Computational approaches for membrane structure analysis in cryo-electron microscopy

Inaugural dissertation

for the attainment of the title of doctor
in the Faculty of Mathematics and Natural Sciences
at the Heinrich Heine University Düsseldorf

presented by

Philipp Schönnenbeck
from Essen, Germany

Düsseldorf, May 2025

from the institute for Biology
at the Heinrich Heine University Düsseldorf
and the Ernst Ruska-Centre for Microscopy and Spectroscopy with Electrons:
Structural Biology (ER-C-3)
at the Forschungszentrum Jülich

Published with permission of the
Faculty of Mathematics and Natural Sciences at
Heinrich Heine University Düsseldorf

Supervisor: Prof. Dr. Carsten Sachse

Co-supervisor: Prof. Dr. Holger Gohlke

Date of the oral examination: 01.12.2025

Eidesstattliche Erklärung

Ich versichere an Eides Statt, dass die Dissertation von mir selbständig und ohne unzulässige fremde Hilfe unter Beachtung der „Grundsätze zur Sicherung guter wissenschaftlicher Praxis an der Heinrich-Heine-Universität Düsseldorf“ erstellt worden ist.

_____

Ort, Datum

_____

Philipp Schönnenbeck

Acknowledgements

First, I would like to express my gratitude to Professor Carsten Sachse for his constant support during my PhD and the exceptional scientific as well as methodological supervision. He helped me significantly by allowing me to freely develop new methods but also guiding me whenever I needed help. I am truly grateful for him creating such a good working environment even in difficult times during the pandemic.

I would also like to thank Prof. Holger Gohlke for serving as my co-supervisor. His deep knowledge of the biological but also bioinformatical part of this work was always very helpful during discussions.

Thank you to Dr. Benedikt Junglas for providing me the initial idea for a lot of my methods and also for most of the data I was constantly working with. He was always quick to answer any questions reliably and with a strong scientific background.

Thank you as well to Dr. Sabrina Berkamp for always discussing data and methods with me as well as provide me with new opportunities to test my implementations. I would also like to thank her for proof reading various abstracts, publications as well as this thesis to improve them significantly.

Thank you to Dr. Daniel Mann for providing me with excellent computational support as well as especially in the beginning guiding me often when I had questions about anything. I also want to thank Daniel as well as David Kartte for multiple occasions when we discussed the programmatic part of implementations which helped me develop my methods.

Thank you for everyone else in our institute, especially Esther Hudina, Kevin Boga, Dr. Lisa Jungbluth, Dr. Claire Ortmann, Katerina Filopoulou and Dr. Saba Shahzad

who have contributed to this work in one way or another, including providing data, emotional support, discussions, training, ideas or proof-reading. But I also want to thanks all members of the Sachse lab for their support and friendship during my PhD. I am truly glad to have worked in such a positive and friendly environment. And finally I want to thank my family and especially my girlfriend for the support and encouragement during my journey in my PhD work. Their support brought me to where I am today and helped me when I was struggling, also balancing my life outside of my PhD work.

Summary

Cryo-electron microscopy (cryoEM) is a powerful tool to study protein-membrane interactions as it provides high-resolution images of vitrified macromolecules, including biological membranes, under near-native conditions. While this technique generates rich data, the manual analysis of the resulting images is tedious and time-consuming. This PhD work focused on automating and improving the analysis of cryo-EM micrographs of membrane structures. To analyze 2D images, I developed a neural network for membrane detection and implemented various methods to efficiently process hundreds of images, extracting membrane and vesicle-specific properties using the segmentation as a basis. These methods were released into a comprehensive toolkit called Cryo Vesicle Image Analyser (CryoVIA). The toolkit was successfully applied to diverse datasets, including previously published data on the membrane remodeling properties of phage shock protein A. This analysis confirmed earlier hypotheses about membrane thickness changes in the presence of the protein. Additionally, CryoVIA enabled numerous applications such as size distribution analysis of lipid nanoparticles carrying siRNA imaged by electron microscopy.

Given that cryo-EM can also generate 3D volumes, I demonstrated CryoVIA's versatility by applying it to tomogram slices. I further enhanced the analysis capabilities by implementing an improved method for estimating membrane thickness in tomograms that does not rely on single slices, building upon an existing analysis pipeline.

As a last step, to facilitate the study of membrane remodeling processes captured in

cryo-EM micrographs I implemented a method to find sequential steps of the process in cryoEM micrographs by using variational autoencoders and dynamic time warping.

The analytical tools developed during this thesis work have already proven valuable to the research community, supporting studies of membrane-protein interactions and lipid nanoparticles. As this PhD work concludes, ongoing research still continues to build upon these methods and I hope it will help researchers in the field of structural biology.

Zusammenfassung

Die Kryo-Elektronenmikroskopie (CryoEM) ist eine leistungsfähige Methode zur Untersuchung von Protein-Membran-Interaktionen, da sie hochauflösende Bilder von vitrifizierten Makromolekülen, einschließlich biologischer Membranen, unter naturnahen Bedingungen liefert. Während diese Technik wertvolle Daten generiert, ist die manuelle Analyse der resultierenden Bilder mühsam und zeitaufwendig. Diese Doktorarbeit konzentrierte sich auf die Automatisierung und Verbesserung der Analyse von CryoEM-Bildern von Membranstrukturen. Zur Analyse von 2D-Bildern entwickelte ich ein neuronales Netzwerk zur Membranerkennung und implementierte verschiedene Methoden zur effizienten Verarbeitung hunderter Bilder, wobei membran- und vesikelspezifische Eigenschaften basierend auf der Segmentierung extrahiert wurden. Diese Methoden wurden in einem umfassenden Toolkit namens Cryo Vesicle Image Analyser (CryoVIA) veröffentlicht. Das Toolkit wurde erfolgreich auf verschiedene Datensätze angewendet, einschließlich bereits veröffentlichter Daten zu den membranmodulierenden Eigenschaften des phage shock protein A. Diese Analyse bestätigte frühere Hypothesen über Veränderungen der Membrandicke in Gegenwart des Proteins. Darüber hinaus ermöglichte CryoVIA die Analyse der Größenverteilung von Lipid-Nanopartikeln, die siRNA tragen und deren Bilder im Elektronenmikroskop aufgenommen wurden.

Da CryoEM auch 3D-Volumen generieren kann, demonstrierte ich die Vielseitigkeit von CryoVIA durch die Anwendung auf Tomogrammschnitten. Ich erweiterte die Analysemöglichkeiten durch die Implementierung einer Methode zur Schätzung der Membrandicke in Tomogrammen, die nicht auf einzelnen Bildern basiert und auf einer bestehenden Analyse-Pipeline aufbaut.

Als letzten Schritt implementierte ich zur Unterstützung der Untersuchung von membranmodulierenden Prozessen, die in CryoEM-Bildern erfasst wurden, eine Methode zur Identifizierung sequentieller Prozessschritte in CryoEM-Bildern unter Verwendung von variational Autoencodern und Dynamic Time Warping.
Die während dieser Doktorarbeit entwickelten Analysemethoden haben sich bereits als wertvoll für die Forschung erwiesen und unterstützen Studien zu Membran-Protein-Interaktionen und Lipid-Nanopartikeln. Während diese Doktorarbeit zum Abschluss kommt, gibt es laufende Anwedungen, die auf diesen Methoden aufbauen und ich es hoffe sie werden Wissenschaftlern in der Strukturbiologe weiterhelfen.

Contents

List of Figures

List of Tables

List of Abbreviations

ATP	**A**denosine **t**ri**p**hosphate
CCD	**C**harge **c**oupled **d**evice
CLEM	**C**orrelative **l**ight and **e**lectron **m**icroscopy
CMOS	**C**omplementary **m**etal **o**xide **s**emiconductors
CNN	**C**onvolutional **n**eural **n**etwork
(cryo)EM	(Cryogenic) **e**lectron **m**icroscopy
(cryo)ET	(Cryogenic) **e**lectron **t**omography
cryoVIA	**Cryo** **V**esicle **I**mage **A**nalyser
DED	**D**irect **e**lectron **d**etector
DOPC	1,2-**d**i**o**leoyl-sn-glycero-3-**p**hospho**c**holine
DOPG	1,2-**d**i**o**leoyl-sn-glycero-3-**p**hospho-(1'-rac-**g**lycerol)
DPPG	1,2-**d**i**p**almitoyl-sn-glycero-3-**p**hospho-(1'-rac-**g**lycerol)
DTW	**D**ynamic **t**ime **w**arping
EPL	*Eschericha coli* **p**olar **l**ipid extract
ER	**E**ndoplasmic **r**eticulum
ESCRT	**E**ndosomal **s**orting **c**omplexes **r**equired for **t**ransport
FEG	**F**ield **e**mission **g**un
FIB	**F**ocused **i**on **b**eam
GUI	**G**raphical **u**ser **i**nterface
GUV	**G**iant **u**nilamellar **v**esicle
LNP	**L**ipid **n**ano**p**articles
LUV	**L**arge **u**nilamellar **v**esicle
MLV	**M**ulti**l**amellar **v**esicle

mRNA	**M**essenger **r**ibo**n**ucleic **a**cid
Psp	**P**hage **s**hock **p**rotein
ReLU	**Re**ctified **l**inear **u**nit
RGC	**R**egion **g**rowing **c**onvolutional neural network
SEM	**S**canning **e**lectron **m**icroscope
siRNA	**S**mall **i**nterfering **r**ibo**n**ucleic **a**cid
SPA	**S**ingle **p**article **a**nalysis
STA	**S**ub**t**omogram **a**veraging
SUV	**S**mall **u**nilamellar **v**esicle
TEM	**T**ransmission **e**lectron **m**icroscope
ULV	**U**ni**l**amellar **v**esicle
VAE	**V**ariational **a**uto**e**ncoder

Chapter 1

Introduction

1.1 Electron microscopy of biological samples

Electron microscopy is a technique to visualize samples up to the atomic scale. While a conventional light microscope relies on the visible light spectrum to visualize samples, electron microscopes rely on electrons interacting with the sample and can therefore deliver much higher resolution due to the shorter wavelength of electrons.

The field of transmission electron microscopy began with a groundbreaking development in the early 1930s when Ernst Ruska and Max Knoll created the first transmission electron microscope (TEM) (Knoll and Ruska, 1932). While in the first few years only inorganic materials were imaged, in 1939 the first biological samples were imaged using an electron microscope demonstrating the usefulness of the electron microscope for biology by capturing the first image of a virus, the tobacco mosaic virus, in a dry gel (Ruska, Borries, and Ruska, 1939, Kausche, Pfankuch, and Ruska, 1939). The advancements in the field of structural biology using the transmission electron microscope started in the 1980s when biological specimen were embedded in vitreous ice. This removed the need for fixation agents revealing high resolution features that were previously lost by the sample embedding. The samples are kept at their near-native state resulting in artifact-free images (Adrian et al., 1984).

1.1.1 Structure of an transmission electron microscope

The structure of a typical TEM can be seen in 1.1. From top to bottom it incorporates an electron source, also called an electron gun, a system of various condenser lenses and apertures, the sample stage with the specimen, a system of various objective lenses and apertures, a projection lens and a final detector (Moody, 2011). The electron beam emerges from the electron gun and travels through vacuum passing these parts, finally hitting the detector at the end resulting in an image. The various parts of the typical TEM will be discussed and explained in the following paragraphs.

Electron gun: The electron gun is the source of the electrons traveling through the microscope. Historically it was made out of a tungsten filament or a lanthanum hexaboride but the currently most used electron gun is a field emission gun (FEG) (Orloff, 2009). By using an electric field for the FEG instead of heating of the tungsten filament the electrons are extracted at a set energy level of 80 to 300 keV. The extracted electrons need to be very fast in order to get a high resolution image because the resolution of the final image depends on the wavelength of the electrons used which is inversely proportional to its momentum (Moody, 2011).

Lenses: The beam of the microscopes needs to be focused and magnified like in a light microscope to reach various magnifications. The TEM also uses lenses for this purpose but instead of the glass lenses of a light microscope it uses strong coils to create an magnetic field (Moody, 2011). This magnetic field can change the electron beam to the correct direction and into the desired shape. By adjusting the current passing through the coils it is possible to change the magnifications of the microscope very easily (Orloff, 2009). A total of three different lens systems can be found in a typical TEM. The first system is the condenser lens system and which creates a parallel beam from the electrons coming from the electron gun. Creating a precise parallel beam by this lens system is critical to receive high-resolution images (Rose, 2008). The second system is the objective lens system through which

the electrons pass after interacting with the sample. It magnifies the image and focuses the beam to create the real space image of the sample. The magnification of the image can be changed by adjusting the strength of the objective lenses and therefore alter the distance between the sample image plane (Carter and Williams, 2016). This lens system determines the microscope's resolution because all subsequent lenses will magnify its aberrations (Moody, 2011). The last lens system is the projection lens system that projects the beam onto the detection system, often a direct electron detector.

Apertures: Apertures are usually part of the lens systems. They are made out of heavy metals with circular holes, which can be used to reduce or mask the electron beam (Moody, 2011). Electrons that are on the wrong axis or have the wrong energy can be stopped from going further through the microscope (Rose, 2008). Depending on the hole size an aperture can also narrow the electron beam size to adjust to specific resolution goals (Reimer and Kohl, 2008).

Sample stage: The stage is used to hold the sample in place and sits under the condenser lens system. In cryo electron microscopy, the microscope stage needs to be cooled to -180°C using liquid nitrogen to keep the sample frozen in the vitreous ice. To be able to see different locations of the sample, the stage can be moved and to perform tomography stages can also be tilted to acquire images from different viewing angles.

Detector: The detector is the last component of an electron microscope and responsible to visualize the electrons emanating from the column. In modern TEMs, the detectors usually digitize the incoming electrons to create digital images while relying on fluorescent viewing screens or photographic film is not needed any more. Electron detectors such as charge coupled devices (CCD) and complementary metal oxide semiconductors (CMOS) (Tietz, 2008) are often coupled with a scintillator to convert electrons to photons to reduce damage to the detectors. Modern electron microscopes use direct electron detectors (DED) that do not need to convert electrons to photons, have higher electron sensitivity and can be read out faster, which

enables the collections of frames into movies. The development of DEDs combined with improved computation methods led to the so called *resolution revolution* resulting in solving of biomolecular structures to near atomic resolutions in a routine manner (Kühlbrandt, 2014).

The complete column of an electron microscope is under high vacuum to reduce any interactions of the electron beam with any present particles that could redirect the electrons reducing the resolution (Carter and Williams, 2016). When an electron passes through a sample, it interacts with the molecules within destroying the sample as the image is acquired. The radiation damage starts with ionizing the sample, breaking bonds and producing secondary electrons as well as free radicals. The secondary electrons and free radicals can cause further chemical reactions while they migrate through the sample. Finally, hydrogen gas can escape the sample and cause visible morphological changes in the sample (Baker and Rubinstein, 2010). The radiation damage is the dose limiting factor in cryoEM. While increasing the electron dose technically increases the signal and therefore resolution, the radiation damage counteracts this increased resolution by a builtup of radiation damage (Baker and Rubinstein, 2010).

1.1.2 Biological sample preparation

Biological samples are usually prepared by pipetting the sample on a metal grid, freezing it to preserve it in a vitreous ice layer, which is supported by the grid and a supportive film. The grid is then inserted onto the sample stage in the electron microscope and imaged. A typical grid is made out of copper, nickel or gold and is formed as a 3 nm-wide flat disk with a mesh of holes. Copper is most often used but when cells cultured to adhere on the grid, gold is often chosen because of its lower toxicity (Jensen, 2010). Usually, a thin carbon film is applied to the grids resulting in either continuous, holey or lacey grids. Continuous films cover the whole grid and provide the most flat disk but also introduce more background noise. Holey

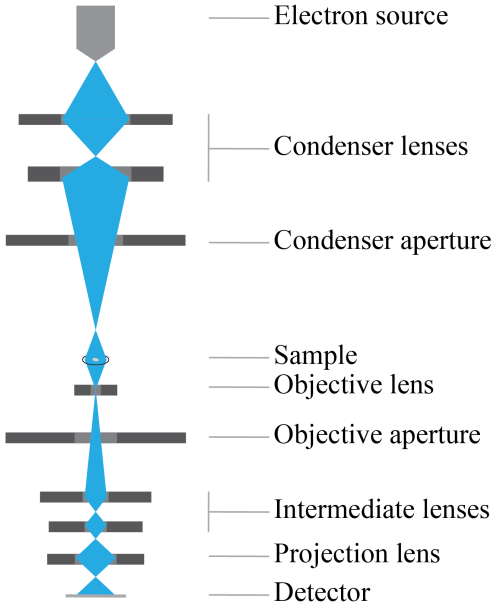

FIGURE 1.1: Simplified structure of an transmission electron microscope. (The figure was conceptually inspired by the PhD thesis of Ortmann De Percin Northumberland.)

films cover the whole grid except for the holes in the mesh (Figure1.2). This way the samples can be visualized in the vitreous ice directly. Lacey films have irregular holes in the carbon and can be used for the thinnest possible support film while still providing stability (Jensen, 2010). There are many variants of grids with different materials, support coatings and various hole sizes. Typical hole sizes in grids are 1.2 and 2 µm with some small fluctuations.

Because the complete microscope column must be kept at a high vacuum, the biological samples have to be preserved and stabilized. The first method to accomplish preservation was dehydration combined with negative staining, chemical fixation and plastic embedding (Jensen, 2010). The dehydration changes the native state of the samples and freezing of the sample was the next method of choice. In order to use biological samples in an electron microscope with minimal artifacts and in a near-native state they have to be frozen in vitreous ice. This reduction in temperature reduces the amount of radiation damage from the electron beam significantly, keeps the sample at a near-native hydrated state as well as protects the sample from the high vacuum in the microscope column (Moody, 2011, Jensen, 2010).

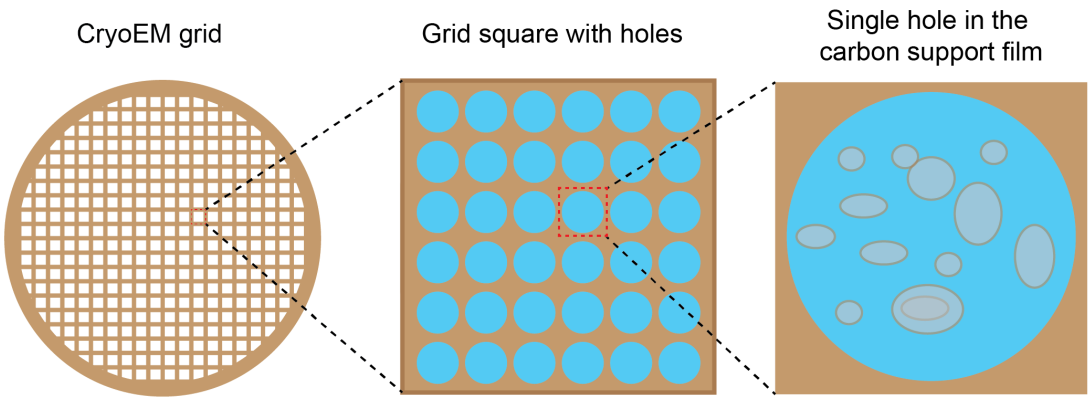

FIGURE 1.2: Illustration of a cryoEM grid. From left to right: A typical cryoEM grid made of a metal mesh forming grid squares. Each square contains a carbon support film with holes. Vitreous ice containing the biological sample is suspended in the holes.

Freezing the sample to obtain vitreous ice can be done by rapidly plunging the sample in liquid ethane, i.e. plunge freezing, or by applying high pressure during the freezing process. After vitrification the samples have to be kept at liquid nitrogen temperatures to prevent the formation of ice crystals (Moody, 2011).

1.1.3 Single particle analysis

CryoEM enables the acquisition of high resolution images of biological samples. Instead of analysing only the individual micrographs, cryoEM is often used to determine three dimensional structures of proteins. When embedding proteins in vitreous ice, the main goal is to have a collection of random orientations of the protein to collect images from all sides of the protein resulting in thousands and sometimes even millions of images from all possible angles. Because all of the 2D projections of the protein are equivalent to slices of the 3D Fourier transform, it is possible to use these projections to reconstruct the object three dimensional shape (Nogales and Scheres, 2015, Sigworth, 2016) combining the application of the Fourier slice theorem as well as the Fourier synthesis (Crowther, DeRosier, and Klug, 1970). This method is called single particle analysis (SPA) because thousands of images

are used to create the three dimensional shape of a single protein (Jensen, 2010).

1.1.4 Cryo-electron tomography

Instead of relying on the random orientations of proteins on the cryoEM grid, it is also possible to reconstruct the three dimensional shape of one specific location in the sample (Koning, Koster, and Sharp, 2018). To obtain various different angles of this region of interest the stage can be tilted. Due to the visibility of the sample holder and the increasing thickness of the sample at higher tilts, the maximum angles are usually at $\sim\pm 70°$ (Wan and Briggs, 2016). Due to the large number of tilted images, they can only be recorded at very low electron doses because the total dose of the region should not exceed 100-180 electrons per $Å^2$, depending on the sample and the used current (Koning, Koster, and Sharp, 2018).

Once a sufficient number of images of varying tilt angles have been collected the tomogram can be reconstructed using the recorded information of the tilt angles and similar methods as in the SPA reconstruction. The method of acquiring the tilt series and reconstructing the three dimensional region of interest is called cryo-electron tomography (CET). Using these reconstructed tomograms to solve the structure of a protein by averaging excised individual proteins it is also known as subtomogram averaging (STA) (Wan and Briggs, 2016).

1.2 Lipid bilayer

1.2.1 Lipids

Lipids are a central class of crucial biological molecules and encompass a large group of organic molecules containing many subgroups. Fats (also fatty acids), phospholipids, mono- and diglycerides, sterols and waxes are the most notable and important subgroups. Lipids are either hydrophobic or ampiphilic (possessing both hydrophobic and hydrophilic properties) and function in organisms as energy

storage (as fat), signalling molecules and cell compartmentalization (as part of membranes) (Gennis, 1989). By being ampiphilic some lipids can form membranes resulting in vesicles or are compartments within a solution or cell. Whenever lipids are mentioned in this dissertation, it is interchangeable with membrane-forming lipids and the following paragraphs will focus on these kinds of lipids.

There are multiple different types of lipids found in biological membranes and each type is in itself a diverse group (Osawa, Fujikawa, and Shimamoto, 2024). The most commonly found lipids are the glycerophospholipids (Gennis, 1989). One of the three hydroxyl groups of a glycerol is linked to a phosphate containing group (hydrophilic) and the other two hydroxyls are linked to hydrophobic components (Figure 1.3A). The hydrophilic phosphate group is often linked to another group, including choline, ethanolamine, serine, glycerol or myo-inositol (Figure 1.3B). Linked to the other two hydroxyl groups are usually long-chain hydrocarbons - fatty acids. These can vary greatly in length, saturation and branching giving this group a wide variety (Gennis, 1989). Glycerophospholipids often make up the majority of membranes found in pro and eukaryotes as the composition of the different phosphate groups can vary a lot (Gennis, 1989). The length of the fatty acids is usually between 16-20 carbon atoms while some cells and microorganisms have smaller or larger fatty acids present in their membrane lipids.

Another group of lipids found in the biological membranes are phosphosphingolipids. They share the same polar component as the glycerophospholipids but the hydrophobic component is replaced by a ceramide - a sphingosine linked to a fatty acid by an amide bond. The most abundant phosphosphingolipid is sphingomyelin (Figure 1.3A) which is abundantly found in animal cell plasma membranes. While phosphosphingolipids can be found in plants and bacteria, these occurrences are rare and they are predominantly found in animal cells (Gennis, 1989).

A third group of lipids are the glycoglycerolipids. These are again similar to glycerophospholipids but instead of replacing the hydrophobic region, the polar headgroup with phosphate is replaced by a link to a carbohydrate. They can be found

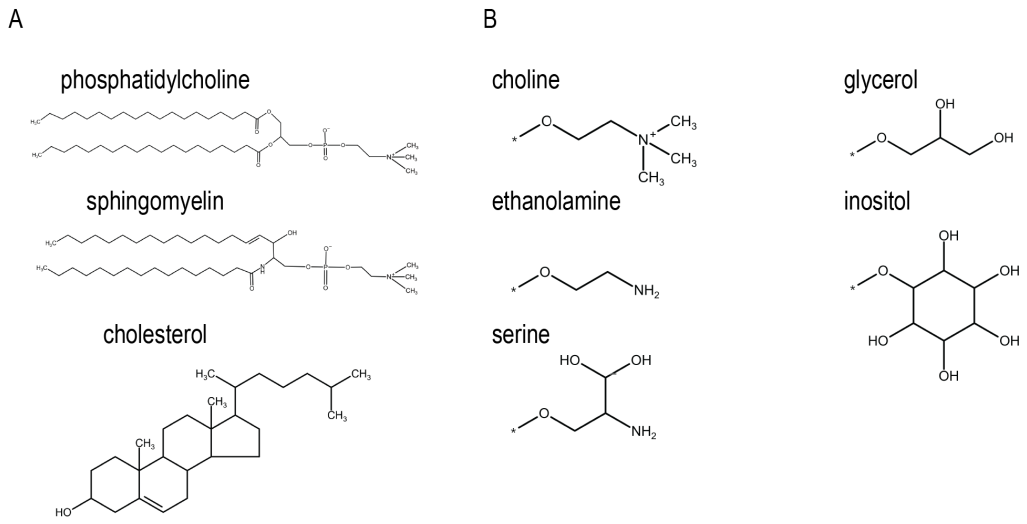

FIGURE 1.3: Lipid structures of typical found lipids (inspired from Gennis, 1989, created using Chemaxon, 2025). (A) Structure of phosphatidylcholine, sphingomyelin and cholesterol. (B) Structure of polar groups commonly found in lipids. Connection to the rest of the lipid is indicated with an asterisk (*). Structures shown are choline, ethanolamine, serine, glycerol and inositol.

predominantly in the membrane of chloroplasts, meaning they are present in plants, algae and some bacteria (Gennis, 1989).

Sphingolipids can also be linked to a carbohydrate instead of a polar phosphate group. These are called glycosphingolipids and they are quite rare but can be found in the outer cell plasma membrane of animals. They are especially important in the erythrocyte membranes because they carry blood group antigens (Gennis, 1989).

The last big group of lipids mentioned here are sterols with cholesterol being the most commonly found, by far. A small polar hydroxyl group is linked to a larger rigid structure mostly made out of four carbon rings giving this lipid a very different structure than the other lipids mentioned earlier (Figure 1.3A). Cholesterol is found almost exclusively in animals cells in various membranes and often makes up ~30% of the cell plasma membrane in animal cells (Gennis, 1989).

There are various additional lipid types that can be found in small numbers in membranes with various functions but they will not be further discussed in the chapter.

1.2.2 Membranes

Membranes can be found in every living cell and play a central roll in maintaining the structure and adding function to it. The basic function of a biological membrane is to define an inside and outside, thus compartmentalizing the cell (Gennis, 1989, Cooper, 2000). Most biological membranes are composed of two layers of lipids of various compositions, the lipid bilayer. The hydrophobic part of those two layers define the inside of the membrane and the hydrophilic segment is interacting with surrounding components. Embedded in these bilayers are membrane proteins that have a wide variety of functions. These proteins can stretch throughout the membrane forming a passage for ions and small molecules allowing controlled regulation of the chemical composition of the inside. Other proteins stretching throughout the membrane can be interacted with on one side of the membrane and lead to reactions on the other side, regulating enzymatic reactions from another compartment. Multiple embedded proteins in close proximity to each other can increase the effectiveness of chain reactions. Proteins and especially enzymes embedded in the membrane play a vital role in the function of the cell and its compartments and enable the communication between multiple membrane enclosed entities (Gennis, 1989, Cooper, 2000).

In eukaryotes most of the lipids present in membranes are synthesized inside the endoplasmic reticulum except for some specific lipid types and carbohydrate bound to lipids which are synthesized inside the golgi apparatus (Cooper, 2000).

The combination of lipid compositions on either side of the lipid bilayer can influence its interaction with the environment but also the membrane's local curvature. By having a higher concentration of large headgroups on one side of the membrane the membrane can be heavily curved (Gennis, 1989, Harayama and Riezman, 2018) (Figure 1.4A). This can create a variety of different shapes which membrane enclosed compartments can have (Döbereiner, 2000). Variety in fatty acids and protein composition of the membrane can also influence the curvature

(Figure 1.4A) and create necessary shapes increasing the effective area to interact with (Harayama and Riezman, 2018). The composition of lipids and especially the distribution of fatty acid lengths have an effect on the lipid bilayer thickness (Figure 1.4B). While longer fatty acid chains and cholesterol lead to greater bilayer thickness (Mitra et al., 2004), shorter fatty acid chains and higher levels of unsaturated lipids lead to lower bilayer thickness (Mitra et al., 2004, Binder and Gawrisch, 2001) and embedded proteins can also change the bilayer thickness by up to 5 Å. The bilayer thickness, levels of unsaturation and the lipid composition all have a strong effect on the permeability of the membrane (Mitra et al., 2004) and are therefore important factors to study when researching membranes.

Membrane-bound proteins can also be found in lipid rafts which are small platforms made out of sphingolipids, cholesterol and protein assemblies that can float freely within the bilayer of cellular membranes (Simons and Ehehalt, 2002). These rafts are more ordered and densely packed than the surrounding bilayer structure and play an important role in the pathogenesis of various diseases (Simons and Ehehalt, 2002).

1.2.3 Types of membrane compartments

Inside eukaryotic cells multiple different organelles exist, which are surrounded by a membrane with very specific lipid compositions. Organelles are either surrounded by a single lipid bilayer or have an additional bilayer creating an inside, an outside and a space inbetween bilayers for complex interactions and reactions. The lipids making up the lipid composition of organelles mentioned in the following paragraphs only include lipids that make up more than 5% of all lipids. In each case there are a lot more lipid types present in the membranes which are not included. Additionally, any type mentioned in the following paragraphs can be further divided into subtypes with various fatty acid lengths, saturations and branching.

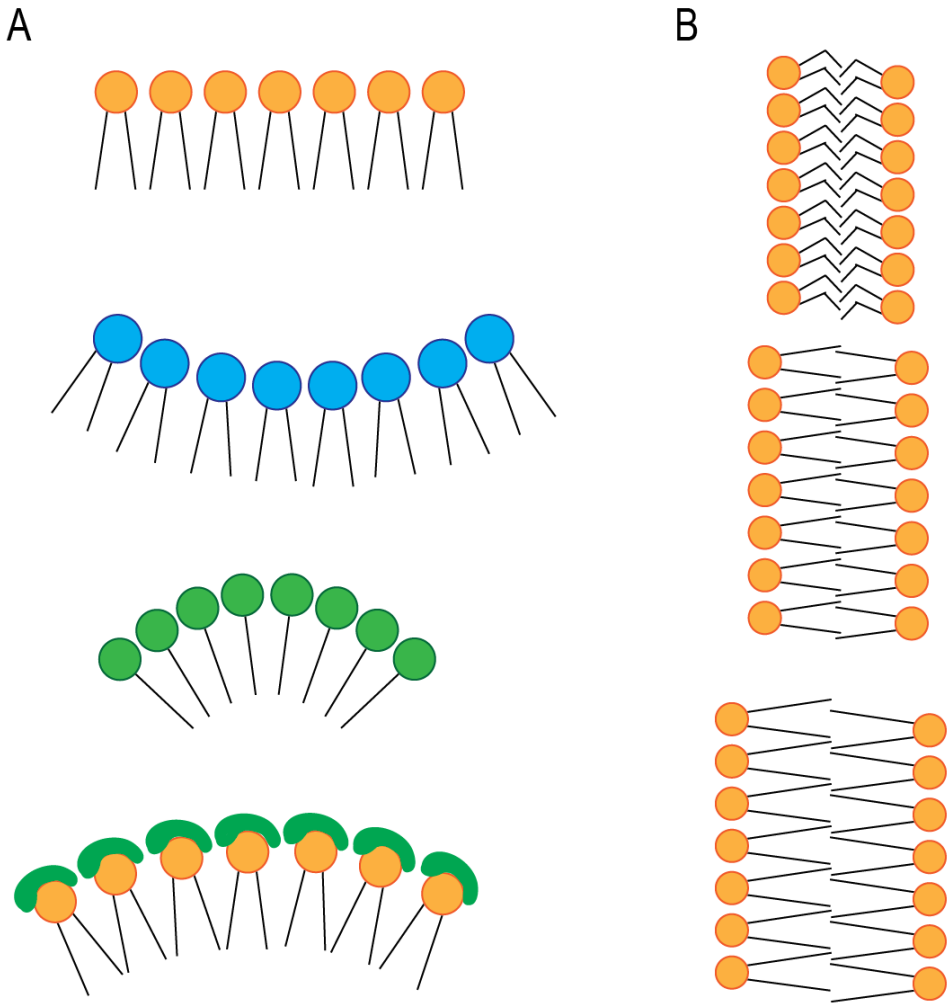

FIGURE 1.4: The effect of lipid composition on the structure of lipid bilayers. (A) The illustration shows the effect of the lipid types on the curvature of membranes. From the top to bottom: Flat membrane - A flat membrane usually consists mostly of phosphatidylcholine and phosphatidylserine. Negative curvature - Negative curvature can occur when conical lipids with small headgroups like phosphatidylethanolamine are present. Positive curvature - Positive curvature can occur with large headgroups like inositol or when only a single unpolar tail is present. Positive curvature can also be induced by the presence of proteins on top of the polar headgroup. (B) The illustration shows examples of how changes in the fatty acids composition can affect the bilayer thickness. Saturation levels, longer chains and branching (not shown) can all lead to differences in the bilayer thickness.

Single lipid bilayer

Plasma membrane: The plasma membrane defines the cell and its boundaries and surrounds the entire cell. As it is the contact point with the outside it serves as the interaction element between the cell, other cells and its environment. Therefore, it has many specialized areas to regulate the cell's inner homeostasis, to communicate with other cells and transport ions and molecules across the membrane. Plasma membranes can form substructures such as microvilli together with an inner actin filament skeleton greatly increasing the effective area of interaction with the environment. The lipid composition of plasma membranes in eukaryotes is mostly made up of five lipids (for mammalian plasma membrane): cholesterol, phosphatidylcholine, sphingomyelin, phosphatidylethanolamine, phosphatidylserine (in decreasing amount) (Casares, Escribá, and Rosselló, 2019). The exact amount of the different lipid types varies in different sources but is also influenced by cell type or maturation stage of cells. In prokaryotic cells, the lipid composition is simpler and is mostly made up of two lipids (for *Escherichia coli's* (*E. coli*) inner membrane): phosphatidylethanolamine and phosphatidylglycerol (Rowlett et al., 2017).

Lysosome: Lysosomes are organelles of varying shapes responsible for the degradation of macromolecules. The enzyme composition inside lysosomes is made out of a mixture of ~50 different acid hydrolases that can degrade proteins, lipids and other organic molecules. Materials to digest in the lysosomes is often acquired through endocytosis, transported to the lysosomes and fused into the lysosomes. Another pathway of digestion is through phagocytosis by taking up large foreign particles and autophagy that recycles cellular components by a series of steps involving the engulfing of other organelles to digest. By having a flexible membrane the shape of a lysosome reflects the material currently being digested (Gennis, 1989). The lipid composition of

the lysosome membrane is made up of mostly six different lipids: cholesterol, phosphatidylcholine, sphingomyelin, phosphatidylethanolamine, bismonoacylglycero-phosphate and phosphatidylinositol (in decreasing amount) (Casares, Escribá, and Rosselló, 2019).

Endoplasmic reticulum: The endoplasmic reticulum (ER) is made out of multiple tubes and flattened sacs of membranes, also called cisternae. The membrane is connected with the outer nuclear membrane creating a continuous inner lumen between them. Membrane-bound proteins and membranes destined for other membrane-bounded organelles are synthesized in the rough ER, which is covered by ribosomes. The smooth ER is the synthesis site of sterols and involved in fatty acid desaturation. Four lipids make up most of the lipid composition of the ER: phosphatidylcholine, phosphatidylethanolamine, phosphatidylinositol and cholesterol (in decreasing amount).

Golgi apparatus: The Golgi apparatus often appears as a series of stacked flat membrane disks of varying sizes but the cisternae can also be scattered throughout the cytoplasm (Suda and Nakano, 2012). It serves mainly to modify glycoproteins coming from the ER after their translation before they are secreted or embedded into the plasma membrane. The proteins to modify go through through these disks in a defined direction and get modified further and further. Each disk has a different enzymes composition and is responsible for different reactions and modifications. The Golgi apparatus is also responsible for the synthesis of glycolipids as well as sphingomyelin (Cooper, 2000). The membrane of the Golgi apparatus is mostly made out of six types of lipids: phosphatidylcholine, phosphatidylethanolamine, cholesterol, phosphatidylinositol, phosphatidylserine and sphingomyelin (in decreasing amount) (Casares, Escribá, and Rosselló, 2019).

Double lipid bilayer

Mitochondrion: Mitochondria are the organelles that are responsible for producing the energy used by the cell in form of adenosine triphosphate (ATP). It has an inner as well as an outer membrane with an intermembraneous space between these two membranes, the so called intermembrane space. The inner membrane folds inside the inner part of the mitochondrion, the matrix, to so called cristae and is responsible for the ATP synthesis by a combination of various membrane-embedded proteins enabling the transfer of electrons. This transfer of electrons and the synthesis of ATP is enabled by a proton gradient between the matrix and the intermembraneous space. The lipid composition of the mitochondrial membranes is mostly made up of four lipids: phosphatidylcholine, phosphatidylethanolamine, cholesterol and phosphatidylinositol (in decreasing amount) (Casares, Escribá, and Rosselló, 2019).

Nucleus: The double lipid layer of the nucleus, also called the nuclear envelope, surrounds the perinuclear space. Multiple nuclear pores are spread across the nucleus connecting the cytoplasm with the inner nucleus area. To form these pores the inner and outer membrane of the nucleus fuse together creating circular gaps with a diameter of ~600 Å (Cooper, 2000). Inside these pores is a large protein complex called the nuclear pore complex and it is are large enough to let selective polar proteins through to regulate reactions inside the nucleus as well as allow mRNA to pass through into the cytoplasm. The outer nuclear membrane is connected to the endoplasmic reticulum creating a continuous space between the perinuclear space and the inner lumen of the endoplasmic reticulum. The lipid composition of the nuclear membrane is very similar to the lipid composition of the plasma membrane with the exception that the cholesterol content is a lot lower while the phosphatidylcholine content is a lot higher (Casares, Escribá, and Rosselló,

2019).

Chloroplast: Chloroplasts are a type of organelle only found in plants and algae and are responsible for the photosynthesis by using the energy from the sunlight to produce sugar and other organic molecules. They have an outer and an inner membrane as well as stacks of membrane disks, the thylakoid membranes, inside the inner part of the chloroplast, the stroma. Inside the thylakoid membrane are multiple proteins embedded that make up the photosynthesis system. The photosynthesis system uses the energy of the sunlight to transfer electrons through multiple proteins and using the energy to create sugar to store the energy. The lipid composition of the chloroplast membranes is very different to other eukaryotic organelle membranes. It consists mostly of monogalactosyldiacylglycerol, digalactosyldiacylglycerol, phosphatidylglycerol, sulfoquinovosyl diacylglycerol, phosphatidylcholine and phosphatidylinositol (in decreasing amounts, respectively) (Botella et al., 2016).

1.2.4 Liposomes

The name liposomes describes any object in which a lipid bilayer encapsulates a volume (Gennis, 1989), which would also include most other membrane structures presented here. Usually, when liposomes are mentioned, artificial vesicles in an artificial environment are meant. From here on forward, liposomes are defined as the artificial vesicles.

Liposomes are formed when introducing phospholipids to water because of their ampiphilic characteristics. The generated vesicles are usually heterogeneous in size and often form multilamellar vesicles (MLVs) - vesicles within vesicles - observed as multiple concentric rings in micrographs (Nsairat et al., 2022). Unilamellar vesicles (ULVs) can be created through various methods (Gennis, 1989) and are often desired when using liposomes to study lipids, membrane proteins or reagents. Liposomes are often used to study lipid compositions but they can also be used to

store solutes for drug delivery in medicine as lipid nanoparticles (Nsairat et al., 2022). ULVs are further separated into three categories:

Small unilamellar vesicles (SUVs): These liposomes have diameter of <500Å and are usually prepared by sonication (Chapman, 1987). The induced pressure from the sound energy breaks up larger vesicles into SUVs resulting in a more size-homogeneous sample. Other methods include injection of ethanolic solutions of lipids (Lombardo and Kiselev, 2022) and the usage of a french press (Lombardo and Kiselev, 2022). Because of the high curvature of these small vesicles, they can be used to study asymmetrical lipid distributions between the two leaflets. The cone shapes lipids with bigger headgroups can be found more often on the outer lipid layer and smaller lipids are usually found on the inner layer (Gennis, 1989).

Large unilamellar vesicles (LUVs): These liposomes are usually described as liposomes with a diameter of 500-5000Å depending on the source of definition. They can be created by various methods including but not limited to detergent dialysis (Freytag, 1985), extrusion (Hokanson and Ostap, 2006) and the usage of polycarbonate filters. LUVs are used to study and perform drug delivery but can also be used to study viral (Zhou and Resh, 1996, Dalton et al., 2007, Brémaud, Favard, and Muriaux, 2022) and other disruptive effects on membranes.

Cell-size unilamellar vesicles or giant unilamellar vesicles (GUVs): These liposomes are all unilamellar vesicles bigger than LUVs up to a diameter of 100 µm. They are very simple membrane systems but can be used to study complex biological membrane interactions involving heterogeneities in lipid composition, shape, mechanical properties, and chemical properties (Bhatia et al., 2015). They can also be used to study the effect of pore-forming toxins (Aden, Snoj, and Anderluh, 2021).

Lipid nanoparticles

Lipid nanoparticles (LNPs) are a specific type of liposomes. They are microscopic structures composed of engineered lipid molecules that form protective spherical vessels (Editorial, 2021). These versatile carriers improved modern medicine by providing a solution to one of the big problems in drug delivery research: protecting sensitive therapeutic molecules and ensuring their safe transport through the body's complex environment (Nsairat et al., 2022). Usually lipid nanoparticles are spherical vesicles with ionizable lipids. These lipids are neutral at physiological pH but positively charged in low pH environments (Editorial, 2021). Their unique composition allows them to encapsulate various therapeutic agents, from small molecule drugs to large biomolecules like proteins and nucleic acids.

LNPs have emerged as one of the most promising innovations in drug delivery systems. These advanced delivery vehicles excel in their versatility and reliability, particularly in delivering genetic material like small interfering ribonucleic acid (siRNA) specifically to liver tissue. Their specific structure provides crucial protection for delicate nucleic acids against degradation from both environmental factors and biological processes, while maintaining precise control over the delivery process (Nsairat et al., 2022). The size and composition enables the crossing into cells but also the release of the content into the cells cytoplasm. Additional lipids reduce the chance to be degraded in the body or the cell (Editorial, 2021). Specialized solid lipid nanoparticles can also be used to target the brain for drug delivery by being able to cross the blood brain barrier, which often is a limiting factor for treating diseases linked to the central nervous systems (Satapathy et al., 2021). This combination of targeted delivery and protective capabilities has established LNPs as a cornerstone in modern pharmaceutical development.

Other lipid structures

There are various other interesting membrane structures that are not studied or characterized in this thesis but are worth mentioning.

- Micelles are small round particles made out of lipids. The hydrophilic headgroup forms a spherical shape and is in contact with the surrounding environment and the hydrophobic tail points inward to the center.
- Nanodiscs are small disc-like structures of a lipid bilayer stabilized by a belt using membrane scaffold proteins or synthetic polymers. They mimic small segments of membranes very well and can be used to study membrane embedded proteins.
- Lipidic cubic phase is a liquid crystalline structure that can be used to study the structure of membrane proteins by crystallizing them.

1.3 Phage shock protein A

The phage shock protein A (PspA) is a key component of the phage shock protein (Psp) system that helps bacteria stabilize their inner membranes during various stress conditions (Osadnik et al., 2015, Darwin, 2005). The Psp system responds to extracytoplasmic stress that may reduce the cell's energy status, including phage infections, heat stress, mislocalization of envelope proteins, and exposure to organic solvents (Darwin, 2005, Flores-Kim and Darwin, 2016). The best studied Psp system is in *E. coli*, where it consists of several proteins, including PspA, PspB, PspC, PspD, PspE, PspF, and PspG (Flores-Kim and Darwin, 2016). The core of the system involves four proteins: PspA, PspB, PspC, and PspF, which form a signal transduction cascade between the inner membrane and the cytoplasm (Flores-Kim and Darwin, 2016). PspA plays a central role in the Psp response:

- Regulatory function: PspA interacts with PspF, the transcriptional activator of the system, forming a PspA·F complex (Osadnik et al., 2015). This interaction inhibits PspF's ATPase activity and down-regulates Psp gene expression (Osadnik et al., 2015, Flores-Kim and Darwin, 2016).

- Effector function: As the most abundant Psp protein, PspA is crucial for maintaining cytoplasmic membrane integrity and the proton-motive force (Darwin, 2005, Flores-Kim and Darwin, 2016).

- Membrane interactions: PspA can associate with the inner membrane and bind to negatively charged lipids, helping to reduce membrane stress (Osadnik et al., 2015, Flores-Kim and Darwin, 2016, Jovanovic et al., 2014).

- Protein interactions: PspA interacts with the putative sensor proteins PspB and PspC (Osadnik et al., 2015, Flores-Kim and Darwin, 2016, Joly et al., 2010). During stress conditions, PspA switches its interaction from PspF to PspBC, allowing for Psp gene expression (Osadnik et al., 2015).

- Oligomerization: PspA can form higher-order structures, including helical rods, that are thought to contribute to its membrane-stabilizing properties (Osadnik et al., 2015, Junglas et al., 2021).

The Psp response involves a complex signalling cascade. Under normal conditions, PspA inhibits PspF's activity by forming the PspA·F complex (Osadnik et al., 2015, Flores-Kim and Darwin, 2016). During stress, PspBC likely acts as a sensor, interacting with PspA and releasing it from PspF (Osadnik et al., 2015, Flores-Kim and Darwin, 2016). The freed PspF then activates transcription of Psp genes, including PspA (Flores-Kim and Darwin, 2016, Joly et al., 2010). Increased PspA levels help stabilize the membrane through direct interactions and potential remodelling events (Osadnik et al., 2015, Junglas et al., 2021).

This intricate interplay between Psp proteins allows bacteria to respond effectively to membrane stress, maintaining cellular integrity and energy status during adverse

conditions. In this thesis PspA from the cyanobacterium *Synechocystis* species is studied, also sometimes called SynPspA.

1.4 Computational methods

1.4.1 Convolution and correlation

Convolution and correlation are fundamental techniques in digital image and signal processing for applying filter masks to data (Gonzalez and Woods, 2008). In digital signal processing the data and the applied mask are in the simplest case one-dimensional arrays of values. To perform a correlation between the data f and the mask w one has to move the mask along the data and calculate the sum of products at every step (Smith, 1997). To be able to calculate a sum at the beginning and end of f, various methods of padding can be used, often zero or edge padding. Usually, the resulting signal is cropped the obtain a result with the same size of the original signal.

Convolution follows the same procedure but with the difference that the mask is rotated 180° before application. For symmetrical masks, convolution and correlation result in identical results. However, they serve different purposes in practice: convolution is mostly used for filtering operations like smoothing and edge detection, while correlation is used for template matching and similarity assessment of images. When applied to digital images, these techniques extend to two-dimensional arrays, using the same fundamental approach of sliding the mask pixel by pixel and computing weighted sums.

Convolutions especially are also used in specific types of neural networks called convolutional neural networks, although usually the mask or kernel is not being flipped in these kinds of networks and the operations are actually correlations.

1.4.2 Convolutional neural networks

Neural networks are sophisticated machine learning models inspired by the biological structure of neurons in the human brain (Goodfellow, Courville, and Bengio, 2016). At their core, neural networks consist of two fundamental components: nodes (often called neurons) and edges (or connections) that link these nodes together. Each node operates like a computational unit with the ability to process information. When a node receives input signals through its incoming edges, it applies a non-linear transformation using what is known as an activation function. This function introduces complexity and allows the network to learn and represent intricate patterns that linear models cannot capture. The node then generates an output signal that is transmitted to other nodes through its outgoing edges. Each edge has a weight assigned which regulates the strength of this signal which are dynamically adjusted, enabling the network to learn and improve its performance. Nodes are often structured in layers in which the nodes are usually not connected to each other but to nodes in different layers. The layers between the input and output layer are often referred as hidden layers. If there is a clear direction through the network from one layer to the next without feedback connections these networks are called feedforward (Figure 1.5). Otherwise, if there are feedback loops occurring, connections from one node to a previous node, these networks are called recurrent neural networks. The basic idea of a neural network is to approximate some function f with $f(x) = y$ where x is the input to the network and y the output of the network.

To train a neural network usually labelled data has to be available, which means that pairs of input and expected output should have previously been created, either by manual curation, experimental data or another method of reliable labeling or calculations. In an untrained, state the output of the neural network is random because the starting weights of all edges are in some form randomly assigned. The output of a specific input is then compared to the expected output and a difference

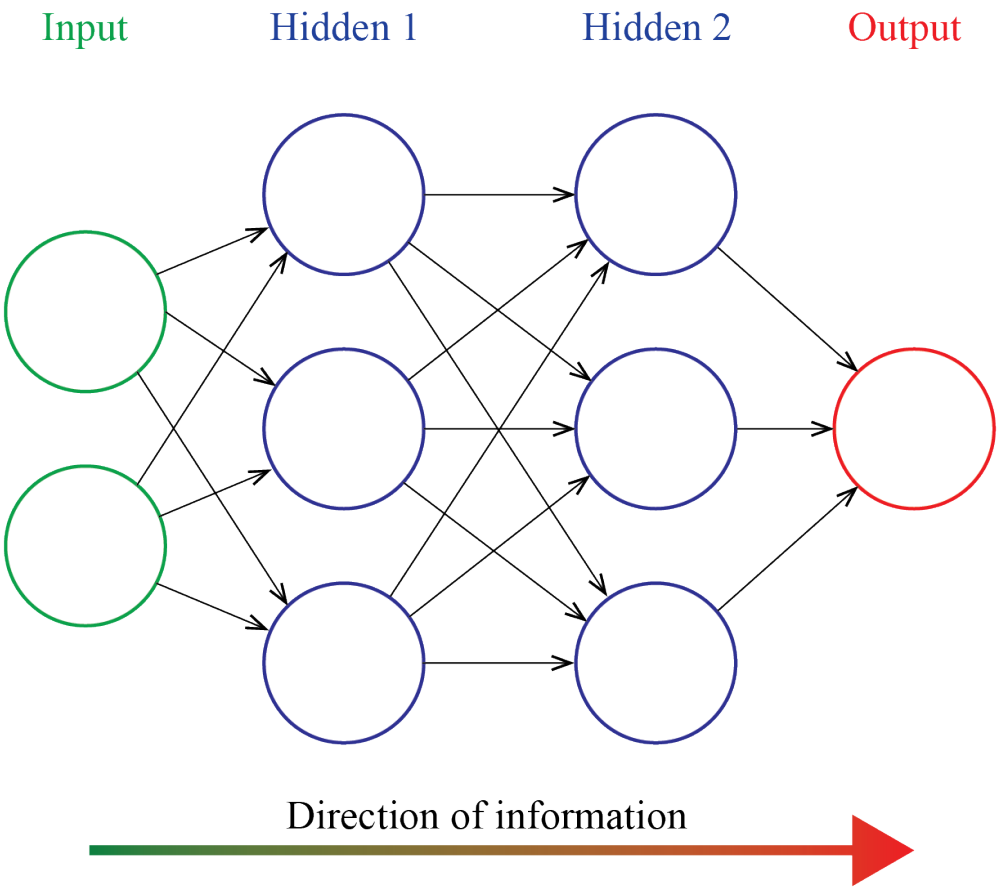

FIGURE 1.5: Illustration of the information flow in a feed forward neural network. The illustration shows the input pass through two fully connected layers and ending in the output layer. Nodes are depicted as circles, each column of nodes is a layer and the entirety of all layers and their connections is the neural network.

is calculated by a specified loss function. Using this loss, gradients can be calculated for each output by backpropagation through the entire network and the weights are adjusted by an optimizing algorithm based on these gradients. This is an iterative process and each input is send through the network multiple times. The loss should decrease over the course of these iterations. When the network was trained long enough and when the training data was representative enough the network should be able to create relatively precise predictions of previously unseen data.

Convolutional neural networks (CNNs) are a specific type of neural network. In convolutional neural networks every node from a convolution layer performs a convolution (technically a correlation) with its own specific filter on the input signal and creates a new output with the same shape as the input (Goodfellow, Courville, and Bengio, 2016). Usually multiple convolutional layers are present in a CNN and with each additional layer the network can learn more complex patterns because the input for each new layer is the output from a previous convolution. The values of each filter are learned during training. Using these convolutional layers it is easier to learn contextual information in sequences or images because each value of an input is the combination of local context from previous calculations. CNNs are often used when the spatial context of a value is of importance and are one of the most important types of neural networks used in computer vision.

1.4.3 Autoencoders

Autoencoder networks are a specific type of feed forward neural networks in that they are trained to copy their input to their output (Goodfellow, Courville, and Bengio, 2016, Ballard, 1987). Their network architecture is often separated into an encoder and a decoder part. The encoder part f uses the input x to create an intermediate output h, $h = f(x)$ often called the latent space, and the decoder part g uses the intermediate output h to create the output r of the autoencoder, $r = g(h), r = g(f(x))$. While the output of an autoencoder is often discarded for

further use, the intermediate output h is rather used for any downstream analysis. Autoencoders are usually constructed and trained in a way that they cannot exactly copy the input to the output by limiting the size of the intermediate result h. This enables the network to reduce the input to a smaller space of values hopefully learning what part of the input is important and which part is redundant. The function $h = f(x)$ can therefore be seen as a lossy compression and $r = g(h)$ tries to recover the data from the compression.

An autoencoder network architecture has to be chosen carefully in order for the network to actually learn a reduced representation of the input. It largely depends on the size, shape and complexity of the input variables. Autoencoders with a very low loss value during training can reconstruct the input almost perfectly but may not be useful in any way if the architecture is not suitable for the given problem. Training the network is usually also performed by using the backpropagation method and using the input as the desired output.

The intermediate output h of an autoencoder can be used for various further methods as semi-supervised classification, content analysis, unsupervised clustering, data reduction and data visualization (Goodfellow, Courville, and Bengio, 2016). The basis for all further analysis is the idea that similar input should create intermediate outputs that are also similar or in some cases close to each other. Autoencoders can also be used as a generative model to generate new data based on the training by generating a latent space sample directly without the use of the encoder and subsequently creating the fitting output using the decoder. Depending on the complexity and the size of the training data this is more or less promising because the latent space is disorganized and irregular so that large parts in the latent space were never encoded using the encoder part and were never learned by the decoder. One way to try to improve this function is the implementations of variational autoencoders. Building upon the explanation of traditional autoencoders, variational autoencoders (VAEs) represent a significant advancement in generative modelling capabilities (Kingma and Welling, 2013). Unlike normal autoencoders, VAEs use a probabilistic

method for the encoding process. The input data is encoded as probability distribution as mean and variance in the latent space instead of directly encoding it into the latent space. This probabilistic encoding creates a continuous, well-organized latent space where similar inputs are mapped to overlapping probability distributions.

The main innovative method of VAEs is their training loss, which combines two components: a reconstruction loss like in traditional autoencoders, and a regularization term known as the Kullback-Leibler divergence. The KL divergence is a method to encourage the encoded latent space distributions to approximate a standard normal distribution, hopefully resulting in a more structured and continuous latent space. This regularization leads to a latent space that is smooth and well-organized, making it possible and viable to sample new points from the latent space and generate more meaningful outputs through the decoder than before. The organized nature of the latent space in VAEs addresses the limitation of traditional autoencoders where large portions of the latent space might correspond to unrealistic outputs because the decoder was only trained on specific latent space inputs. As a result, VAEs can be used for generative tasks, to reconstruct new data similar to the existing training data but also for a more distinct latent space representation because of the need to distinguish probability distributions.

1.4.4 Dynamic time warping

Dynamic Time Warping (DTW) is a powerful algorithmic technique designed to measure similarity between two temporal sequences that may vary in speed or time (Sakoe and Chiba, 1978). At its heart, DTW solves a fundamental challenge in comparing sequences: how to align and measure distance between time series that might be stretched, compressed, or slightly misaligned.

The algorithm is rooted in dynamic programming, a mathematical optimization approach that breaks complex problems into simpler subproblems. DTW has a

computational complexity of $O(N\,M)$, where N and M represent the lengths of the two sequences being compared. This makes it computationally intensive for very long sequences, but highly flexible for comparing sequences with minor temporal variations.

Conceptually, DTW is closely related to the Needleman-Wunsch algorithm, originally developed for biological sequence alignment (Needleman and Wunsch, 1970). The core mechanism involves constructing a matrix representing all possible alignments between two sequences. The algorithm then navigates through this matrix from the origin (0,0) to the final point (N-1, M-1), seeking an optimal path that minimizes the total distance between sequence elements.

At each step the algorithm either matches the next two values in the sequences with each other or only advances one of the two sequences and matches it with the previously matched value of the other sequence - so called warping. This flexibility ensures that every value in each sequence is matched at least once, though some values may be matched multiple times (Figure 1.6A and B). The final distance measurement is calculated by summing the differences between matched values, providing a comprehensive similarity score. To prevent excessive warping a window restraint can be added which limits the distance a value can be warped. An alternative is to add a penalty value to the distance measurement each time the sequence is warped. This is also called amerced dynamic time warping (Herrmann and Webb, 2023).

DTW can also be used to find a small sequence in a larger collected signal by changing the restriction of starting from the origin (0,0) and ending at (N-1, M-1) to starting in the top row (0, X) and ending in the bottom row (N-1, Y) (Figure 1.6C). DTW is used in very different fields including speech recognition (Permanasari, Harahap, and Ali, 2019), gesture recognition (Li et al., 2019), musical analysis (Lijffijt et al., 2010), stock market analysis (Grzejszczak et al., 2022), medicinal signal processing (Jiang et al., 2020) and shape analysis (Zhao and Itti, 2016).

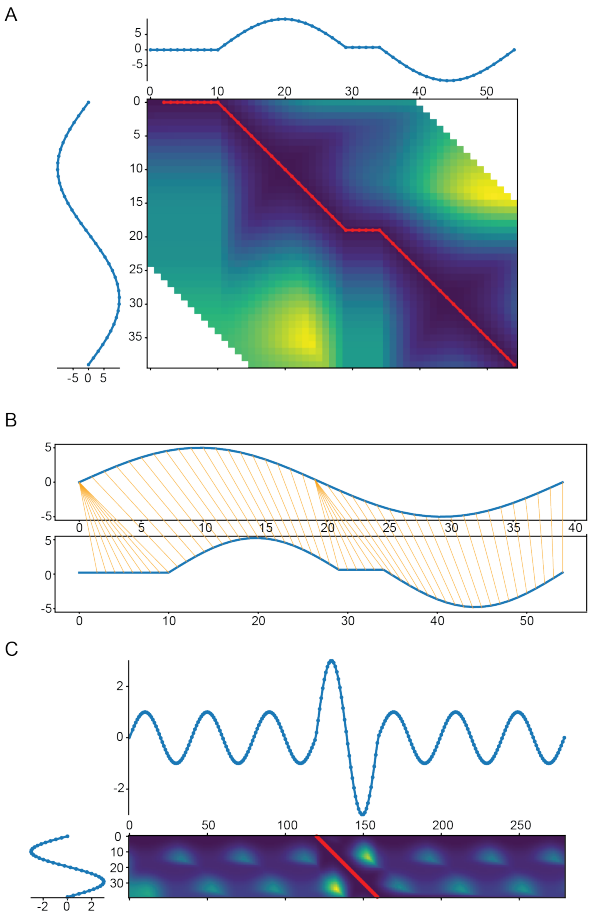

FIGURE 1.6: Examples of the dynamic time warping methods. Figures were created using the dtaidistance python package (Meert et al., 2020) and subsequently modified. A: The top and left graph show two simplified example signals. The graph in the middle shows a heatmap of differences between the mappings between signal 1 and 2. The best mapping is shown in dark blue while the worst mapping is shown in yellow. The red line indicates the best path through the heatmap from the top left to the bottom right indicating a complete mapping between the two signals. A horizontal line indicates a mapping of multiple values of signal 1 to one value of signal 2 and a vertical line would indicate the opposite. A diagonal line indicates a continuation of indices from both signals. B: The resulting mapping from the signals in A. The graph on top shows signal 1 and the lower graph shows signal 2. Each mapping of the different indices of the signals is indicated by an orange line connecting the two values. C: Similar to A the graphs show two signals and the best mapping of the two signals. The restriction of having to start at the top left and having to end in the bottom right is changed to having to start in the top row and ending in the bottom row. This means that every value of signal 2 has to be mapped to a value in signal 1 but not reversely. The red line shows again the best path from the top row to the bottom row. This illustrates the method of searching for subsequences (signal 2) inside a larger sequence (signal 1).

1.4.5 Skeletonization

Skeletonization is a digital image processing method to convert a binary image of an object to a thinned version of this object. An exact definition of a morphological skeleton does not exist and there are various different methods of skeletonization published (Zhang and Suen, 1984, Lee, Kashyap, and Chu, 1994) resulting in very similar by slightly different skeleton versions of a binary object. The skeleton of an object should represent that object as a thin one-pixel wide line while the connectivity should remain the same. Methods to generate a skeleton can be either using a distance transform of the object or iterative morphological thinning. The distance transform calculation is also called medial axis skeletonization (Figure 1.7A). As a first step a distance transform of the binary object is calculated, measuring the distance of every pixel to the closest contour points. The skeleton is then the set of points which have more than one closest point on the object's boundary. This set of points can be visualized as a crevice along the medial axis of the object. To estimate the skeleton by iteratively thinning the object a set of rules is needed which indicate which pixels can be removed in the next step. These rules rely on the amount and distribution of the eight neighbouring pixel. Removing a pixel according to Zhang and Suen, 1984:
If all of these conditions apply, remove this pixel:

- The number of neighbouring nonzero points is between 2 and 6 inclusively
- When going clockwise around the pixel the number of found 0-1 patterns is exactly 1
- In the first iteration: P_2, P_4, P_6 are not all ones. In second iteration: P_2, P_4, P_8 are not all ones.
- In the first iteration: P_4, P_6, P_8 are not all ones. In second iteration: P_2, P_6, P_8 are not all ones.

This process is done iteratively and parallelized until no more pixels can be removed. All methods and implementations have small differences ((Figure 1.7A and B)) and during this dissertation the method of Zhang and Suen (Zhang and Suen, 1984) is chosen when skeletonization is performed.

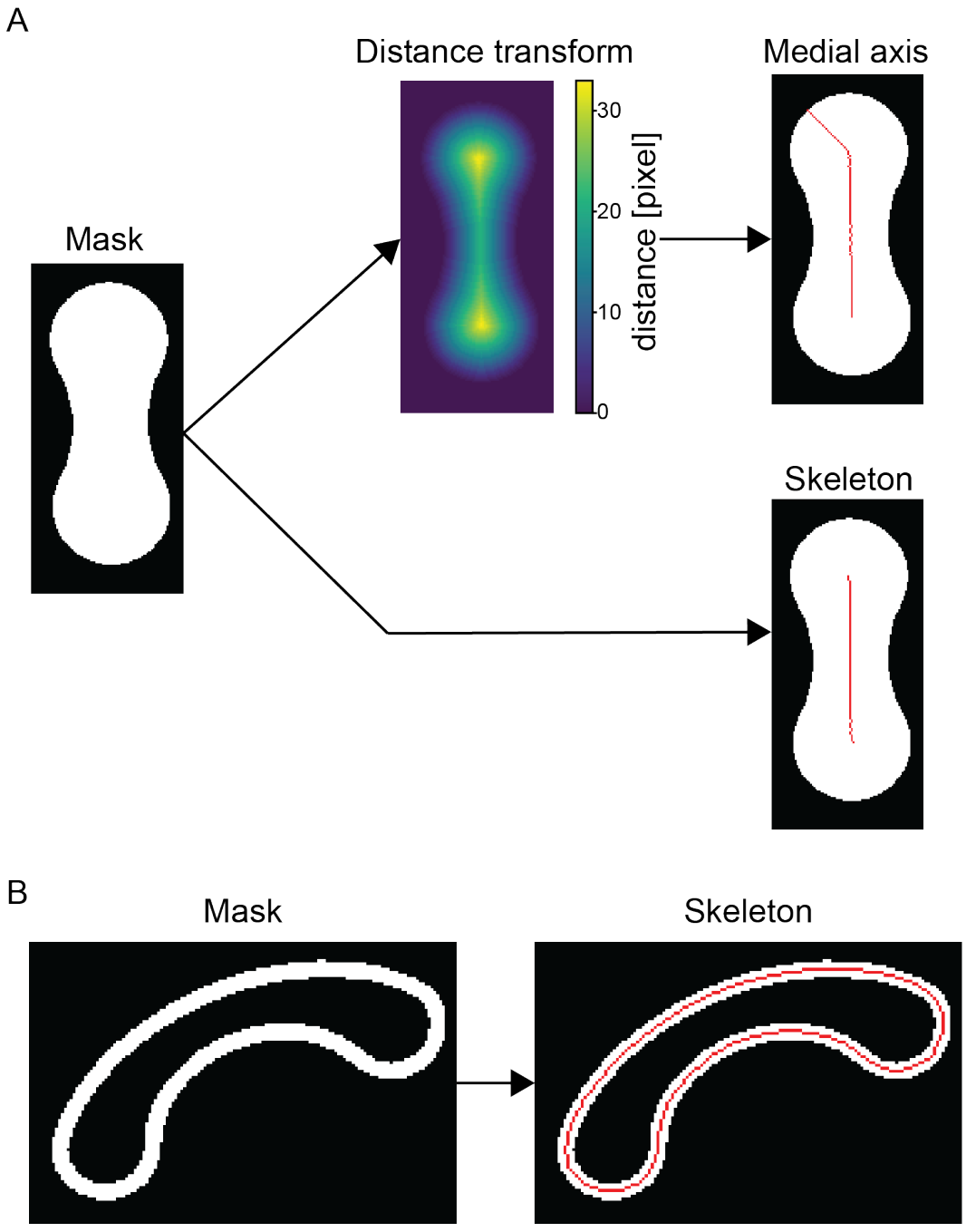

FIGURE 1.7: Illustration of the skeletonization method using simple masks. A: The left image shows a simple binary mask. Calculating its distance transform results in the top middle image showing the distance of each pixel to the nearest contour. Using the medial axis method results in the top right image showing the mask's medial axis in red and a possible problem with the medial axis method by sometimes showing unintuitive results. The bottom right image shows the result of the skeletonization method by Zhang and Suen. B: The left image shows a mask of a typical shape used during this dissertation. The right image shows the closed skeleton of the mask on the left.

Chapter 2

Aims

The overall objective of this work was to develop automated and robust methods for analysis of biological lipid bilayers in cryo electron microscopy data with a focus on vesicles in 2D micrographs. In order to get a better understanding of membrane interactions and the effect of membrane-remodeling proteins, I set out to develop a toolkit for researchers to analyze their membrane images. At first, methods to reliably identify membranes in the images were required. Moreover, batch processing and automation of the analysis of the found membranes by implementing existing property extraction methods as well as developing new methods. Finally, I wish to implement a graphical user interface to aid researchers without any programming knowledge. The toolkit also should be applied to multiple experimental datasets to demonstrate its usefulness. To further help researchers understand membrane remodeling processes, automation for identification of shape changes was desirable. Therefore, I was aiming to develop a method to extract the steps of morphological membrane changes out of hundreds of images to visualize the process using a semi-supervised method involving dynamic time warping. At last, I also aimed to contribute to the growing methods of analyzing membranes in tomograms by estimating the thickness of the bilayer in reconstructed cryoEM volumes.

Chapter 3

Cryo Vesicle Image Analyser - CryoVIA

*The content of this chapter is the main focus of this work explaining the inner workings and results of CryoVIA, a software designed to streamline the analysis of biological membranes as seen in cryo micrographs. Most figures and most of the text were taken from the publication Schönnenbeck, Junglas, and Sachse, 2025 which introduced CryoVIA and published the software. The figures and most of the used text was written by me if not indicated otherwise. All figures and sections from the publication are marked with a * in the figure legend or the section header. Large part of the Materials and Methods section was adjusted, updated and further explained. If sections still contain part of the publication but have been adjusted or some was text was added they are indicated with **. Otherwise if sections and figures are completely new and not present in the publication no * is present in the title or figure legend. Additionally, one section and two figures were taken from the publication Junglas et al., 2025. The according authors were indicated at the the specific segments.*

3.1 Introduction*

Cryo-EM is a powerful tool to study protein-membrane interactions as it provides high-resolution images of vitrified macromolecules under near-native conditions including biological membranes (Kühlbrandt, 2022). Isolated and soluble protein

structures of biological macromolecules are commonly determined to high resolution enabling atomic model building (Subramaniam, Kühlbrandt, and Henderson, 2016). A group of lipid-interacting proteins is capable of deforming lipid membranes and inducing shape changes on lipid membranes through their distinct binding mechanisms (McMahon and Gallop, 2005). Archetypical examples are GTPase driven dynamin or bar-domain proteins that are involved in the cellular membrane-trafficking processes like endocytosis (Daumke, Roux, and Haucke, 2014, Jimah and Hinshaw, 2019). Another important group of membrane-remodelling proteins constitutes the family of endosomal sorting complexes required for transport III (ESCRT-III) that are topologically catalysing budding reactions away from the cytosol. While structures of membrane-remodelling proteins can be determined in isolation, many of them require their biological substrate in order to polymerize (Frost et al., 2008, Skruzny et al., 2015).

A series of membrane-remodelling protein structures have been determined in the presence of lipid membranes using cryoEM (Junglas et al., 2021, Low et al., 2009, Zhang and Hinshaw, 2001). For this purpose, Fourier-Bessel, single-particle or hybrid approaches of image processing approaches for helical reconstruction were employed to resolve the protein structures of the helical lattices formed on lipid membranes (Desfosses et al., 2014, Diaz, Rice William, and Stokes, 2010, Egelman, 2007). In the meantime, widely used single-particle image processing software suites have been adapted to work with helical protein assemblies (He and Scheres, 2017, Punjani et al., 2017). These image processing suites primarily focus their refinement on protein structures. In the case when lipid membranes are tightly bound to the protein structures, lipid density can be observed alongside the protein density (Moss et al., 2023). However, phospholipid bilayers alone also generate significant contrast suitable for detailed analysis of characteristic lipid features and membrane shapes (Heberle et al., 2020). Nevertheless, the localization of such membrane structures and the quantitative evaluation of those features is often performed interactively and remains a subjective as well as labour-intensive task. For

the case of cellular electron tomograms, few automated membrane analysis tools have been put forward (Barad et al., 2023, Martinez-Sanchez et al., 2014, Salfer et al., 2020) while they target to capture the larger scale cellular environment in three-dimensional image volumes.

Quantitative analysis of membrane structure from many micrographs is still a largely manual task as no suitable image processing tools are available. To this end, we developed a cryo vesicle image analysis (CryoVIA) tool to automate membrane structural analysis. The developed toolkit combines neural network-based image segmentation, structure identification with a series of analytical tools to estimate local and global structural properties including the classification of vesicular membrane shapes. We apply CryoVIA to different preparations of vesicles and lipid mixtures of exemplary data sets and reveal modifications to their structural properties.

3.2 Results

3.2.1 Principal workflow of cryoVIA*

In order to generate a quantitative automated workflow suitable for analysing biological membranes from cryo-micrographs, we created CryoVIA that requires electron micrographs as input and concludes with analytical data plots. The workflow is divided into three basic parts: neural-network based segmentation, membrane structure identification, and structure analysis (Figure 3.1). For the first part of the toolkit, the given micrographs are segmented to locate the membrane structures of interest that are subsequently used for further analysis. We applied segmentation using a pre-trained U-net with micrographs including user-provided membrane structures as input (Ronneberger, Fischer, and Brox, 2015) and found membranes across micrographs consistently labelled. By default, a pre-trained U-Net is used, while some use cases may require to re-train the U-Net on manually segmented micrographs.

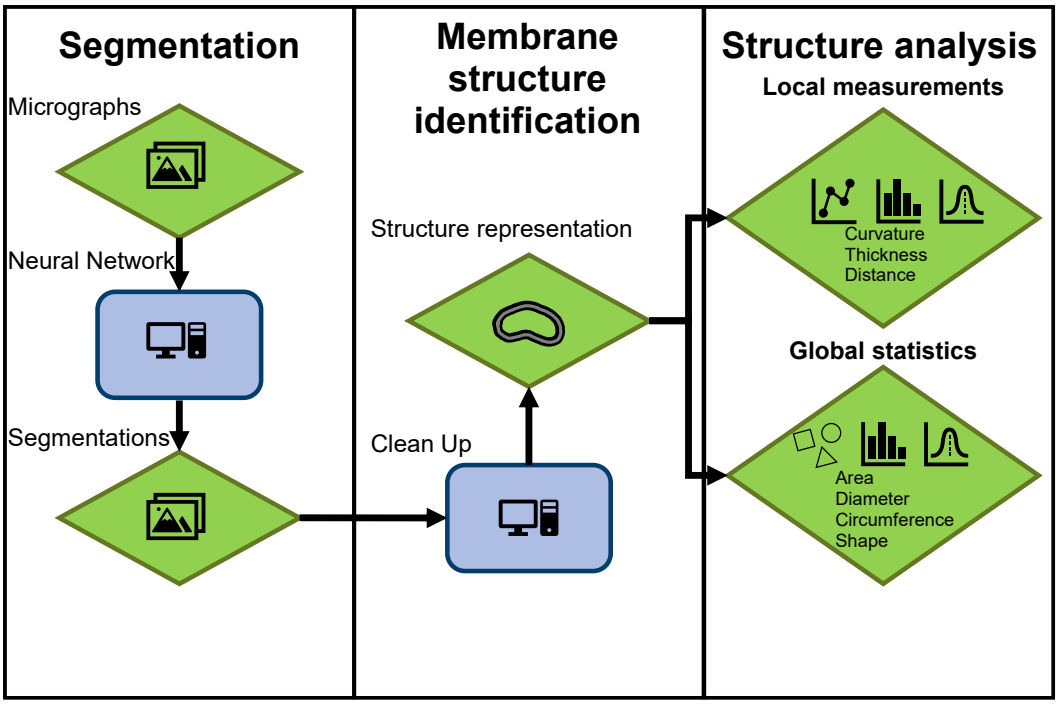

FIGURE 3.1: *Cryo-micrographs serve as input for the U-net based segmentation that is followed by a membrane structure identification. This step assigns unique and single membrane entities and is critical to single out overlapping membrane structures. In the final step, the identified membrane structures are subjected to a detailed quantitative analysis for the extraction of local and global structural parameters.

3.2.2 Identification of membrane features**

The second part of the toolkit refers to the membrane structure identification that will generate membrane entities based on the segmentation results from the first part. The results of the binary segmentation are used to identify independent instances of membrane structures within one micrograph by simply splitting the segmentation into independent connected components. This approach works well when membrane structures are well separated in one micrograph, however, when the target structures are crowded and membranes overlap, they require additional separation routines. Overlapping membrane structures are located and re-connected by monitoring the continuity of local membrane structures (see 3.4 for details). For presenting the principal functional features of CryoVIA, we, initially, use a test data set containing 356 cryo-micrographs of DOPC vesicles that were size-filtered by a 200 nm cutoff. As a result of the feature identification, the initially segmented skeletons are successfully separated by restraining subsequent angles into individual membrane structures (Figure 3.2A).

For detailed and consistent analysis of the identified membrane structures, refinement of the initially detected pixel positions is essential to obtain accurate membrane contours located at the center of each membrane bilayer (Figure 3.2B). For this purpose, we convolve the image with a bilayer-like kernel and subsequently employ the Frangi filter (Frangi et al., 1998) (see 3.4 for details). As a result of the membrane structure identification, the curated membrane contours are available for detailed analysis of the membrane structures. As an optional step, it is also possible to remove identified membranes outside of grid foil holes using a circle convolution (3.19). After identification of the foil hole edges, localized membrane structures outside of the holes can be effectively removed and the relevant membrane features are ready for subsequent in-depth data analysis. In summary, through a series of refinement and pruning steps, segmentation results are enhanced for the following analysis of structural features.

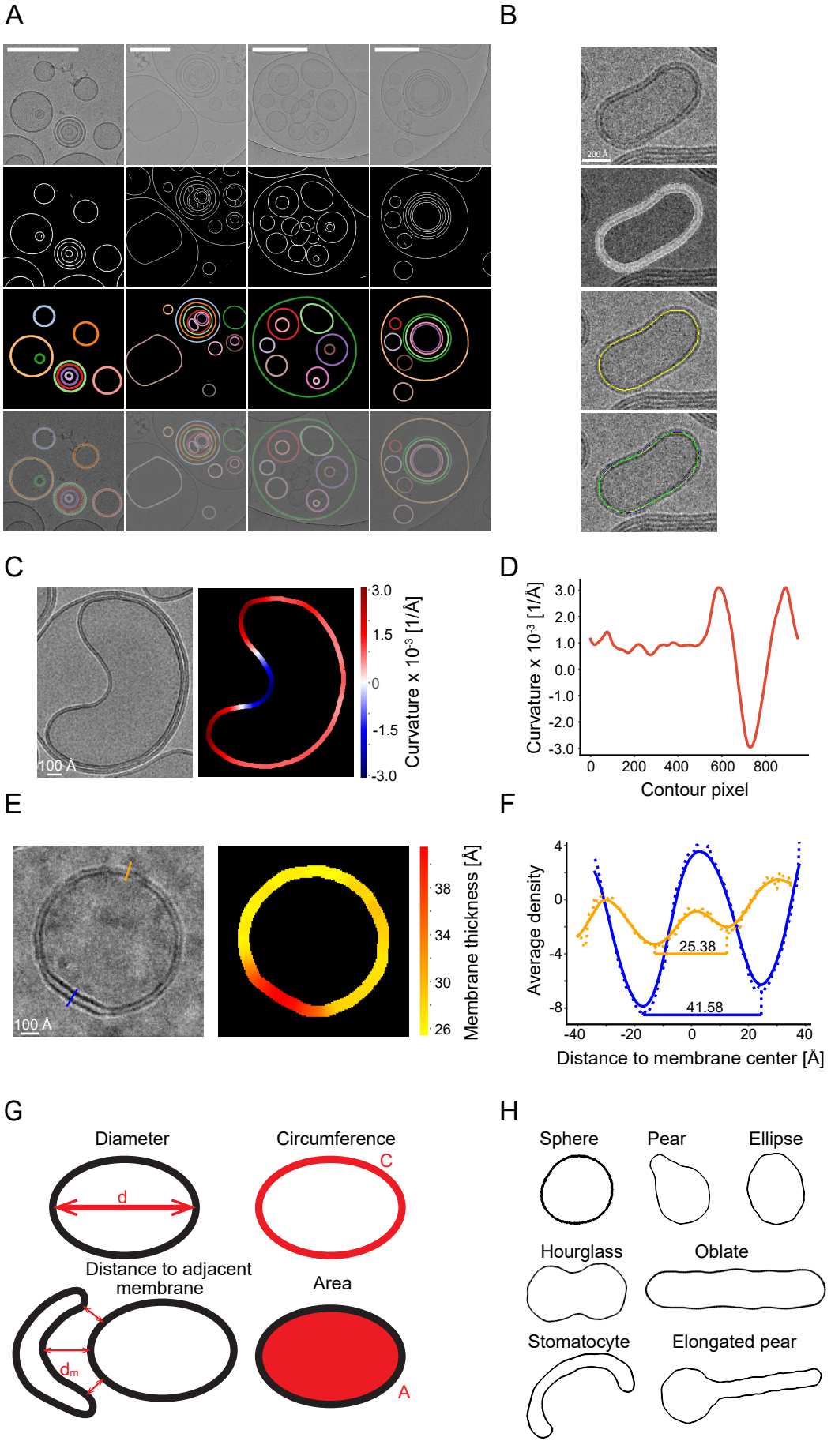
A
B
C
100 Å
3.0
1.5
0
-1.5
-3.0
Curvature x 10⁻³ [1/Å]
D
Curvature x 10⁻³ [1/Å]
3.0
2.0
1.0
0.0
-1.0
-2.0
-3.0
0
200
400
600
800
Contour pixel
E
100 Å
38
34
30
26
Membrane thickness [Å]
F
Average density
4
0
-4
-8
25.38
41.58
-40
-20
0
20
40
Distance to membrane center [Å]
G
Diameter
d
Circumference
C
Distance to adjacent membrane
dm
Area
A
H
Sphere
Pear
Ellipse
Hourglass
Oblate
Stomatocyte
Elongated pear

FIGURE 3.2: *(A) From top to bottom rows: Four micrographs of the dataset DOPC (200 nm size filtered) containing different lipid structures (top). The corresponding U-net based segmentation (top center). The results of membrane identification (bottom center). Segmentation results superimposed on original micrographs (bottom). Only closed vesicles were extracted from the segmentation. Scale bar 200 nm. (B) From top to bottom: Magnified image of vesicle (top). Segmentation of the corresponding vesicle: multiple pixels are covering the bilayer (top center). One pixel-wide initial skeleton of the segmentation in yellow (top bottom). Skeleton in yellow, corrected skeleton in blue, pixels where skeleton and corrected skeletons are identical in green (bottom). (C) Example stomatocyte vesicle from the DOPC 200 nm size-filtered data set (left) with curvature values superimposed on segmented membrane (right). (D) Curvature of C plotted as a function of contour pixels. (E) Example vesicle from the DOPG/DPPG data set with two cross sections in blue and orange (left) with membrane thickness estimates superimposed on segmented membrane (right). (F) Extracted (dashed line) and smoothened (solid) density profiles from the corresponding cross section locations in E blue and orange, respectively. (G) Global parameters extracted are diameter, circumference, distance to adjacent membranes, and area. (H) Possible membrane shapes from membrane structures are: spheres, pears, ellipsoid, hourglass, oblate, stomatocyte, and elongated pear. These shapes are used for the training of the default shape classifier later (see also Figure 3.9).

3.2.3 Quantitative extraction of local and global membrane features*

As the final part of the CryoVIA workflow, we perform structure analyses for each membrane contour using the information from the identified pixels. Measurements for each contoured pixel such as curvature, bilayer thickness, and distance to other membrane segments are obtained locally. Global statistics about the membrane structure such as length, area, diameter are directly derived from the membrane contours. Finally, shape classifications are employed for large-scale and intuitive comparisons of different experimental data sets.

In order to describe local shape changes of the membrane contours, we make use of the curvature descriptor. Curvature is defined as the reciprocal radius of a circle that best describes the local curve. The higher the curvature, the higher is the local shape changes of the membrane while a curvature of zero corresponds to a straight line. In addition, the direction of the curvature is calculated and represented by the

sign of the curvature value. For closed membranes (e.g., vesicles), convex regions of the membrane have a positive curvature value while concave regions will assume a negative value. Based on a local measurement, it is not possible to distinguish between convex and concave curvature in membrane segments, as they require the topological information of the entire membrane entity. In the following analysis only completely closed membranes - vesicles - are considered and analysed. The calculated curvature values are presented in two dimensions superimposed on the micrograph or as a function of the contour length (Figure 3.2C/D).

Another important local membrane parameter is the underlying bilayer thickness or leaflet separation reflecting the physical properties and chemical composition of the membrane (Heberle et al., 2020). For bilayer thickness estimation, the averaged local cross sections of the bilayer density are extracted and smoothened by a Gaussian filter until two distinct minima can be identified. The distance between these minima is estimated as the bilayer thickness (Figure 3.2E/F). Due to the inherent noise in cryoEM images, the estimated thickness values along the contour of the vesicle are additionally smoothened by a Gaussian filter. The bilayer thickness is estimated for each contour pixel of the vesicle locally as well as averaged over one membrane structure, e.g., for one vesicle.

Global structural parameters such as diameter, circumference, and area of each identified membrane structure are directly extracted based on the membrane contours according to their geometric definitions (Figure 3.2G). Moreover, distances to other membrane structures are also determined, e.g., for cases when vesicles contain additional enclosed vesicles. Membranes and vesicles occur in a wide variety of shapes, therefore, classification or clustering into different classes is desirable for further analysis. As self-contained membrane structures can only assume a limited set of shapes (Döbereiner, 2000), they are classified by a small one-dimensional convolutional neural network using simulated reference shapes. Based on our most frequent shape observations, we designed the default classifier to distinguish seven

shapes including sphere, prolate, tube, pear, stomatocyte, hourglass, and an elongated pear (Figure 3.2H). The shape classification makes use of the fact that the curvature along the contour of the vesicle has a distinct profile for each shape. To perform classification, the curvature contour of a given vesicle is length-normalized by resizing the curvature values to a predefined vesicle size, interpolating to a fixed number of data points and the values are shifted to start with the lowest value. The length-normalized values can then be used by the classifier. The default classifier identifies the test shapes with an accuracy of 98.6% after training on a set of 200 instances for each shape (Figure 3.3). In addition, it is possible to add custom shapes to classify specific vesicles after user definition using the provided GUI.
In the following analysis only completely closed membranes - vesicles - were considered and analysed. The calculated curvature values are presented in two dimensions superimposed on the micrograph or as a function of the contour length (Figure 3.2CD/DE).

3.2.4 Errors in curvature and bilayer thickness estimation*

To estimate the precision of the local curvature estimation, we used another test data set of DOPC sonicated vesicles. We compared the local measurements with segmentation-based global parameters that are generally of higher reliability. For this purpose, we looked at 500 ideal vesicles of highest circularity and of diameters of >1000 Å. The circularity was estimated by global segmentation parameters $(4 * Area * \pi)/(Perimeter^2)$ with 1 being a perfect circle and 0 being highly non-circular shapes, which we consider to be a reliable measurement. Next, we estimated the curvature locally and circle radii for every point of the vesicle using six different neighbourhood sizes (50, 100, 200, 300, 400, and 500 Å, respectively) and subsequently calculated the difference between these locally estimated radii and the globally derived radii (Figure 3.4A). The errors obtained with large neighbourhood sizes of 200, 300, 400, and 500 are small at 6.3, 3.4, 2.8, and 2.6 Å,

respectively. When using small neighbourhood sizes of 50 and 100 Å, the mean error in the curvature estimation was substantially higher at 44.8 Å and 18.1 Å, respectively, presumably due to the increase of noise over signal available for radii fitting. While small neighbourhood sizes can detect radius changes more locally, they are more prone to overfitting in the presence of higher noise levels in the measurements. As a compromise between precision of the curvature estimation and locality of the detectable features, we chose a default neighbourhood size of 200 Å. To evaluate the error of the bilayer thickness estimation, we examined the forward difference of the estimated bilayer thickness values. For the same 500 most circular vesicles described above, the mean difference and standard deviation corresponded to 0.14 Å and 0.17 Å, respectively. Based on these considerations, bilayer thickness of the DOPC vesicles can be estimated quite precisely with an error to about 0.2 Å. To further reduce the impact of noise in the micrograph and the limitation of pixel accuracy, we smoothened the estimated thickness values along the contour with a Gaussian kernel of sigma 2 (Figure 3.4B). The analysis of the 500 vesicles yielded a mean bilayer thickness of 28.2 Å and a standard deviation of 1.8 Å. The higher standard deviation than the estimated error above is likely due to actual variation in membrane thickness. In previous studies on DOPC bilayer thickness estimation of 50-60 non-spherical vesicles recorded at the same defocus of 2.0 µm errors were estimated between 3.0 and 4.0 Å (Heberle et al., 2023). In comparison, we obtain a slightly smaller but still very similar variance in the thickness.

3.2.5 Analysis of Validation dataset*

In order to comprehensively test the capabilities of CryoVIA, we compared multiple size preparations of unilamellar vesicles made of DOPC and DOPG/DPPG (70/30) lipids that are known to give rise to different ultrastructures. For the first sample, we considered the sonicated DOPC vesicles, and for the second and third, we assigned DOPC 50 nm and 200 nm size-filtered preparations, respectively. For the

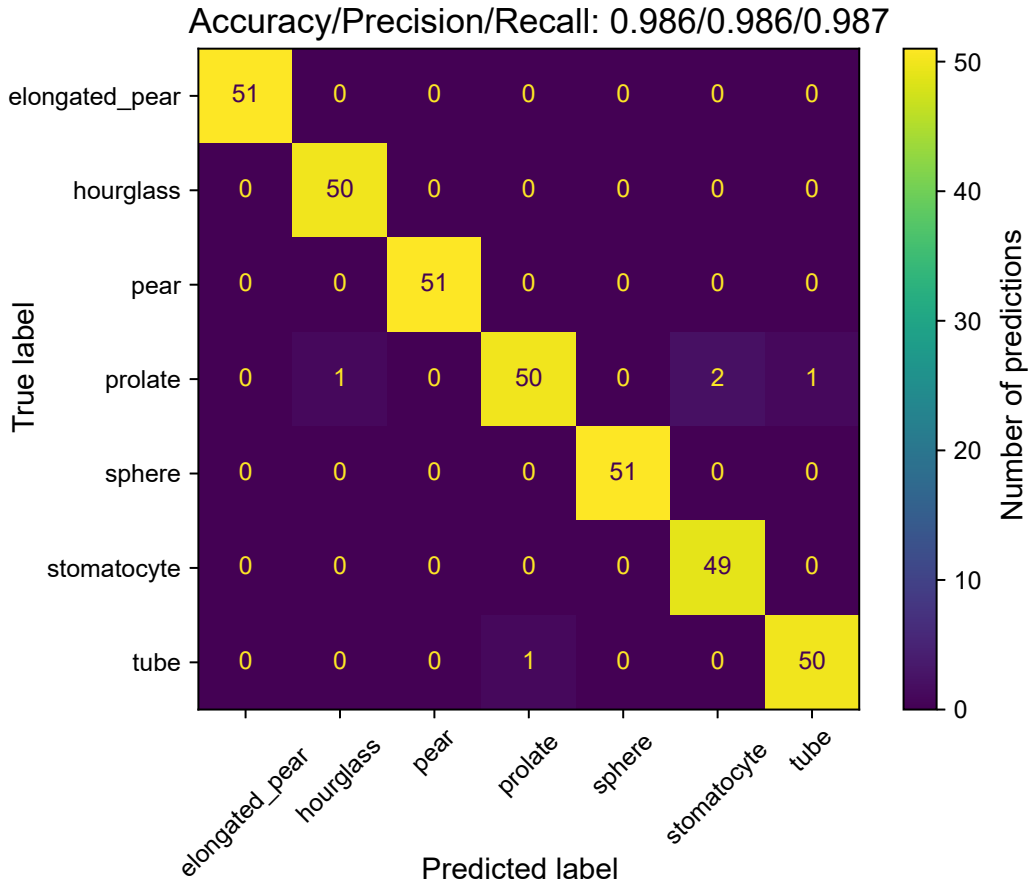

FIGURE 3.3: *Confusion matrix and classification metrics accuracy, precision, and recall for the default shape classifier trained on seven different shapes.

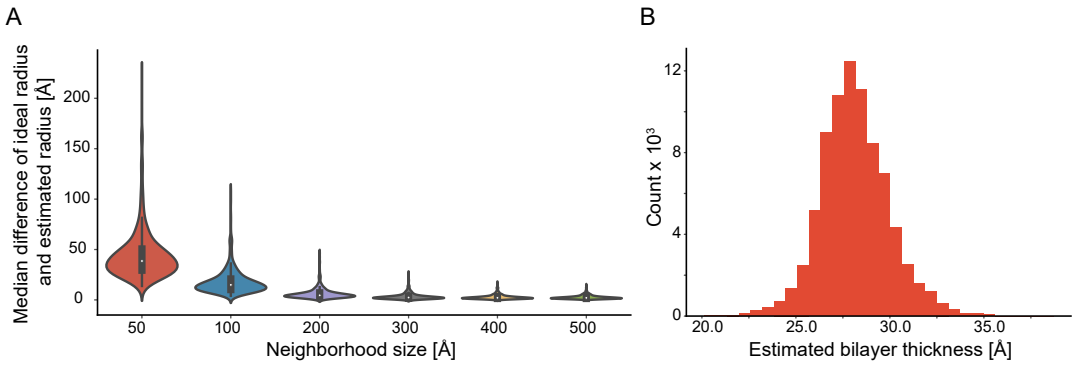

FIGURE 3.4: *Error estimation of curvature and bilayer thickness determination in a DOPC sonicated data set using the 500 most circular vesicle contours found. (A) Median of difference between the globally estimated vesicle radius (ideal) and the locally determined (estimated) curvature radius using different maximum neighbourhood sizes for curvature estimation. For neighbourhood sizes larger than 200 Å the errors are smaller than 6 Å. (B) Bilayer thickness estimations of all contour points yield a distribution of 28.2 ± 1.8 Å. One standard deviation of the mean accounts for 72.4 % of included values.

fourth sample, we generated vesicles from a DOPG/DPPG (70/30) mixture. For each of the samples, we prepared plunge-frozen cryo-samples and recorded between 251 and 909 micrographs (see Table 3.1). Each data set was segmented by a U-net specifically trained to detect densely packed vesicles. In the four data sets, a total of 48,938 vesicles were reliably identified, while only fully closed membrane structures were considered. The detected vesicles of each data set were manually examined and discontinuously segmented or incorrectly identified vesicular structures were discarded. Incorrectly detected membranes often have unrealistic sharp bents in the contour and can, therefore, be identified by their very high curvature values. The GUI provides an easy way for sorting according to high curvature and quickly removing the segmentations by a threshold value. For each data set, the average amount of detected vesicles per micrograph varied. In micrographs of sonicated DOPC vesicles, the highest frequency of vesicles per micrograph (42.8 on average) were found due to the small circular vesicles. For the 50 and 200 nm DOPC data sets, the micrographs were often densely packed while the toolkit managed to identify on average 24.1 and 5.1 vesicles per micrograph, respectively whereas the DOPG/DPPG vesicle preparation only had an average of 4.2 vesicles

	Maximum	Minimum	Mean	Median	Median absolute deviation
Circumference [Å]					
DOPC sonicated	15,897	388	961	654	189
DOPC 50 nm size-filtered	8,563	402	1,758	1,466	579
DOPC 200 nm size-filtered	12,566	402	3,117	2,263	1,356
DOPG/DPPG (70/30)	23,473	406	3,077	2,368	1,027
Diameter [Å]					
DOPC sonicated	6,052	124	309	209	58
DOPC 50 nm size-filtered	3,040	126	575	465	189
DOPC 200 nm size-filtered	4,374	126	1,041	744	458
DOPG/DPPG (70/30)	7,364	134	960	737	315
Area [nm^2]					
DOPC sonicated	125,508	104	1,102	302	154
DOPC 50 nm size-filtered	41,469	106	2,875	1,495	1,027
DOPC 200 nm size-filtered	89,825	114	9,941	3,453	3,020
DOPG/DPPG (70/30)	392,323	118	10,793	3,995	2,979

TABLE 3.1: Size statistics of the liposome datasets

per micrograph.

When we computed global parameters of circumference, diameter, and area (see Table 3.3, Figure 3.5A, Figure 3.9A, B), we found the that the determined circumferences of vesicles in the sonicated DOPC data set are on average smaller with a median circumference of 651 ± 189 Å median absolute deviation (m.a.d.) than in the data sets of the 50, 200 nm size-filtered DOPC and DOPG/DPPG at 1466 ± 579 Å m.a.d., 2263 ± 1356 Å m.a.d. and 2368 ± 1027 Å m.a.d., respectively. When

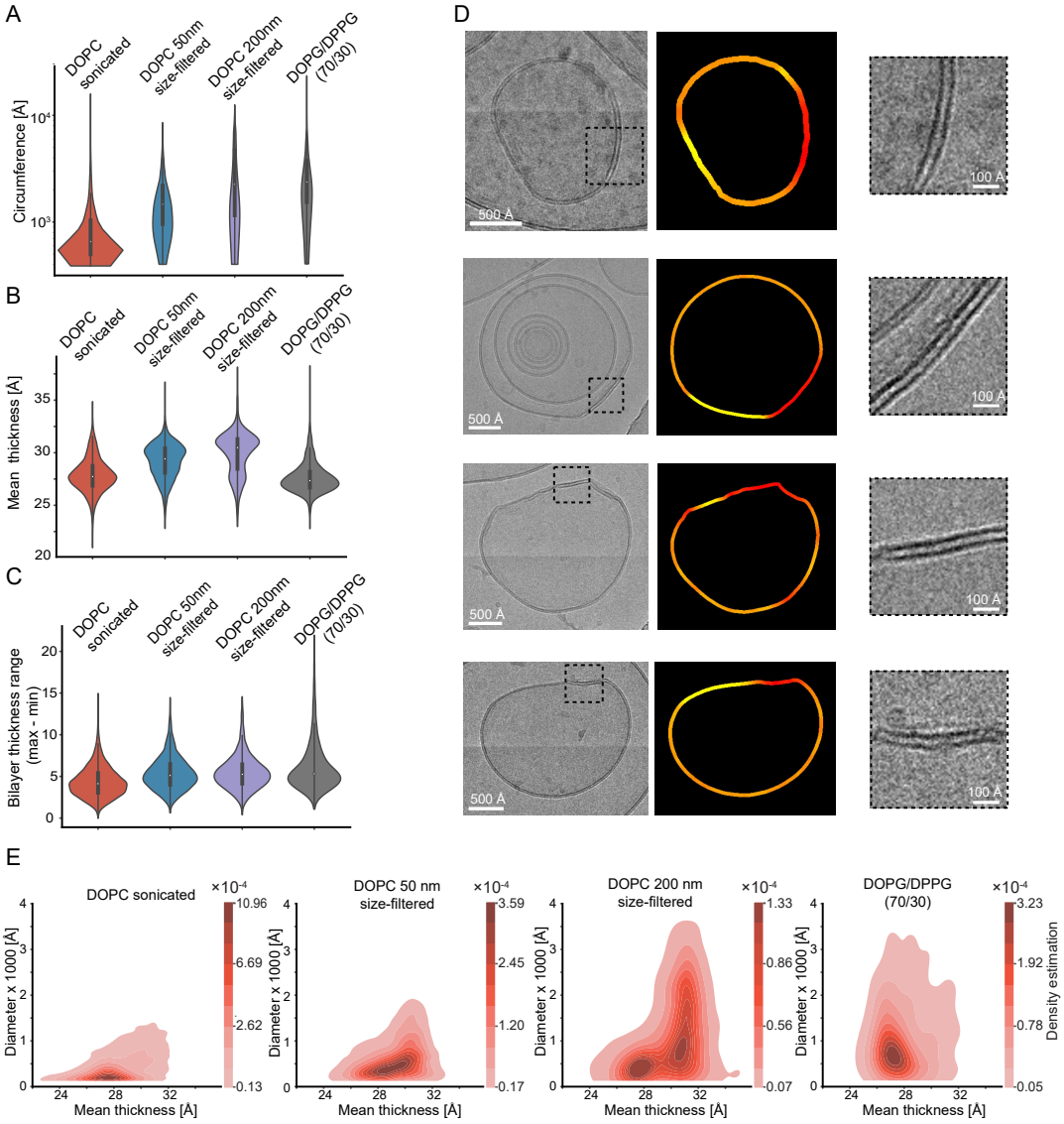

FIGURE 3.5: *Determined quantities of circumference, diameters, and membrane thickness from four lipid samples. (A - C) Violin plots of the evaluated vesicles from four data sets (DOPC sonicated (n = 38871), DOPC 50 nm size-filtered (n = 6061), DOPC 200 nm size-filtered (n = 1819), and DOPG/DPPG (70/30) (n = 2179)) with circumference (A), mean bilayer thickness distribution (B) and range (C). The white dot within each violin indicates the median, while the shaded area represents the kernel density estimate of the data distribution. The inner grey box represents the 2% to 75% interquartile range, while the vertical grey line includes values inside the interquartile range multiplied by 1.5. (D) Example images for high bilayer thickness of the DOPG/DPPG data set. The vesicle image with a dashed box indicating the region of zoomed inset (left). The thickness map along the segmented contour from yellow to red with red being the highest thickness (center). Zoomed membrane segment with the highest thickness value (right). (E) Kernel density distribution plots of diameter against the mean bilayer thickness. The density values of each distribution are normalized in such a way that the sum equals 1 (see also Figure 3.9).

inspecting the determined diameters of the 50 and 200 nm size-filtered DOPC vesicles, the median diameters differ from 465 ± 189 Å m.a.d. to 744 ± 458 Å m.a.d., respectively, which is in agreement with the chosen polycarbonate size filters for the vesicle preparations. The presence of vesicles with maximum diameters up to 3040 and 4374 Å larger than the size filters of 50 and 200 Å, respectively, reveals that a considerable amount of large diameter vesicles was not removed by the filter presumably due to the fluid and deformable properties of the lipid membranes. The sonicated DOPC vesicles showed a median diameter of 209 ± 58 Å m.a.d. while the DPPG-DOPG data set had a similarly high median diameter as the 200 nm DOPC vesicles with a median diameter of 737 ± 315 Å m.a.d. The obtained results including the deviations from the sonication-only data set are in agreement with previous studies as sonication produces on average smaller vesicles (Nizamudeen et al., 2021). Together, CryoVIA is capable of automatically determining global size statistics of multiple lipid vesicle preparations from a large number of cryoEM micrographs.

In order to further characterize the local membrane properties of the chosen test samples, we performed detailed membrane analysis as part of CryoVIA. As a result, we found that the average of the mean bilayer thickness of sonicated DOPC vesicles and the DOPG/DPPG vesicles with 27.5 Å and 27.2 Å was smaller than in the 50 and 200 size-filtered DOPC samples at 29.0 and 30.5 Å (Figure 3.5B), which is likely a direct result of the filter treatment of sonicated DOPC vesicles. For DOPG/DPPG vesicles, the observed difference between the maximum and minimum bilayer thickness was higher at 22 Å than for the DOPC vesicles at 15 Å (Figure 3.5C), suggesting larger local structural changes, possibly due to the presence of unsaturated DPPG molecules. Inspection of DOPG/DPPG vesicles identified with high bilayer thickness supports the measured quantities visually (Figure 3.5D). Relating the bilayer thickness with diameter revealed an overall correlation between the two quantities for the vesicles taken from the four data sets (Figure 3.5E). Interestingly, sonicated DOPC as well as DOPG/DPPG samples showed a more focused

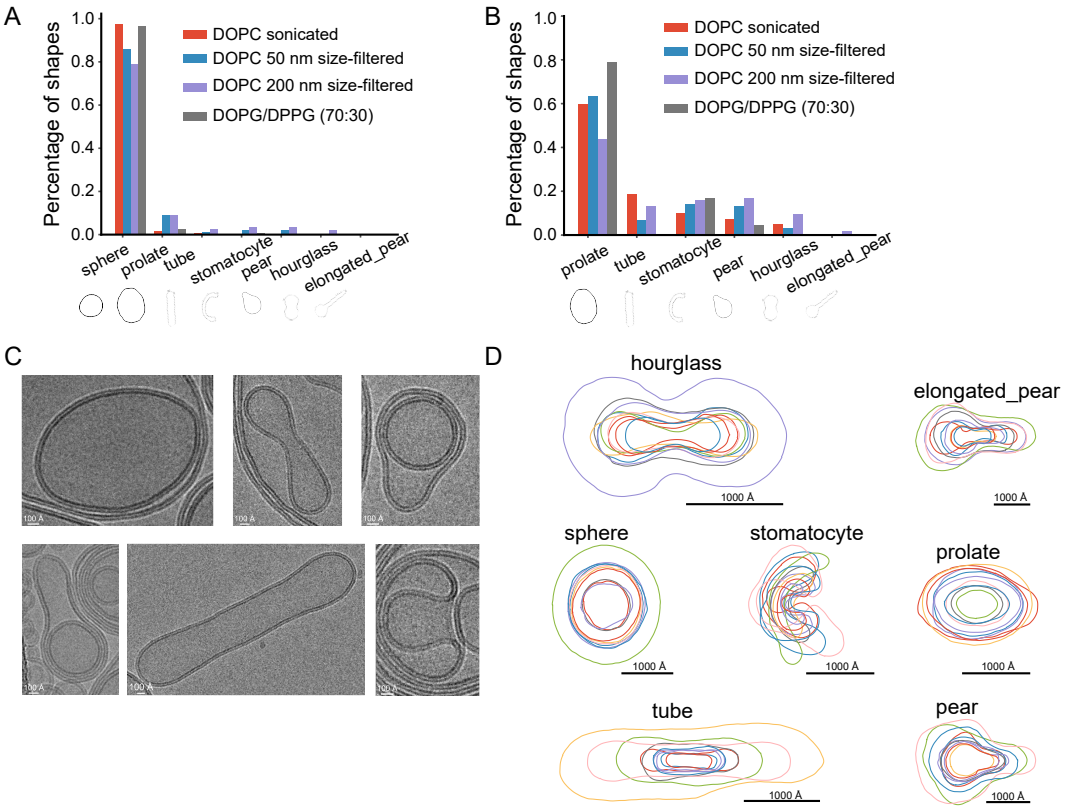

FIGURE 3.6: *Shape classification of sonicated, 50 and 200 nm size-filtered DOPC and DOPG/DPPG vesicles. (A) Bar graph of the shape distribution of the four data sets. (B) Bar graph of the shape distribution of all data sets excluding spheres as they make up the majority of shapes. (C) Example vesicle images of shapes found in micrographs. From top left to bottom right: prolate, hourglass, pear (from DOPC 200 nm sample, respectively), elongated pear (DOPC sonicated), tube (DOPC 200 nm) and stomatocyte (DOPC sonicated). (D) A total of 7 classified shapes, 10 aligned and superimposed experimentally segmented vesicle contours. The 10 vesicles with the highest confidence for each shape in the shape classification are displayed (see also Figure 3.9).

distribution of diameter with bilayer thickness whereas the size-filtered data sets show a more continuous distribution of vesicles.

In order to further characterize the shapes of the four vesicular samples, we clustered them using the pre-trained default CryoVIA shape classifier. For the four samples, the most prominent shape was the spherical vesicle, in particular for sonicated DOPC and DOPG/DPPG vesicles as they made up more than 95% of all vesicles (Figure 3.6A). The 50 and 200 nm size-filtered DOPC samples showed more shape diversity as other shapes took up more than 13 and 20% share, respectively. The

	EPL SUVs	EPL + PspA
Pixel size (Å/pix)	0.681	0.681
# Frames	50	50
Total dose (e^{-}/Å^{2})	30-32	30-32
Underfocus (µm)	2.0-3.0	2.0-3.0
# Movies	1,525	1,531
# Closed vesicles detected	1,576	2,773
# Closed vesicles detected per micrograph	1.0	1.8

TABLE 3.2: PspA data acquisition

majority of the remaining vesicles were classified as prolates that tended to be close to spherical as well (Figure 3.6B). Examples of classified shapes were inspected and overlaid onto each other (Figure 3.6C/D) as well as a small share of unusual shapes not found in the default training set (Figure 3.9C). The complete analysis of the 2031 micrographs took 3.5 hours and a total of 48,930 vesicles were identified and analysed (see methods). In conclusion, CryoVIA reliably extracted local membrane characteristics and consistently classified the majority of the shapes of the four differently prepared vesicle data sets.

3.2.6 Membrane remodelling effects of bacterial ESCRT-III member PspA**

Hypothesized effect of PspA on liposome formation*

To further test the utility of the developed CryoVIA tools on cryoEM data obtained from protein lipid mixtures, we turned to a previously characterized preparation of small unilamellar vesicles (SUVs) from E. coli polar lipid extract (EPL) incubated with the bacterial ESCRT-III protein PspA (Junglas et al., 2021). Previously, it was observed that upon addition of PspA the SUVs were converted into larger vesicles in comparison with the control of EPL alone and that bilayer thickness increased for large vesicles.

Data analysis with CryoVIA*

Initially, we benchmarked the capabilities of the pre-trained network. Prior to segmentation, high-pass filtering was applied to compensate for the strong contrast effects of the lacey carbon foil. This way, a total of 50 randomly selected micrographs were segmented with the provided pre-trained network. Based on the 160 manually curated reference vesicles, the pre-trained neural network detected 146 correctly while only 8 had been missing, reaching an accuracy of 0.91. The small fraction of missing vesicles is composed of non-closed vesicles. While the average circumference of membranes was similar between EPL SUVs and EPL + PspA samples, the data set containing PspA generated membranes of larger lengths (Figure 3.8A). When focusing the analysis on membranes with a circumference greater than 5000 Å (Figure 3.9D), the difference between the largest vesicles/membranes in both data sets became more apparent. While the length of EPL SUV membranes rarely exceeded 6000 Å, the EPL membranes including PspA were mostly found evenly distributed between 5000 and 8000 Å with a tail fraction even longer than 10,000 Å. This analysis was limited by the fact that a lot of the membrane structures were larger than the dimensions of the micrographs and were, therefore, not automatically analysed due to the non-closed entity present on the micrograph (Figure 3.7A). By contrast, in the respective publication (Junglas et al., 2021), the authors had annotated membranes with a length of over 15,000 Å by fitting an ellipsoid shaped vesicles the beyond the micrograph, which we did not implement in CryoVIA. Nevertheless, the clear trend in size difference between EPL SUVs and EPL+PspA as a result of PspA-mediated membrane fusion was confirmed by the CryoVIA workflow.

When analysing the mean bilayer thickness of the two data sets (Figure 3.8B), at first sight the bulk distribution looked very similar with a mean thickness of around 30 Å and most values found 25-35 Å. Nevertheless, the EPL+PspA sample had an additional distribution of membranes with a bilayer thickness of around 45-55 Å.

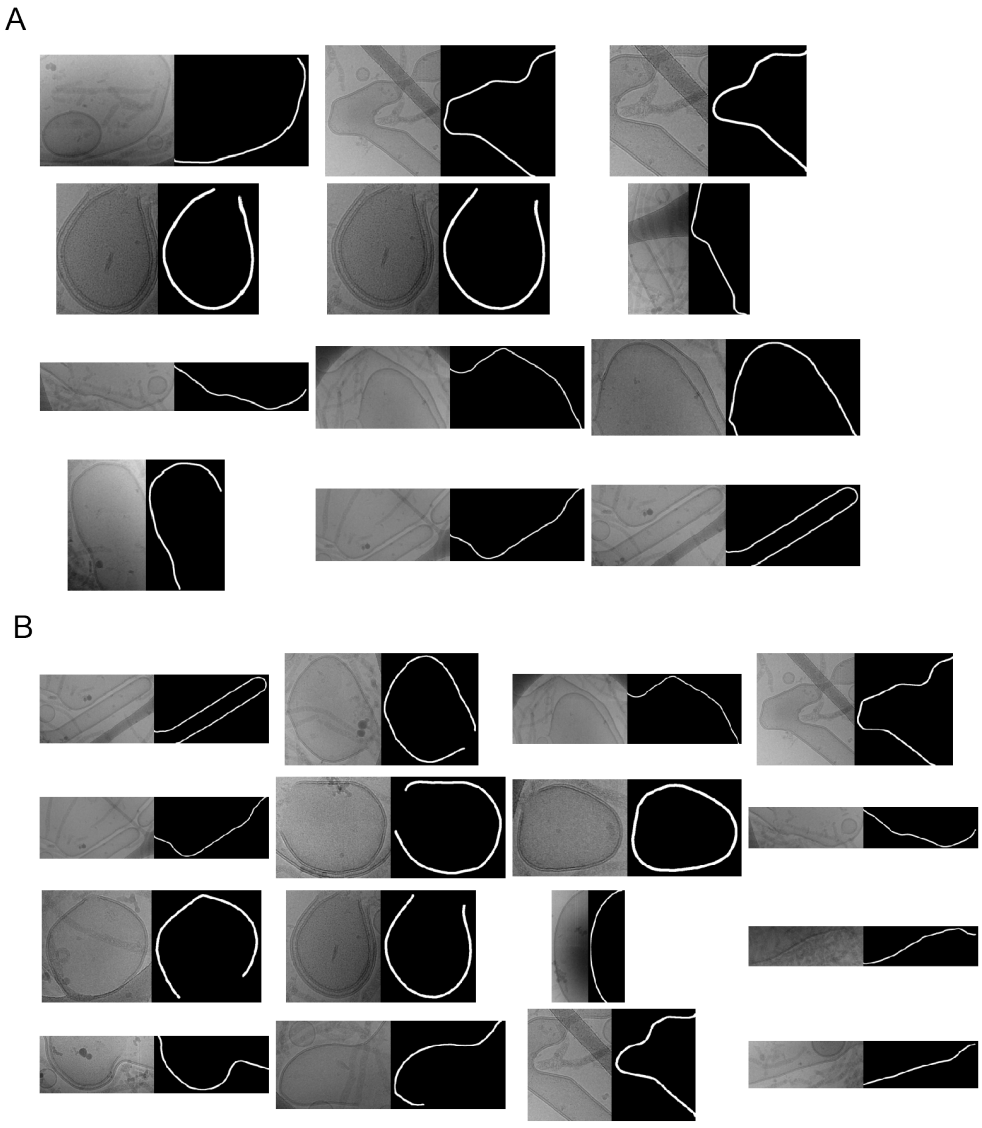

FIGURE 3.7: *Gallery of EPL+PspA micrographs with membranes larger than the micrograph. (A) Some cropped non-closed membranes of the PspA data set with a length greater than 5000 Å. (B) Some cropped membranes of the PspA data set with a bilayer thickness greater than 45 Å.

When we examined the bilayer thickness of membranes with a length greater than 5000 Å (Figure 3.9D/E), we detected a shift towards a greater thickness in the PspA data set with a mean of 42 Å compared to the new mean of 33 Å in the EPL SUV data set, thus confirming the reported conclusions that larger vesicles on average possess an increased bilayer thickness (Junglas et al., 2021). Moreover, when correlating the mean bilayer thickness with circumference a second population emerged with bilayer thickness greater than about 45 Å mostly found in vesicles of large circumference (Figure 3.8C/D). It should be noted most of the large circumference membranes with a thicker bilayer exceeded the dimensions the micrograph (Figure 3.7B) and thus limiting the precise reporting of this apparent structural property. For more precise reporting and analysis through CryoVIA, lower magnification micrographs with larger fields of views will more accurately capture structural changes of large membrane entities. We demonstrated that CryoVIA can be successfully employed to protein lipid mixtures in order to characterize the protein-induced membrane remodelling effects on lipids.

ATP enhances PspA-induced membrane remodeling

This section and the two Figures 3.10 and 3.11 were directly taken from the co-authored publication Junglas et al., 2025. The section and the two Figures were written and prepared by Dr. Benedikt Junglas and Esther Hudina in equal amount. Both allowed me to use the part of the publication in my thesis. The PspA used in this publication is a slightly modified variant of the previously studied PspA protein.

To assess the consequences of the structural plasticity of PspA in the context of membrane remodelling, we analysed the cryo-images for structural and morphological changes of added EPL SUVs and the effect of ATP under reconstitution conditions developed for optimal tubulation (50 nm SUVs and in situ refolding) (Figure 3.10a). After incubation with PspA, we observed PspA rods engulfing and tubulating membranes (Figure 3.10b). Notably, PspA rods engulfing membranes did not have uniform diameters. Instead, they were frequently attached to vesicles

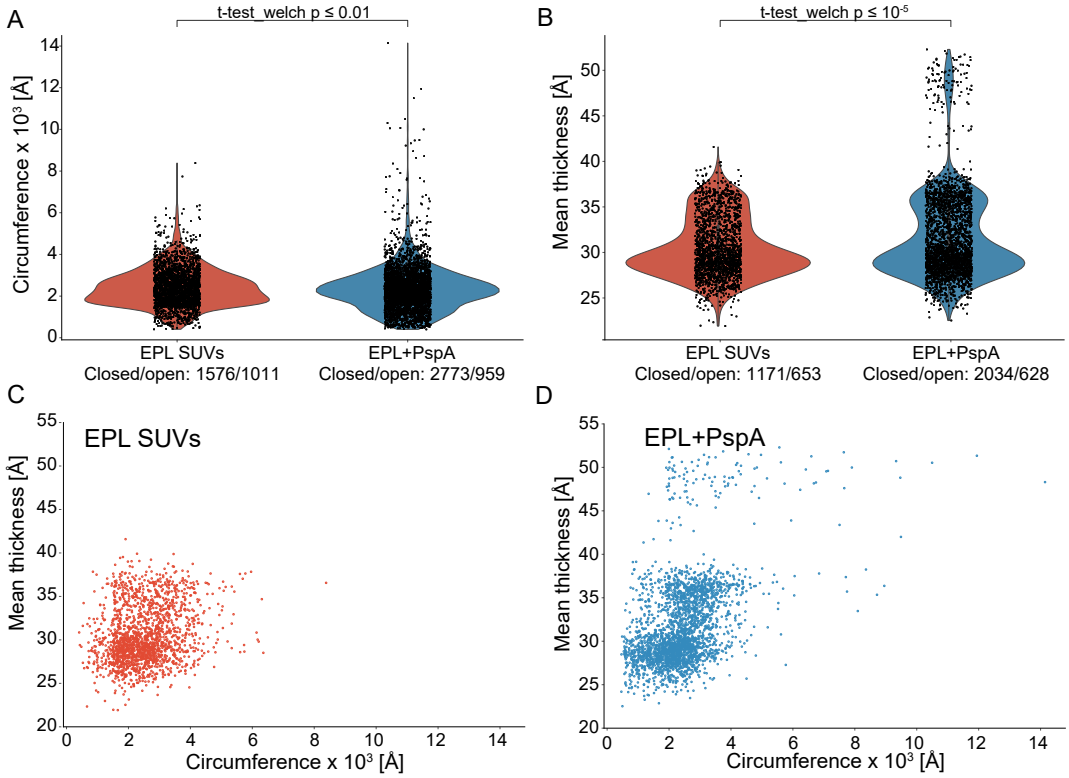

FIGURE 3.8: *Membrane remodelling analysis of the EPL+PspA dataset. (A) Violin plot of the membrane length distribution. (B) Violin plot of the mean bilayer thickness distribution. (A, B) The white dot within each violin indicates the median, while the shaded area represents the kernel density estimate of the data distribution. The inner grey box represents the 25% to 75% interquartile range, while the vertical grey line includes values inside the interquartile range multiplied by 1.5. The sample size is noted below the label. (C) Scatter plot of mean bilayer thickness against circumference of the EPL SUVs data set (D) Scatter plot of mean bilayer thickness against circumference of the EPL + PspA data set (Figure 3.9).

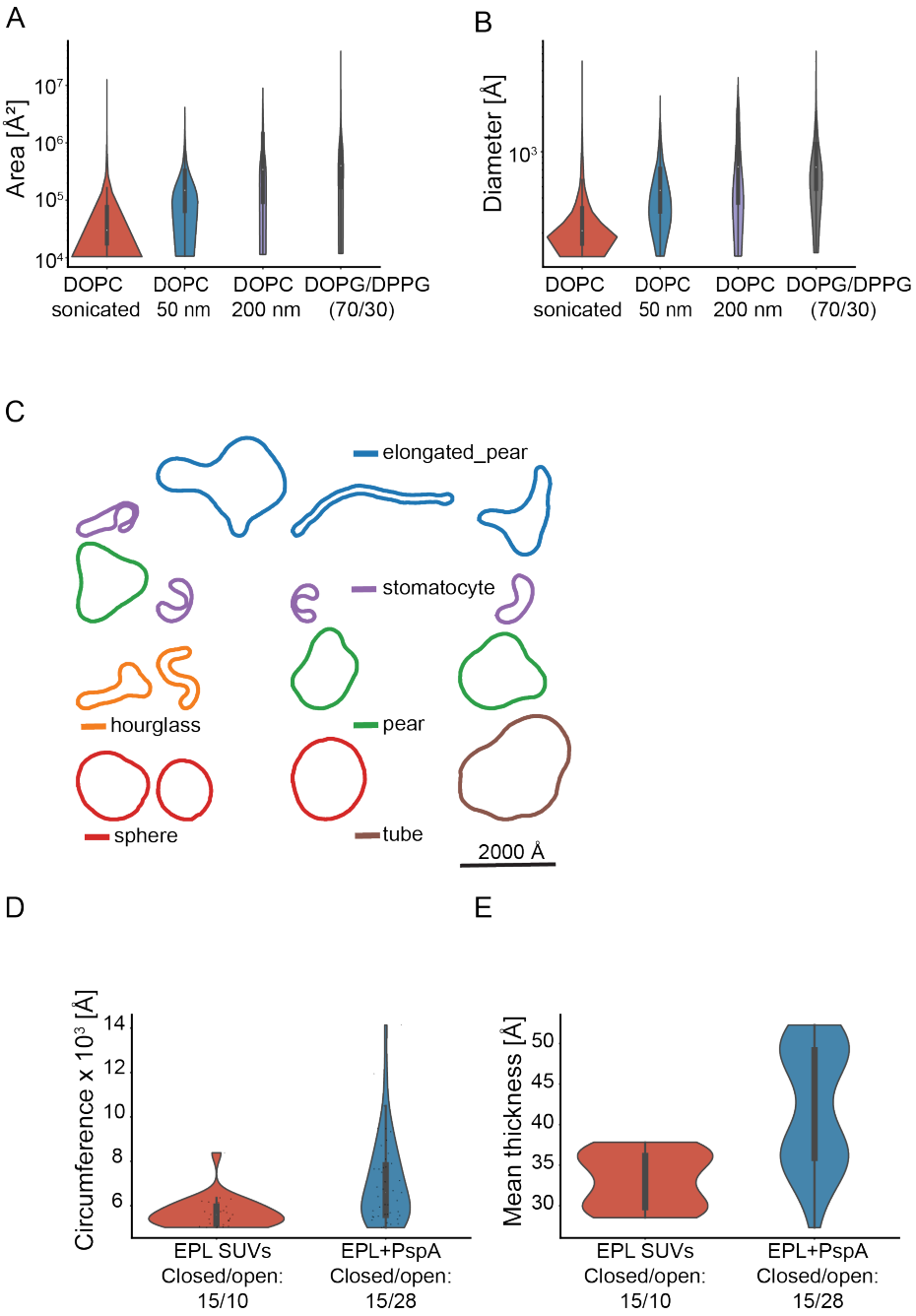

FIGURE 3.9: *(A, B) Violin plots of the evaluated vesicles from four data sets (DOPC sonicated, DOPC 50 nm size-filtered, DOPC 200 nm size-filtered, and DOPG/DPPG (70/30)) with area (A) and diameter (B). (C) A total of 15 irregular shapes that have similarly high confidence score derived from the shape classifiers as in Figure 6D but were excluded due to irregular shapes that are not closely resembling any of the pre-trained shapes. (D) Zoomed-in violin plot of the membrane length distribution of membranes with a length greater than 5000 Å of the EPL SUV and EPL + PspA data sets. (E) Zoomed-in violin plot of the mean thickness distribution of membranes with a length greater than 5000 Å of the EPL SUV and EPL + PspA datasets.

with one wider end tapering towards the distal end. Moreover, engulfed membranes were continuous lipid tubes as well as isolated small vesicles and membrane patches. In the absence of PspA, control SUVs had a narrow bilayer thickness distribution from 27 Å to 32 Å with a mean bilayer thickness of 31 Å (Figure 3.10c). After incubation with PspA, SUV membranes were significantly thicker on average, with a broad distribution and a major peak at 38 Å and a minor peak at 68 Å. In the presence of PspA and ATP, the bilayer thickness distribution closely resembles the PspA sample (mean thickness, 37 Å). The observed increase in bilayer thickness after incubation with PspA is consistent with a previous report (Junglas et al., 2021). To monitor changes in vesicle sizes, we used the vesicle perimeter as a descriptor (Figures 3.10, 3.11A). The EPL SUVs alone had a mean perimeter of 100 nm, corresponding to a mean diameter of 32 nm. Similar to the bilayer thickness, the distribution of vesicle perimeters was significantly increased in the presence of PspA and PspA + ATP, peaking at 160 nm and 150 nm, respectively. The vesicle size increase observed after incubation with PspA agrees with the previously reported PspA-mediated vesicle fusion (Junglas et al., 2021). Another prominent feature of the vesicles containing PspA was the formation of small, double-membrane vesicles (that is, small vesicles that are encapsulated by a larger vesicle), in analogous topology to intra-luminal vesicles (ILVs) (Figure 3.10b, red arrowheads). Approximately 9% of all vesicles were double-membrane vesicles in the control, whereas the share of double-membrane vesicles increased in the PspA preparations to 41% and was highest in the PspA + ATP sample at 52% (Figure 3.10e). Using the ATPase-deficient mutant PspA R44K/E126Q/E179Q as a negative control, we validated that indeed it was the ATPase activity of PspA and not the addition of ATP that gave rise to the increased number of double vesicles in the PspA + ATP sample. In addition, the distance between the two enclosed vesicle membranes, termed here the enclosure distance, was on average higher in the control vesicles (>70 Å) with a very broad enclosure distance distribution (Figure 3.11B, C). Both the PspA as well as the PspA + ATP sample showed a well-defined distance distribution with a mean enclosure

distance of 67 Å and 62 Å, respectively. Compared with the vesicle perimeter, only the smallest vesicles (perimeter of 100-200 nm) showed this constant enclosure distance of 50-70 Å (Figure 3.11D). Together, this quantitative image analysis of vesicle characteristics showed that the presence of ATP increases the occurrence of double-membrane vesicles through the enhanced membrane remodelling capabilities of PspA.

3.2.7 Lipid nanoparticles

Further testing the capabilities of CryoVIA was done by analysing micrographs of lipid nanoparticles (LNPs) encapsulating small interfering RNA (siRNA). These lipid nanoparticles are used in drug delivery research and their particle size and encapsulation efficiency are pivotal considerations when designing LNPs for *in vivo* use. Determining the size of nanoparticles in cryoEM micrographs is therefore a perfect use-case for CryoVIA.

Adjustments of CryoVIA for Lipid nanoparticles

These recorded lipid nanoparticles images did not show a visible lipid bilayer and the edge of these particles was not as clearly visible as in the previously shown datasets. The inner density of these particles though was higher than the surrounding environment leading to clearly visible particles with less sharp edges than previously analysed vesicles. Because the lipid nanoparticles were visually very different than previously seen vesicles a new neural network was trained on eight manually segmented micrographs. Additionally, a new option for neural network was implemented for cases were the elements of interest appear as blobs in the image rather than vesicles surrounded by a distinct lipid bilayer. Usually, only the membrane itself is being segmented and the skeleton of this segmentation is extracted and used for further analysis. For this specific case the whole vesicles was segmented and the contour of the vesicle was extracted and used for further analysis.

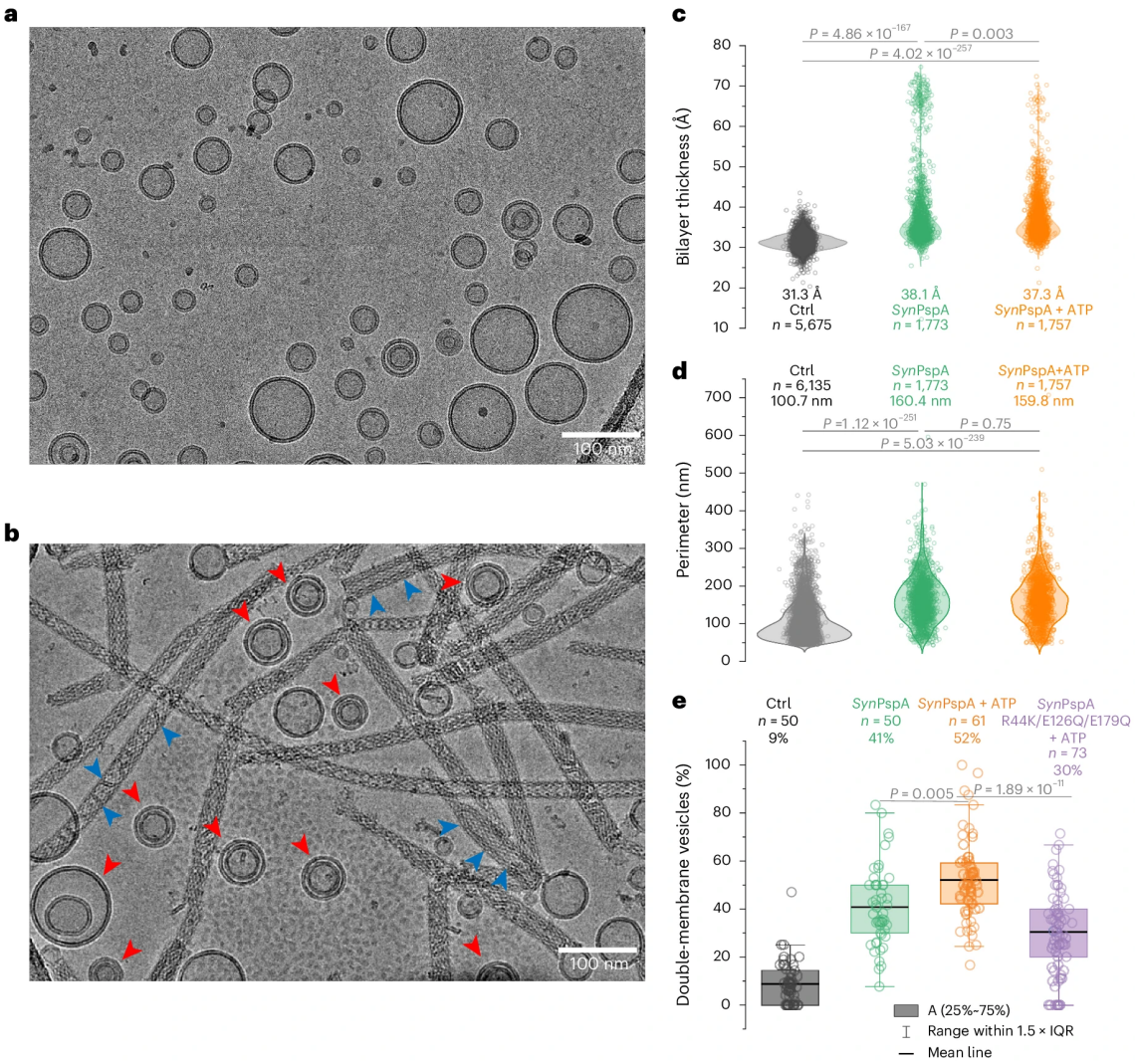

FIGURE 3.10: (A) Selected cryoEM micrograph from 632 recorded movies of EPL control vesicles. (B) Selected cryoEM micrograph from 50 recorded movies of the SynPspA + EPL sample. Red arrowheads indicate encapsulated vesicles. Blue arrowheads indicate engulfed membranes. (C) Violin plot of the bilayer thickness of control EPL SUVs (gray), SynPspA + EPL SUVs (green) and SynPspA + EPL + ATP SUVs (orange). The mean bilayer thickness, the number of measured vesicles (n) and P-values from a two-sample t-test are indicated on the graph. (D) Violin plot of the vesicle perimeter of control EPL SUVs (gray), SynPspA + EPL SUVs (green) and SynPspA + EPL + ATP SUVs (orange). The mean vesicle perimeter, the number of measured vesicles (n) and P-values from a two-sample t-test are indicated on the graph. (E) Box plot of the relative occurrence of double-membrane vesicles in each sample: control EPL SUVs (gray), SynPspA + EPL SUVs (green), SynPspA + EPL + ATP SUVs (orange) and SynPspA (R44K, E126Q, E179Q) + EPL + ATP SUVs (violet). The relative number of double-membrane vesicles, the number of measured vesicles (n) and P-values from a two-sample t-test are indicated on the graph (Ctrl versus SynPspA, $P = 1.83 \times 10^{-19}$; Ctrl versus SynPspA + ATP, $P = 1.13 \times 10^{-31}$; Ctrl versus SynPspA R44K/E126Q/E179Q + ATP, $P = 1.24 \times 10^{-14}$; SynPspA versus SynPspA + ATP, $P = 0.005$; SynPspA + ATP versus SynPspA R44K/E126Q/E179Q + ATP, $P = 1.89 \times 10^{-11}$). IQR, interquartile range.

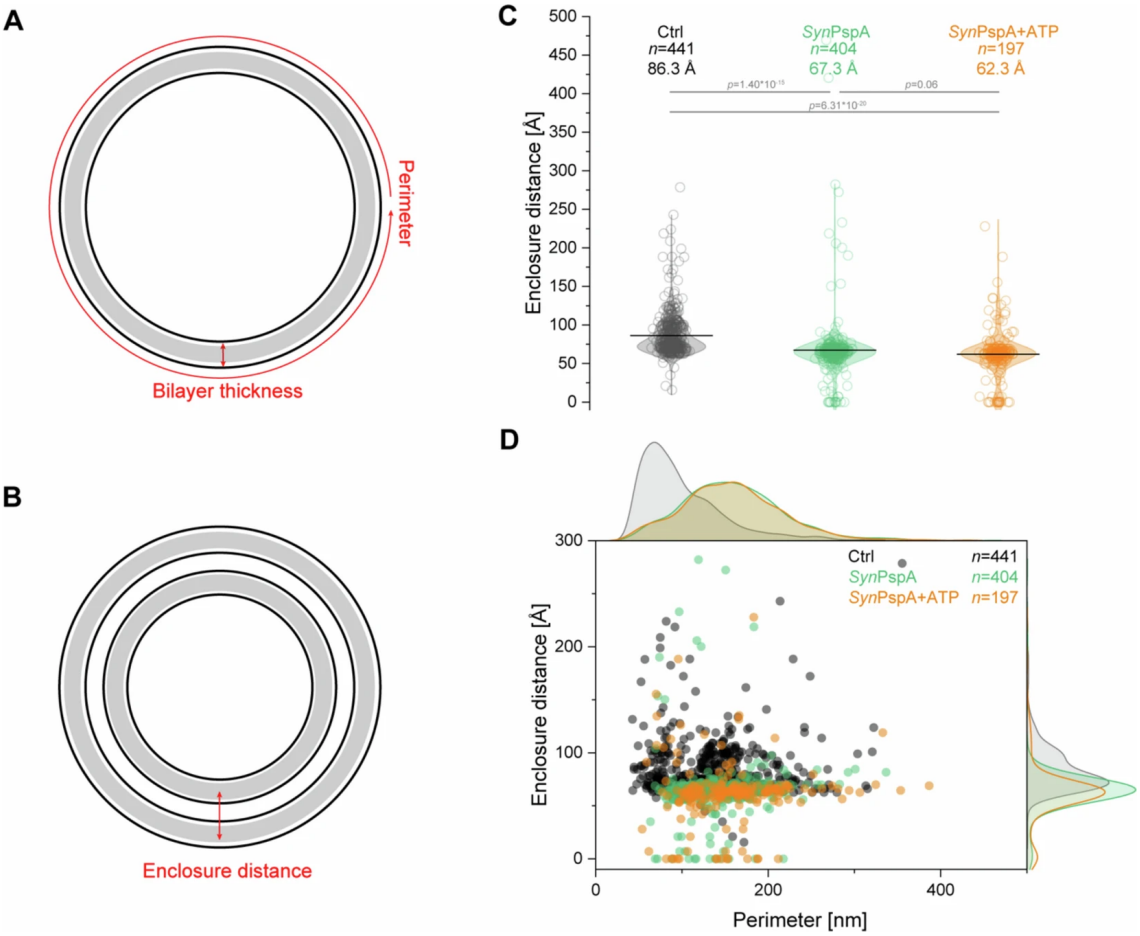

FIGURE 3.11: (A+B) Schematic view of the measured vesicle parameters: perimeter, bilayer thickness, and enclosure distance (see 3.4 for details). (C) Violin plot of the enclosure distance of control EPL SUVs (grey), SynPspA+EPL SUVs (green), and SynPspA+EPL + ATP SUVs (orange). The mean enclosure distance, and the number of measured vesicles n and p values from a two-sample t-test are indicated on the graph. (D) Scatter plot and histogram of the vesicle perimeter versus enclosure distance of control EPL SUVs (grey), SynPspA+EPL (green), and SynPspA+EPL + ATP (orange). The number of measured vesicles n is indicated on the graph.

Data analysis with CryoVIA

A total of 389 micrographs were used for this analysis. The micrographs were segmented by the specifically trained neural network, manually checked and incorrect segmentations of single vesicles were filtered out. To remove vesicles found outside of the grid holes the grid hole detection was applied and only vesicles inside the holes were kept. Figure 3.12A shows some of the segmentation results. While not all vesicles were segmented correctly a visual inspection revealed that most were correctly identified and statistical results can be confidently extracted. Figure 3.12B shows the distribution of vesicles found in each micrograph and Figure 3.12C shows the size distribution across all micrographs. Most of the found vesicles have a diameter in the range of ~550-800 Å and only a small fraction of vesicles can be found outside of this range. Additionally, the particles were spread out quite evenly across the grids resulting in most holes having 5-12 particles visible inside in holes after removing particles on the carbon edge and badly segmented particles. The actual number of particles per hole is probably slightly higher.

The previously reported diameter of 80 nm by Dynamic Light Scattering analysis was only partially confirmed. While particles with ~80 nm diameter were found in the micrographs, the nanoparticles appeared with a wider distribution of sizes and the most particles had a diameter of ~70 nm.

3.3 Discussion**

We introduced a dedicated Cryo Vesicle Image Analyser (CryoVIA) software package for the evaluation of membrane structures in cryoEM data sets. CryoVIA comprises the complete image analysis workflow from neural-network segmentation, membrane structure identification followed by the structure analysis (Figure 3.1).

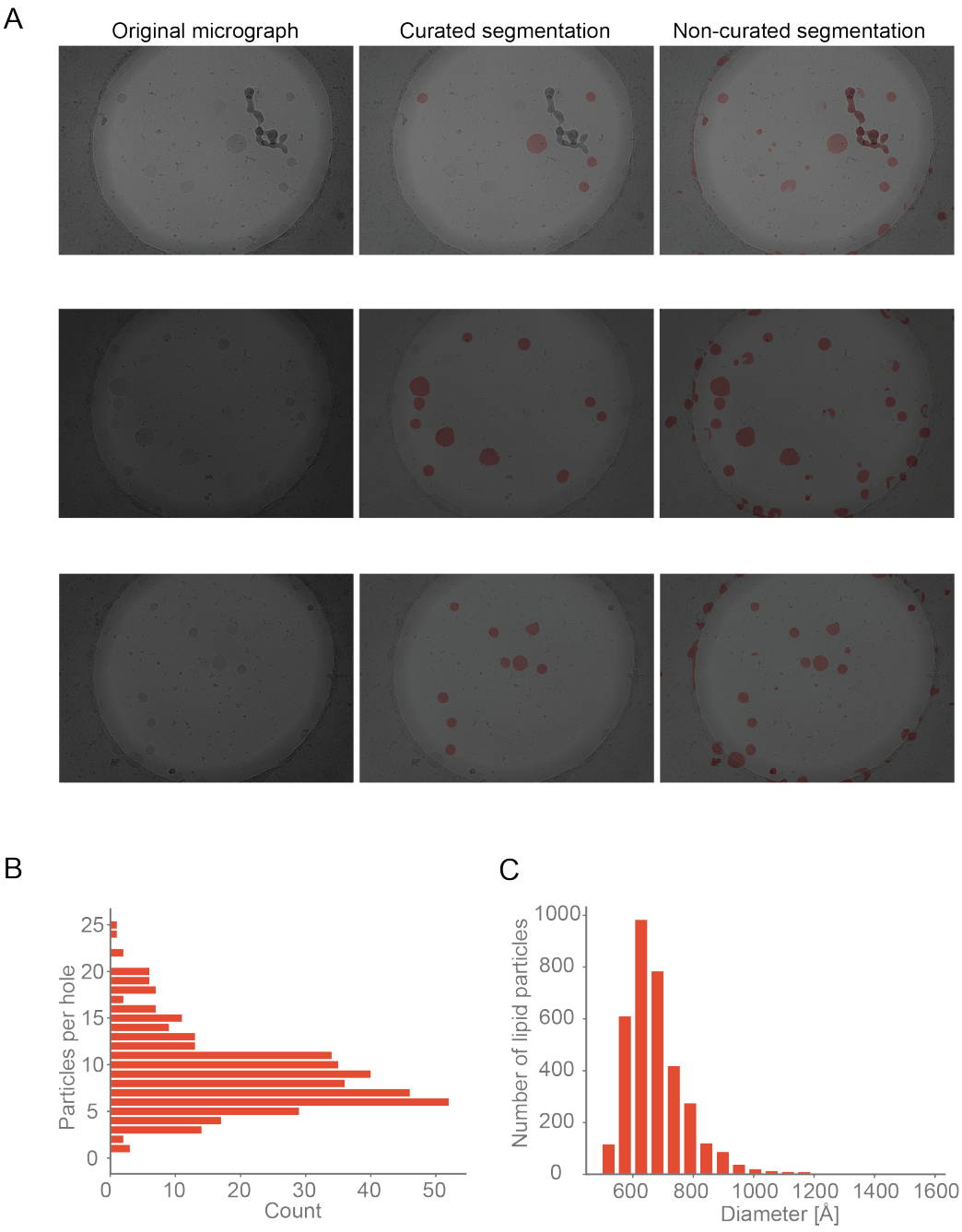

FIGURE 3.12: (A) Histogram showing the distribution of diameter in the lipid nanoparticle dataset. (B) Histogram showing the distribution of amount of particles visible per micrograph (C) Three example micrographs with their segmentation before and after clean-up.

When complete membrane structures are identified, they are subjected to the analysis of local and global structural parameters such as membrane thickness and curvature with high precision as well as diameter, circumference, and area followed by classification into distinct membrane shapes (Figures 3.2, 3.3, 3.4). CryoVIA was tested on the analysis of four different vesicle data sets confirming relevant differences induced by the preparation procedure and membrane composition (see Table 3.1, 3.3, Figures 3.5, 3.6). Moreover, CryoVIA was applied to quantitatively evaluate membrane shape changes of a previously reported bacterial ESCRT-III membrane remodelling protein PspA (see Table 3.2, Figure 3.8). As an additional use-case CryoVIA was applied to measure the size of lipid nanoparticles prepared for cryoEM methods as well as analyse the amount of lipid nanoparticles present per hole in the grid mesh.

The here obtained membrane thicknesses were determined directly from the cryoEM images with an estimated spatial precision of ± 0.2 Å. When image intensities are used for thickness estimation, they interestingly correspond to the lipid hydrophobic thickness (2DC)(Heberle et al., 2020). This thickness is given by the distance covering the lipid chains embedded present in the bilayer and is slightly lower than the expected distance between the denser phosphate head groups (DHH) that are commonly obtained by X-ray or neutron scattering methods. For instance, in the case of DOPC (50 nm size filtered) the 2DC and DHH were determined by small-angle X-ray scattering at 29.3 and 35.0 Å, respectively. The same study reported cryoEM based measured bilayer thickness of DOPC lipids (50 nm size filtered): mean thickness value of 29.7 ± 0.6 Å matching the hydrophobic thickness (2DC) (Heberle et al., 2020). The here estimated bilayer thickness of the DOPC 50 nm size-filtered test dataset at 29.0 Å compares well with the reported cryoEM value of 29.7 Å. The slight differences are likely explained by different pixel size calibrations. Reasons for the deviation to the actual phosphate head group distance DHH arise from the smearing of the obtained lipid intensities due to the 2D projection through a spherical 3D lipid membrane convolved with the CTF. For DOPG and

DPPG, the lipid hydrophobic thicknesses 2DC were reported to be 27.2 Å and 26.8 Å, respectively, albeit at elevated temperatures of 50°C (Pan et al., 2012). For the mean bilayer thickness of DOPG/DPPG using the CryoVIA method, we obtained 27.2 Å that is in close correspondence to the previously reported values. Together, we find the CryoVIA estimates on membrane thickness very precise on sub-Å-scale and accurate on an Å level as they are in good agreement with previously reported values by scattering methods. Regardless of minor deviations, CryoVIA can be used to reliably estimate membrane thickness in particular for comparative studies that investigate membrane thickness changes.

CryoVIA was also able to analyse micrographs of LNPs showing a deviation of the previously measured LNP size. While not designed for elements which are not membrane and vessel-like, the basic analyses of CryoVIA can still be used for any identifiable object in images when the size, shape, curvature or distance to other object is of interest. The only membrane specific part of CryoVIA is the lipid bilayer estimation and the pre-trained neural network.

Imaging of vesicular lipid structures using cryoEM has been a direct way to visualize and characterize the structures at high resolution. In some contexts, negative staining electron microscopy has been used. However, as the technique requires specimen drying followed by a collapse of the lipid structures, the detailed structural properties are not faithfully maintained for imaging. In contrast, the main advantage of cryoEM is the structural preservation of the specimen in a fully hydrated manner after plunge-freezing them to embed them in vitreous ice. However, it should be mentioned that during the freezing procedure, the volume of the starting droplet is reduced drastically into water films of 40 - 80 nm of thickness imposing stress and crowding of the large lipid structures. This preparation procedure excludes lipid structures from the analysis that are larger than the dimensions of the ice film thickness such as giant unilamellar vesicles. Nevertheless, although the observed lipid structures of appropriate sizes may suffer from some deformation, the cryoEM method presents a direct and faithful way of imaging lipid structures

in aqueous solution.

The presented CryoVIA was developed and tested using cryoEM micrographs of purified lipid-water mixtures. In this case, the structural analyses are restricted to the images in two dimensions. The analysed micrographs were recorded with a dose of 20 - 30 e^{-}/Å2 at an underfocus range between 2.0 - 3.0 µm. Previous analyses revealed that defocus series did not have an effect on the estimated bilayer thickness measurements while images close to focus suffered from poor overall contrast problematic for image analysis (Heberle et al., 2023). The precision and easy accessibility to quantifications of lipid shape changes opens up new possibilities to study membrane-remodelling proteins (Junglas et al., 2021, Low et al., 2009, Zhang and Hinshaw, 2001) such as dynamin and ESCRT-III proteins.

Vesicle identification in cryo-micrographs can also be used to aid in solving the structure of membrane proteins using single particle structure determination (Coupland et al., 2024). Although not implemented, CryoVIA applications could also be extended to inform particle picking for single-particle structure determination of bilayer-embedded protein complexes, e.g., by selecting protein complexes that reside in vesicles of particular diameter ranges and lipid curvatures in analogy to the previously published tool Vesicle Picker (Karimi, Coupland, and Rubinstein, 2024). Various methods for solving structures of membrane-bound proteins in liposomes have been proposed (Wang and Sigworth, 2009). This way, proteins can be directly isolated in cell-derived membrane vesicles (Tao, Zhao, and MacKinnon, 2023) and exposed to additional stimuli, e.g., electric fields (Mandala and MacKinnon, 2022) and buffer gradients (Sejwal et al., 2017, Yao, Fan, and Yan, 2020). Although CryoVIA was not designed for single particle protein structure determination, it could be used to enhance the homogeneity of the structure by classifying picked particles through membrane curvature or vesicle shapes. Nevertheless, the current implementation of CryoVIA focuses on analysing the membrane and vesicle structures themselves rather than solving the structure of membrane proteins. Lipid membrane analysis tools in three dimensions have been developed for

electron tomography (Barad et al., 2023, Salfer et al., 2020). We here show that many of the conclusions on ultrastructural lipid changes can already be observed in two-dimensional images at better signal-to-noise ratios without the need of tilt-series acquisition and tomographic reconstructions. Moreover, the application of zero-tilt imaging has already successfully been extended to the in situ cellular environment (Lucas et al., 2022) and, therefore, the analysis of lipid structures from cellular images based on two-dimensional micrographs are expected to be possible. The results of the quantitative lipid structure analysis will largely depend on the initial results of segmentation, and, therefore alternative and more tailored membrane segmentation approaches (Martinez-Sanchez et al., 2014, Lamm et al., 2022) could be combined with the analytical tools from CryoVIA. CryoVIA's ability to process multiple data sets efficiently streamlines the analysis process. This feature is particularly advantageous when dealing with large-scale comparative studies including high-throughput experiments.

CryoVIA is a python-based program that is designed to run quickly on a desktop computer to run the analysis in a user-friendly manner, i.e., a data set of 2031 micrographs can be fully analysed within four hours of runtime on a dedicated work station (see 3.4). One of the key advantages of our toolkit is the ability to accurately measure key membrane parameters such as bilayer thickness, diameter, and shape of vesicles. This level of precision is critical for understanding the structural and molecular variations of biological membranes of vesicles and organelles. The toolkit's user-friendly interface and algorithms ensure that researchers, regardless of their expertise, can access and utilize these analytical tools. The presented toolkit offers a robust and accessible solution for the analysis of membranes in cryoEM micrographs opening up new avenues to study protein lipid interactions. Moreover, the software can also be employed to address experimental challenges in adjacent fields of structural biology such as nanoparticles used in drug delivery as well as soft-matter science.

3.4 Materials and Methods

3.4.1 Liposome preparation*

This small section on the liposome preparation was written by Dr. Benedikt Junglas who also prepared the liposomes. I have his permission to use the section in this thesis. Chloroform dissolved 1,2-dioleoyl-sn-glycero-3-phosphocholine (DOPC), 1,2-dioleoyl-sn-glycero-3-phospho-(1'-rac-glycerol) (DOPG) and 1,2-dipalmitoyl-sn-glycero-3-phospho-(1'-rac-glycerol) (DPPG) were purchased from Avanti polar lipids. Lipid films were produced by mixing the lipid solutions (100% DOPC or 70% DOPG/30 % DPPG (w/w) mixture) and evaporating the solvent under a gentle stream of nitrogen and vacuum desiccation overnight. The lipid films were rehydrated in 10 mM Na-Phosphate buffer pH 7.6 (DOPC) or 10 mM Tris-HCl pH 8.0 (DOPG/DPPG) by shaking for 30 mins at 37 °C (DOPC) or 50 °C (DOPG/DPPG). The resulting liposome solution was subjected to five freeze-thaw cycles. The liposome solution was either used as is (DOPG/DPPG), or SUVs (small unilamellar vesicles) were generated by extrusion of the liposome solution through a porous polycarbonate filter (50 nm pores, 200 nm pores) or tip (40% power output, 50% duty cycle, 5 min) using an Ultrasonic Homogenizer (Biologics, Inc.).

3.4.2 Electron cryo-microscopy*

This small section on the image acquisition was written by Dr. Benedikt Junglas who also imaged the liposomes. I have his permission to use the section in this thesis. Liposome grids were prepared by applying 4 µl sample (for sample details see Table 3.1) to glow-discharged (PELCO easiGlow Glow Discharger, Ted Pella Inc.) Quantifoil grids (R1.2/1.3 Cu 200 mesh, Electron Microscopy Sciences). The grids were plunge-frozen in liquid ethane using a Leica EM GP2 set to 80% humidity at 10 °C (sensor aided backside blotting, blotting time 3 - 5 s). Movies were recorded in underfocus on a 200 kV Talos Arctica G2 (ThermoFisher Scientific) or a 300 kV

Titan Krios G4 (ThermoFisher Scientific) electron microscope equipped with a Bioquantum K3 (Gatan) or Biocontinuum K3 (Gatan) detector operated by EPU (ThermoFisher Scientific). Movie frames were gain corrected, dose weighted, aligned, binned to the physical pixel size and the CTF of the micrographs was estimated using cryoSPARC Live (Punjani et al., 2017). Micrographs with poor ice or poor CTF fit were removed.

3.4.3 LNP preparation

This small section on the lipid nanoparticle preparation was written by Jeffrey Momoh who also prepared the particles. I have his permission to use the section in this thesis.
Lipid nanoparticles (LNPs) encapsulating siRNA targeting NEMO/IKK-γ (Integrated DNA Technologies, Coralville, IA, USA) mRNA were formulated under RNase-free conditions using RNase-free materials. Briefly, siRNA was dissolved in sodium acetate buffer (pH 4.0) and mixed with a lipid solution in ethanol at an N/P ratio of 3. The lipid mixture consisted of D-Lin-MC3-DMA (MedChemExpress, Monmouth Junction, NJ, USA), DSPC, cholesterol, and PEG-DMG (Avanti Lipids, Alabaster, AL, USA) at a molar ratio of 50:10:38.5:1.5. The resulting LNP suspension was dialysed overnight against Dulbecco's PBS (pH 7.4) in a 1,000-fold volume excess. Encapsulation efficiency and siRNA concentration were assessed using the Quant-IT RiboGreen RNA Assay Kit (Thermo Scientific, Waltham, MA, USA), comparing fluorescence signals in LNP samples with and without the addition of Triton X-100. Cholesterol content was measured using the Cholesterol FS Assay Kit (DiaSys Diagnostic Systems, Holzheim, Germany). Dynamic light scattering (DLS) was performed to determine the hydrodynamic particle size and polydispersity index. For cryo-electron microscopy, LNPs were diluted to a final lipid concentration of 8 mg/mL.

LNP samples were prepared on Quantifoil grids with a continuous 2nm carbon support film. A VitroJet (Cryosol-world BV, Weert, the Netherlands) was used to

	DOPC sonicated	DOPC 50 nm site-filtered	DOPC 200 nm size filteres	DOPG/DPPG (70/30)
Lipid Concentration (mg/ml)	5	5	5	5
Magification (x10,000)	49	49	49	53
Pixel size (Å/pix)	1.737	1.737	1.737	1.737
# Frames	45	45	45	45
Total Dose ($e^-/Å^2$)	45	45	45	45
Underfocus µm	2.0	2.0	2.0	2.0
# Movies	909	251	356	514
# Vesicles detected	38,871	6,061	1,819	2,179
Vesicle frequency per micrograph	42.8	24.1	5.1	4.2

TABLE 3.3: Liposome data acquisition

process the grids using 30s of plasma-cleaning and deposited at speeds ranging from 2 to 5 mm/s. Subsequently, imaging was carried out at a pixel size of 2.79 Å, with a nominal electron dose of approximately 80 electrons per square Ångström, within a defocus range of -5 to -20 micrometers. This imaging was accomplished using a 200 kV Talos Arctica equipped with a K3 BioQuantum energy filter.

3.4.4 Graphical User Interface*

CryoVIA is implemented in python and is available as a graphical user interface (GUI) for ease of use. The GUI is split into four sections:

- Segmentation training (Figure 3.13A)

  In the first section, the user can create, copy or delete specific neural networks models. The default model is trained on the data sets we analysed but additional models can be created by training a completely blank model or copying and fine-tuning existing models. Depending on the variance in different data sets, it is helpful to use different models for different data sets. The segmentation section also provides a method to manually annotate training data by opening a plugin in napari (Ahlers et al., 2023).

- Shape classifier training (Figure 3.13B)

  The second section can be used to create new shape classifier models. The user can add and remove specific shapes from models and create new shapes by drawing in the provided window.

- Edge detection (Figure 3.14A)

  The third section can be used to detect and exclude grid holes in micrographs. This detection can be directly applied to already created data sets or the correct parameters can be identified and applied during the data set analysis. When detection is applied to data sets, membranes found outside of the grid holes will be removed from the data sets. This task is also available as a standalone software and can be applied to particle picking jobs of Relion (Scheres, 2012) or CryoSparc (Punjani et al., 2017).

- Membrane analysis (Figure 3.14B)

  The last section is the main part of the GUI and can be used to create new data sets, run segmentation and analysis on data sets and to inspect and clean data sets. The inspection offers various filters and possibilities to inspect single membranes found in the data sets. It is also possible to compare the results of different data sets and export various results as csv-files.

3.4.5 Segmentation

To analyse membranes cryoEM micrographs the membrane structure of interest have to first be located and preprocessed. Identifying pixels belonging to membranes and background pixels is a classic semantic segmentation task and is performed by a convolutional neural network. Two very different CNN architectures were considered, implemented and compared. The first architecture is the U-Net, the standard CNN for segmentation of biomedical images. The second option is a version of a lesser known architecture called the region growing CNN (RGCnet).

A

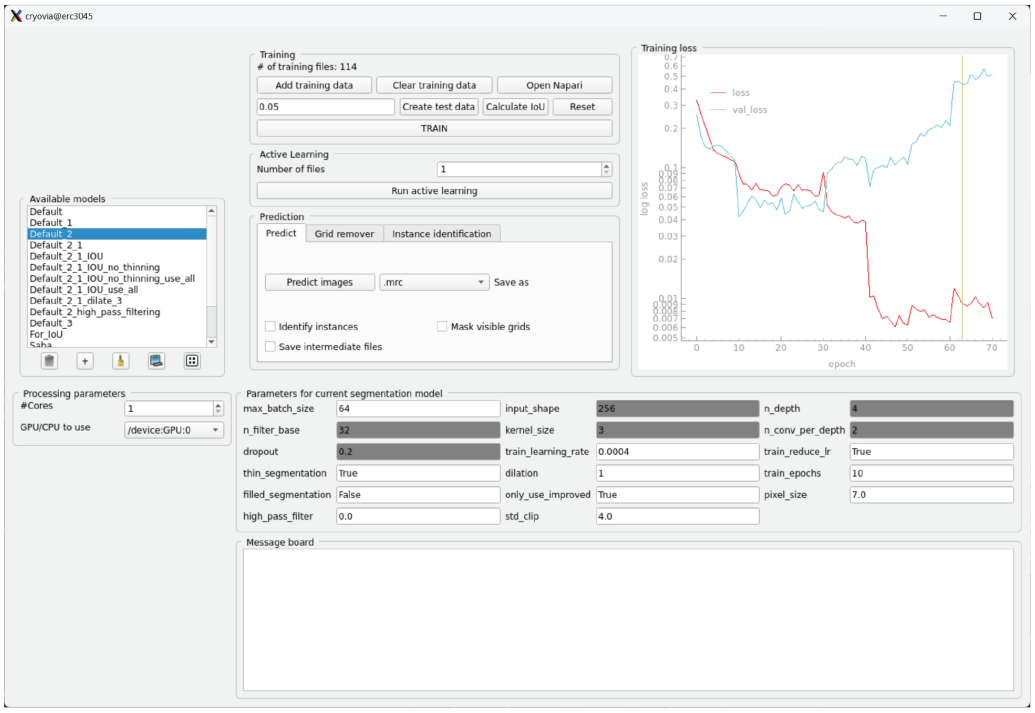

B

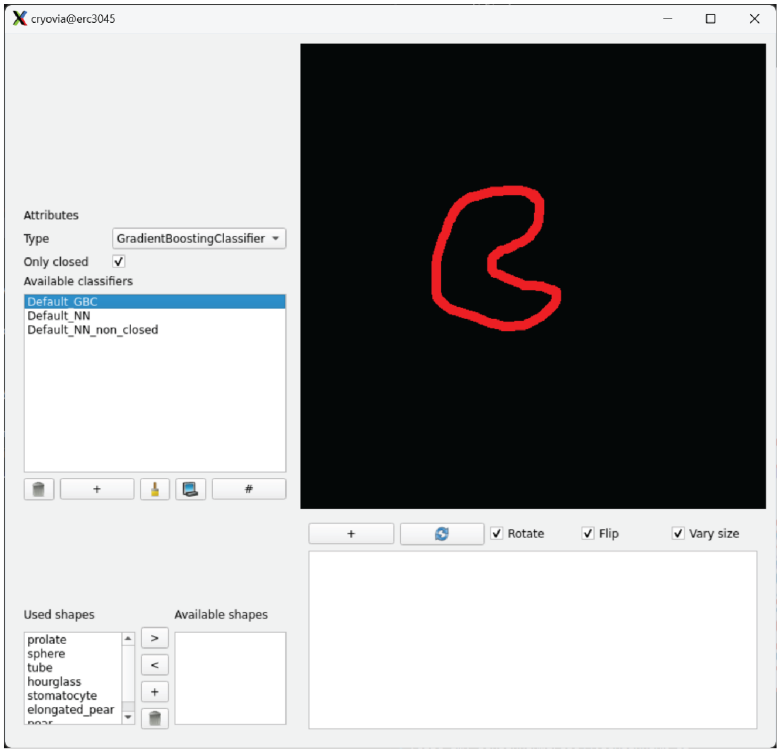

FIGURE 3.13: (A) Segmentation neural network training and modifier including parameters for segmentation model. (B) Display of results of shape classifier and modifier.

A

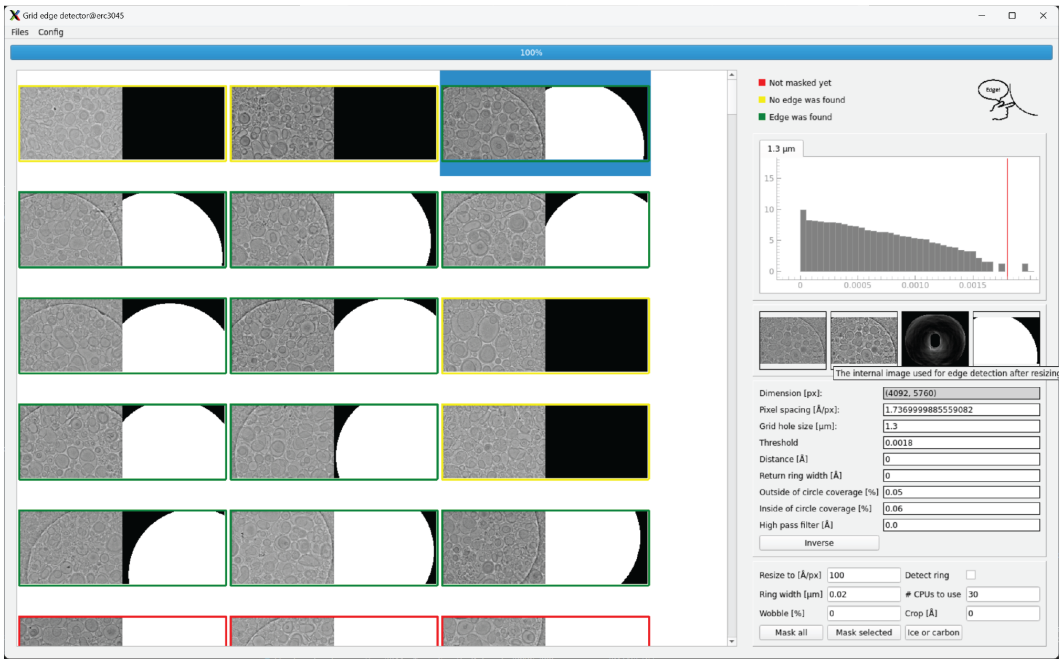

B

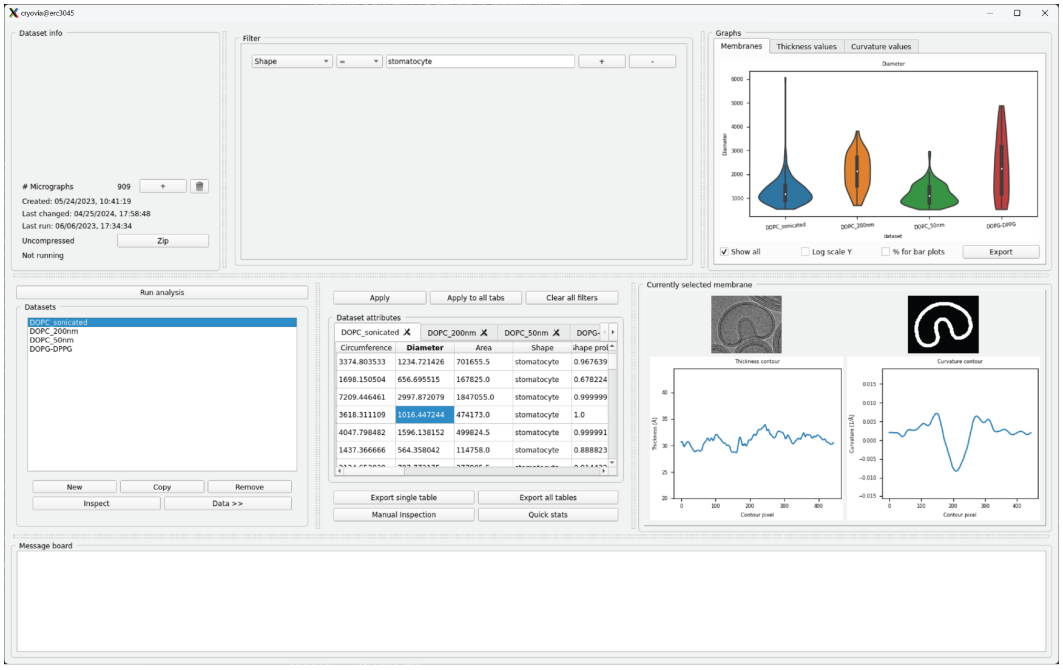

FIGURE 3.14: (A) Foil hole edge detector. (B) Data analysis and data set creation/running.

U-Net

The U-Net is a specific type of CNN invented in 2015 and a standard network architecture in image recognition (Ronneberger, Fischer, and Brox, 2015). The name is based on the the architecture structure of the network which consists of a contracting path and a symmetrical expanding path on either side. The contracting path is following the standard architecture of a CNN. , iterative applications of convolution layers with a 3x3 kernel are performed, each connected to a rectified linear unit (ReLU). Inbetween are max pooling layers for downsampling after which the number of feature channels is doubled. The expanding path mirrors the contracting path by upconvolutions. Additionally after each upsampling step the corresponding feature map of the contracting path is concatenated adding to the spatial awareness of the network. The default U-Net implemented for CryoVIA uses an image patch of 256x256 pixels as input, has a depth of 4 with 32 filters in the first layer, a consistent kernel size of 3x3 for each convolution layer and 2 convolution layers per depth.

RGCnet

RGCnet is an architecture designed for vessel like objects of interest (Lagergren, Rutter, and Flores, 2020). Rather than producing a segmentation map of the same size as the input it predicts only the segmentation map of the eight pixels surrounding the central pixel of the input. The architecture of RCGnet is a multilayer convolutional ResNet-style with dropout layers between residual blocks. The last convolution is followed by a fully connected layer of shape 9x1 representing the central 9 pixels. It is trained with pixel-wise binary cross entropy loss and the Adam optimizer (Kingma and Ba, 2014). The input maps are cropped 160x160 pixel images from the micrographs resized to a pixel size of 7 Å per pixel. The idea is to start segmentation with a pixel seed coordinates, predict the surrounding pixels and use the surrounding pixels which were identified as membrane pixels for

the next round as seed pixels. This technique ensures connectivity of the segmentation and because membranes are vessel like structure it should work well with the given input.

To test the architecture we trained a network an the same segmented data as the U-Net, extracting 50000 random cropped images with half of them on or near the membranes and the other half with only background pixels as the central nine pixels. The resulting segmentation is comparable to the result of the U-Net segmentation (Figure 3.15). However, for this technique seed pixels from the previously manually segmented membranes were used as starting points which can not be done with unseen data. Using randomly selected coordinates can be used as was done in the original work (Lagergren, Rutter, and Flores, 2020) but this has several drawbacks when it comes to images of membranes. The visible membranes in the micrographs are multiple different objects and not just one completely connected membrane or vessel like the eye vessels presented in the original work. This means we would have to randomly sample a high number of pixels from the data to minimize the possibility to miss some of the membranes. We also cannot stop sampling data when we found one positive segmentation result because the would only yield one segmented membrane. Furthermore, the amount of iterative predictions of cropped images is very high due to every run only resulting in a segmentation of eight new pixels.

In CryoVIA only the U-Net is implemented. While the RCGnet segmentation has a similar accuracy to the U-Net segmentation, U-Net is easier to use, faster and does not rely on random seed pixels to get a good segmentation. Even if the segmentation result would be slightly improved, CryoVIA does not rely on perfect segmentation as only the skeleton as a representation of each membrane is used and ultimately this skeleton is improved by various post segmentation processes.

The pre-trained U-Net provided by CryoVIA segments in patches of 256 x 256 pixels and has a depth of 4, 32 filters in the first layer, a kernel size of 3, 2 convolution layers per depth and a training rate of $4 * 10^{-4}$. A total of 92 images were manually

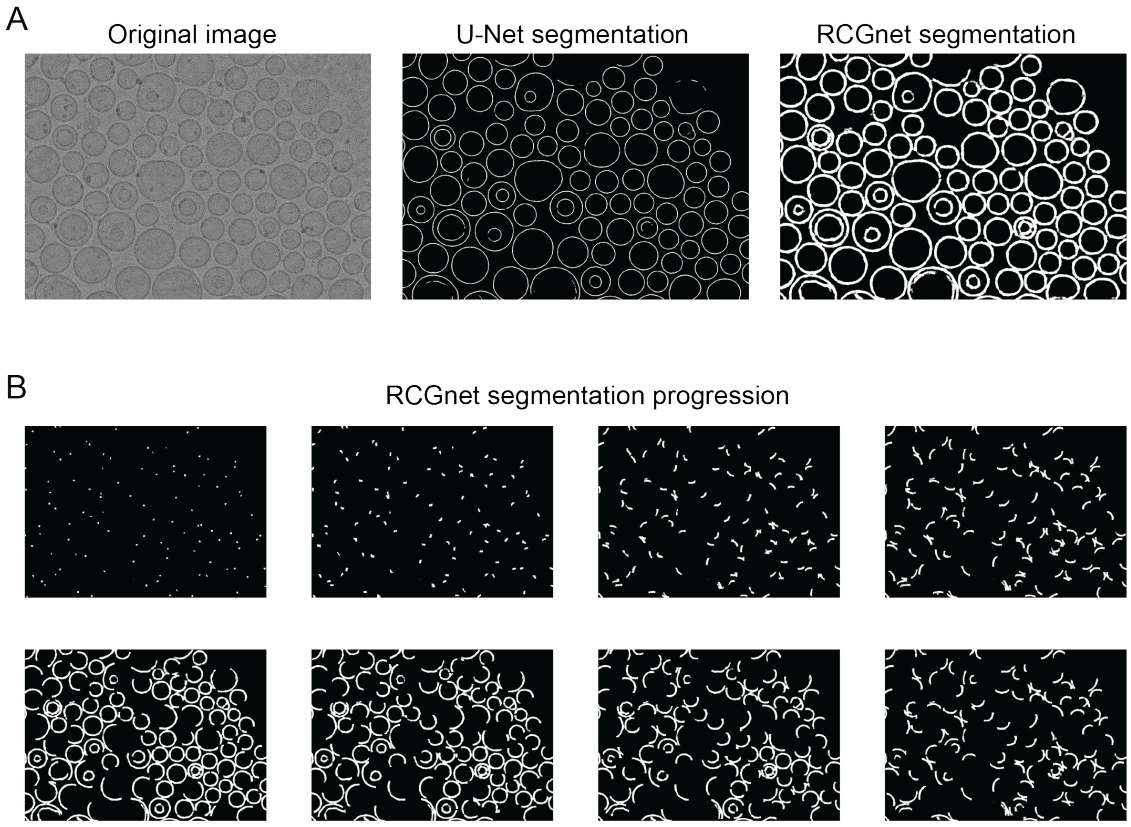

FIGURE 3.15: Comparison of the segmentation result from a trained U-Net and a trained RGCnet. (A) Left: An example micrograph for segmentation. Middle: Segmentation result of a trained U-Net. Right: Segmentation result of a trained RGCnet. (B) Progression of the RGCnet segmentation over multiple iterations. The growing vesicle segmentation with each iteration can be clearly seen.

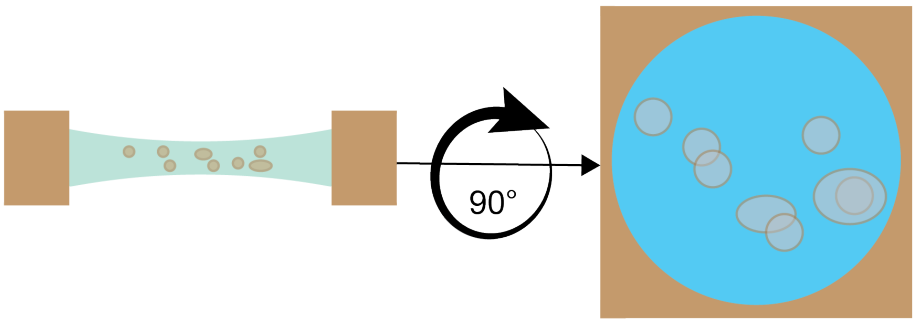

FIGURE 3.16: Illustration of how micrograph can show seemingly overlapping vesicles. If vesicles are embedded at different heights in the ice they appear to be overlapping in the recorded micrographs.

segmented and used as training data with a pixel size of 7 Å/pixel.

Because some of the vesicle seen in our data were seemingly overlapping due to being on different z-heights in the ice (Figure 3.16) and because semantic segmentation cannot solve this issue easily an instance segmentation method was also shortly tested. Mask region based CNN is an instance segmentation architecture which finds instances by bounding boxes and afterwards performs pixel-wise segmentation of the boxes (He et al., 2017). Because it segments each box separately a pixel in the original image can have multiple classes and overlapping instances can be solved. However, because Mask-RCNn needs a very large dataset to train on and membranes come in a large variance of sizes, training the Mask-RCNN did not result in any usable segmentation. To solve the overlapping membranes in the micrograph a different method was developed using the semantic segmentation of the U-Net, skeletonization as graph representation (Yan, 2021) as well as curvature estimation.

3.4.6 Post segmentation processing**

Solving overlapping membrane structures*

As part of post segmentation processing, the segmented tracks need to be pruned in particular to disentangle overlapping membrane structures. For this step, the connected components of the segmentation were extracted and for each component the skeleton was calculated (Figure 3.17A). Subsequently, the skeleton was converted to a graph network (Yan, 2021). In this graph network nodes are represented by the crossovers of membrane skeletons and edges are represented by the membrane skeleton segments connected to crossover nodes (Figure 3.17B/C). Each node was then evaluated to connect membrane segments that may be part of the same membrane by calculating the angle between the different segments connected to this node. When this angle was larger than 125°, the segments were not combined whereas when two segments formed a straight line, the skeletons were merged into one continuous membrane structure. The segment combination that did not form a straight line but had an angle smaller than 125° was evaluated by the curvature and the corresponding center of the fitted circles (Figure 3.17D/E). The curvature was calculated by extracting a few skeleton pixels of each membrane edge close to the node and fitting circles to these few pixels (Figure 3.21). When curvature values and fitted circle centers are similar the segments are combined. The output of this method is a binary segmentation mask for each individual membrane (Figure 3.17F). With this approach, overlapping membrane segments can be assigned to continuous underlying membrane stretches.

Improving membrane skeleton*

For subsequent parameter determination, the refinement of the membrane bilayer center is critical as the segmentation procedure inconsistently detected inner and outer leaflet separately. In order to remove those ambiguities, we convolved the micrograph with a bilayer-like kernel consisting of a concentric ring where the outer

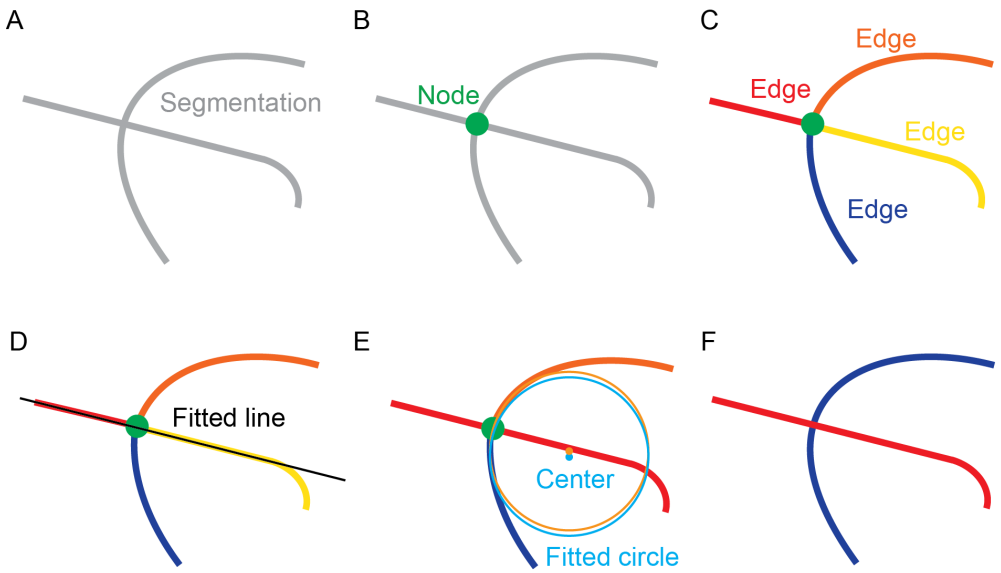

FIGURE 3.17: (A) Example binary segmentation. (B) Identified node where vesicles overlap. (C) Four edges connected to the node. (D) Fitted a straight line through the red and yellow ends. (E) Combined red and yellow ends because the straight line fitted well close to the node resulting in two overlapping ends. Fitted circle for the orange and blue end close to the node and the center of the fitted circle. (F) Combined blue and orange edges to one membrane stretch as fitted circle centers were close to each other.

radius represents half the maximum bilayer thickness and the inner radius was chosen such that the distance between the outer and inner radius corresponded to the leaflet thickness. As a result of this convolution, the bilayer membrane signal was enhanced and presented by a single line that was boosted by the application of the Frangi filter, which had been developed to enhance vessel-like structures (Frangi et al., 1998). Lastly, the detected lines were further simplified using interpolation through selected points of highest pixel intensities of the filtered image. When this method of detecting the bilayer center failed due to weak signal, the segmented membranes were labelled unsuitable for more detailed membrane bilayer thickness analysis.

Grid edge detection

Biological samples for cryoEM are transferred to a sample grid. These round disks are usually made out of copper or gold (Jensen, 2010) and consist of an outer ring and an inner mesh grid. A thin carbon film is applied to the metal mesh, serving as a support for the sample. When using Quantifoil grids, in each grid square are symmetrically ordered round holes perforating the carbon, usually with a diameter of 1.2 or 2 µm. During sample preparation the grid is covered with the sample, blotted and subsequently frozen. This way the holes are filled with the sample embedded in a thin layer of vitreous ice.

During image acquisition multiple images can be acquired per hole but sometimes parts of the carbon film are visible. Ideally, no sample should be present on the carbon film but this is rarely the case. Various different methods can be used to grid holes in the carbon film (Cheng et al., 2023,Berndsen et al., 2017). These methods rely on the idea that the edge of the holes have more detectable textural features than the vitreous ice and particles within. Using this fact one can use a combination of various filters and thresholding operations to detect the edge of the hole and subsequently fit a circle to the edge. This method works well if the edge of the hole is the only darker edge present in the micrograph but when other

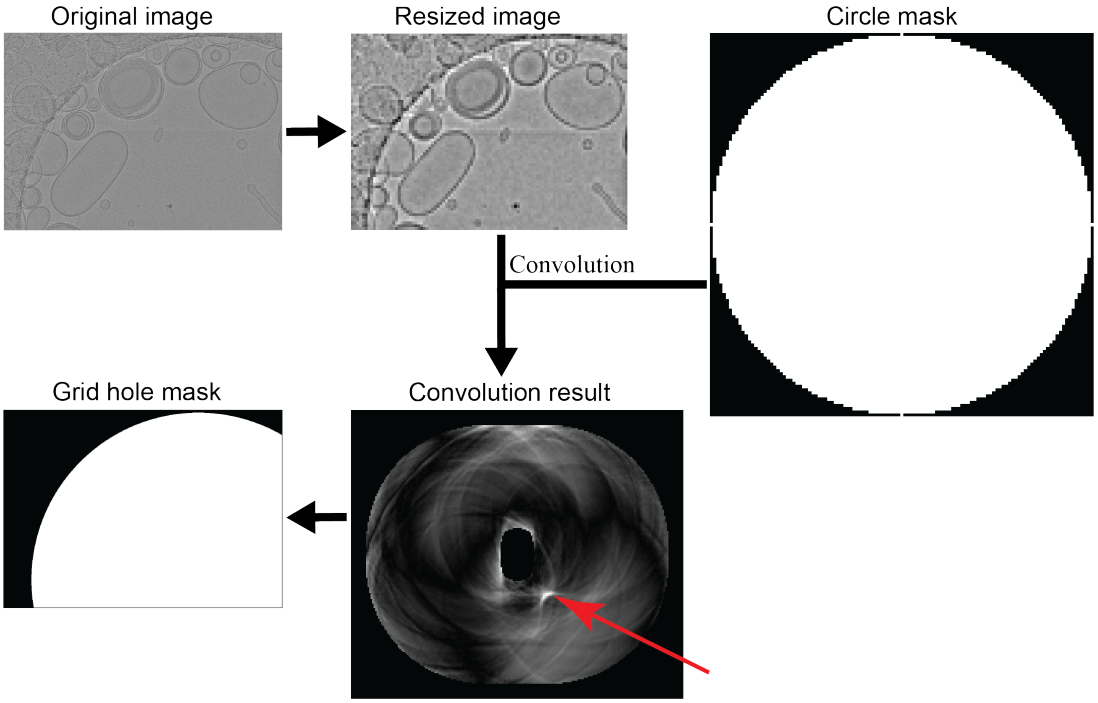

FIGURE 3.18: Illustration of the grid hole detection method. The analysed micrograph (top left) is resized to a much smaller size (top middle). A mask of a circle with the corresponding diameter of 1.2 or 2 µm is created (top right). For every pixel in the resized image the mask is applied and the difference between the mean of values inside and the mean of the values outside of the circle is calculated by various convolutions and displayed as an image (bottom right). The pixel with the highest value (red arrow) indicates the most likely center of a visible grid hole in the micrograph and a fitting mask in created (bottom left).

similarly shaped object like large vesicles are present in the micrograph it can fail to correctly identify the edge. For CryoVIA a new method is implemented which is less influenced by dark artefacts in the micrograph. First, the micrograph is resized to a predefined pixel size which by default is 100 Å. Then a mask of a circle is created with a diameter of 1.2 or 2 µm scaled to the predefined pixel size with a value of one for all pixels inside of the circle and zero for the rest. The rescaled micrograph is then padded with zeros by the radius of the circle on each side. Another image is also created with the same size as the padded, resized micrograph. The values in this image are zero where padding was added, otherwise it is one. The next step is a convolution of the resized micrograph and this circular mask, as well as a convolution of the other created image with the same circular mask. The convolution of the padded micrograph is the sum of all values inside the a circle with the size of the grid hole with each pixel representing the center of the circle. The second convolution is the number of values used for the sum of the first convolution. Using these two convolutions, the sum over all values in the resized micrograph and the number pixels in the resized micrograph it is now possible to calculate the mean values of all pixels inside and outside the circle for every circle center. The output of the method is the difference between the mean inside and outside values.

If the grid edge is visible in the micrograph, the inside of the grid hole is usually brighter than the outside. The highest value of the output should therefore be at the correct center of the grid hole and a mask can be created according to the hole size and the estimated center (Figure 3.18). If a brightness gradient is present in the micrograph the method will fail if the gradient is too strong. This can be counteracted by high-pass filtering the image which reduces the gradient but also the difference between the inside and outside contrast. When working with these images a small alteration of the method is applied in which only a ring like feature is compared against the rest to compare only the carbon edge against the rest of the micrograph. Although, this can sometimes fail in case of large dark objects in

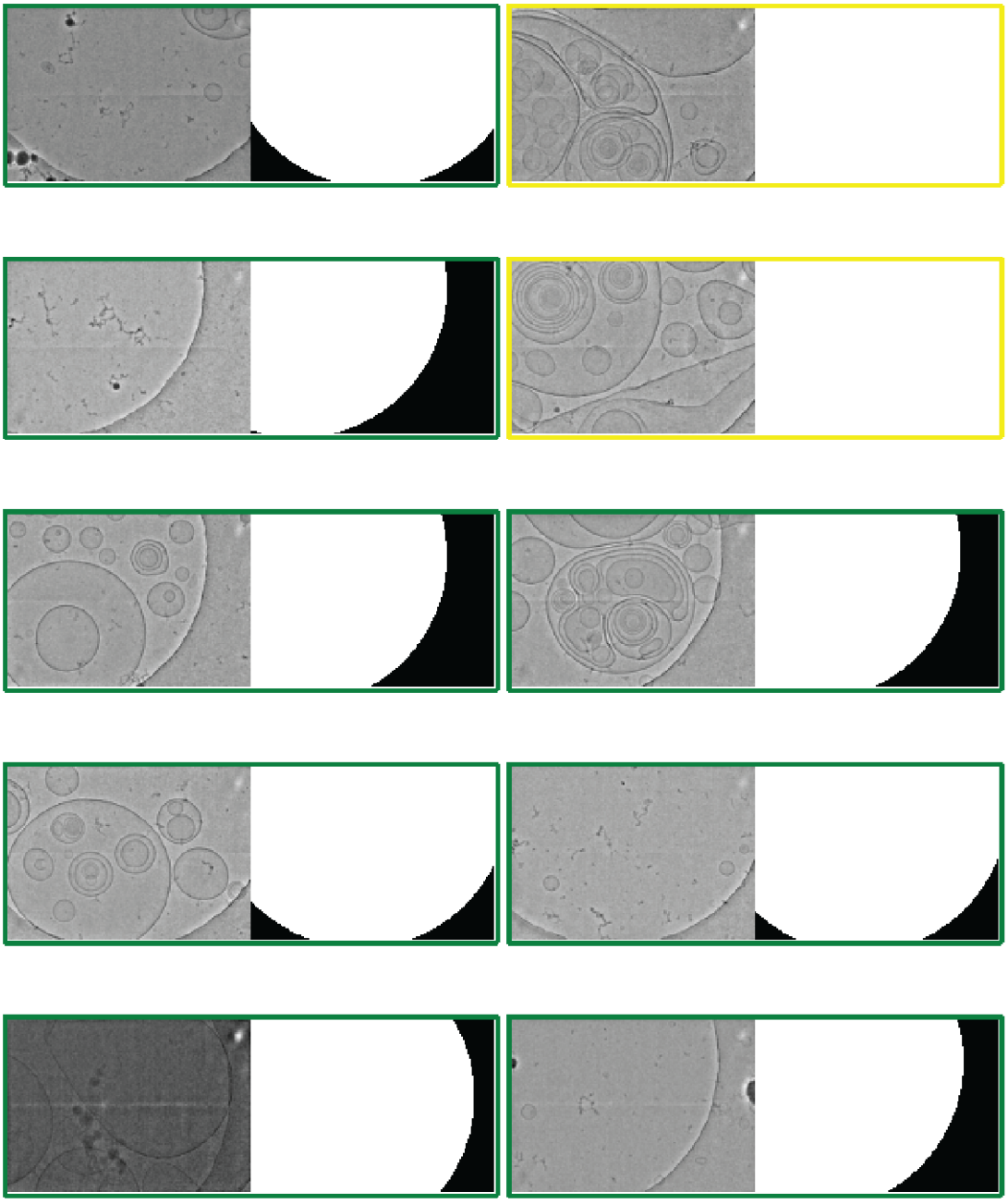

FIGURE 3.19: Examples of edge detection output. The binary images are the created masks after the hole is detected. Green edge means a hole was found an yellow means no hole was found.

the micrograph like in the previously published methods as mentioned earlier.

To distinguish between micrographs with visible carbon edges and micrographs without carbon edges a threshold for the minimum difference is used (Figure 3.19). Further optimization for each dataset can be applied by various parameters. It is possible to set the minimum percentage of the image which should be inside the grid hole, as well as the maximum percentage of the image which is allowed to be outside. The width of the ring can be set when working with high-pass filtered images as well as the pixel size to work with.

Sometimes not only images inside the holes are acquired but also only on the carbon. No carbon edge is visible and it is difficult to find out if the image was acquired on the carbon. If the dataset is large enough another method can be used to discern whether images are completely inside the hole or on the carbon. When plotting the median values of the micrographs two distinct distribution should be visible which can be then labelled by choosing a reasonable threshold value (Figure 3.20). All particles with lower values are found on the carbon because imaging through carbon results in lower pixel values.

The mask can subsequently be used to filter picked particles in Relion (Scheres, 2012) or CryoSparc (Punjani et al., 2017) jobs as well as filter segmented membranes in CryoVIA datasets. This filtering can lead to faster runtimes for 2D and 3D averages in SPA, better resolution in 3D protein models and more precise analysis of membranes. Particles on the carbon film have less contrast and can interact with the carbon which would lead to altered results when analysed. This method remove the effects these particles will have on the analysis.

3.4.7 Local membrane bilayer thickness estimation**

As the segmentation and the contour detection are usually performed on a lower resolution micrograph (the default network segments at 7 Å/pixel), the contour has to be refined to the original resolution of the micrograph. A modified procedure

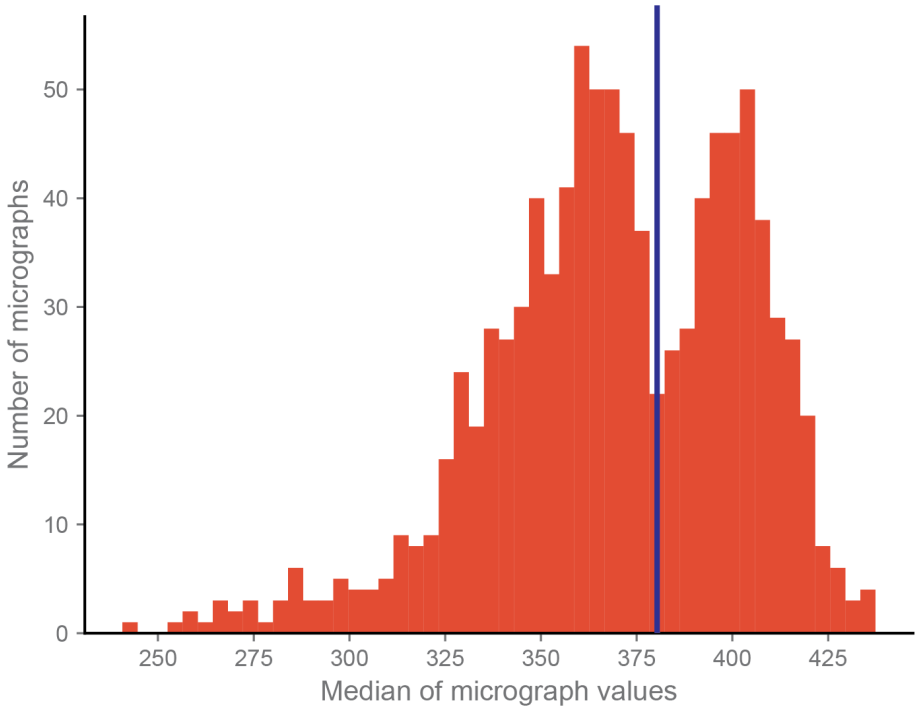

FIGURE 3.20: Histogram of the median value of all micrographs which do not show a visible carbon edge in an example dataset. The blue line indicates a possible threshold value to separate images of carbon (left) and images of ice (right).

based on local pixel averaging from Heberle et al., 2020 was employed: After interpolating the contour pixels onto the original micrograph size, the distance between the contour pixel and all pixels surrounding the contour pixels was estimated up to a predefined maximum distance. The distance of pixels within the vesicle was considered as negative to differentiate between the different directions. In the next step, all pixel density values for the same distance bin were smoothened with a Gaussian filter with a sigma value of 10 Å, averaged and plotted as a function of distance from the contour. The values were smoothened by a Gaussian filter until two distinct minima can be extracted on either side of the contour and their distance taken as the bilayer thickness.

3.4.8 Local membrane curvature estimation*

To estimate the local curvature at a specific membrane the corresponding pixel coordinate and neighbouring pixel along the membrane contour up to a predefined threshold are gathered. The threshold represents the sensitivity of the curvature estimation algorithm. As a next step a circle with its unknown parameters radius and center coordinates is fitted to the gathered coordinates. The fitting algorithm weights all coordinates equally and is based on minimizing the sum of differences between the mean distance to the fitted center and the individual distances per pixel. The reciprocal value of the radius of the fitted circle is then considered as the curvature value at the current pixel. To differentiate between negative and positive curvature a small step towards the estimated circle center is calculated. If this step results in a coordinate which is inside the vesicle the curvature is considered negative, otherwise it is considered positive.

The local curvature is calculated at each contour point of the membranes. For each point j, a neighbourhood Mj is extracted:

$$M_j = \{x \in V : d_j(x) < max\_dist\}$$

where V is the set of all points assigned to the current membrane, $dj(x)$ is the distance between j and x along the contour of the membrane, and max_dist is a set variable that affects the sensitivity of the curvature estimation. For closed membranes, the maximum value for max_dist is $c/4$, where c is the circumference of the closed membrane. In the next step, the curvature $curv_j$ at each point j is estimated by

$$curv_j := \left(\frac{\sum_{m \in M_j} eucl\_dist(center_j, m)}{|M_j|}\right)^{-1}$$

$$center_j := y \in \mathbf{N}^2 \text{ where } y \text{ is one of the minima in } \{dist\_sq_j(x) : x \in \mathbf{N}^2\}$$

$$dist\_sq_j(r) := \sum_{m \in M_j} \left(eucl\_dist(r, m) - \frac{\sum_{n \in M_j} eucl\_dist(r, n)}{|M_j|}\right)^2, r \in \mathbf{N}^2$$

where $eucl\_dist(x, y)$ is the Euclidean distance between x and y, $center_j$ is the center of the best-fitting circle for the neighbourhood of point j, and $dist\_sq(r)$ is the sum of squares of the differences between the Euclidean distances of r and x, and the mean of the Euclidean distances between all points of M_j and r for all points x in M_j. contour but can results in low sensitivity if the neighbourhood distance threshold is too high and no differences in large vesicles with only slight curvature. Therefore a second option was implemented to adapt to the local curvedness of the membrane. This adaptive curvature method estimates the curvature by fitting circles to increasing numbers of neighbouring contour points. After every step the sum of errors is calculated and if this sum exceeds a predefined low threshold the previous fitted circle is used for curvature estimation. The method is more sensitive towards highly curved areas but can also detect small changes in less curved segments. The minimum neighbouring distance has still to be set to a reasonable distance to counteract small segmentation errors. The drawback of this adaptive method is the highly increased runtime depending on the minimum and maximum distance as well as the step size between these two values. For cases where the curvature of membranes is highly interesting this method is to be preferred.

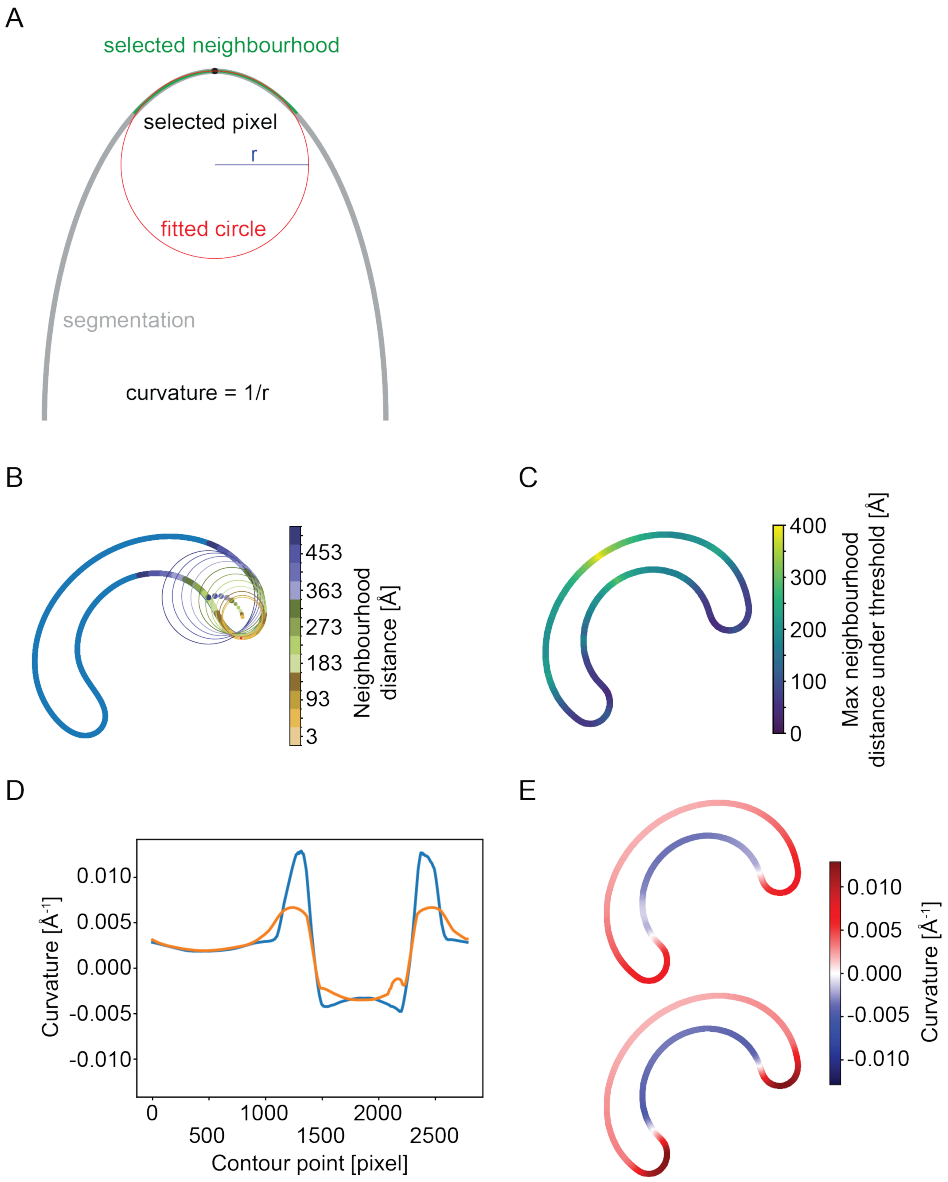

FIGURE 3.21: **Illustration of the curvature estimations methods used in CryoVIA. (A) Illustration of the curvature estimation method. Grey: Segmentation. Black dot: Pixel location of curvature evaluation. Green: Neighbouring pixel to fit a circle to. Red: Fitted circle. Blue: Radius of the fitted circle. The curvature is estimated as the reciprocal value of the radius of the best fitting circle. (B) Illustration of neighbourhood distances for a single point (red dot) on the contour of the vesicle. The coloured circles show the best fitting circle with their center being highlighted. This shows the influence of the neighbourhood distance parameter for the curvature estimation by demonstrating too large circles fitted at a high curvature segment. (C) Illustration of the maximum neighbourhood distance at every contour point. The maximum neighbourhood distance is estimated by the largest fitted circle with a sum of errors below a predefined threshold. High curvature segments of a low maximum neighbourhood distance while low curvature segments of a high maximum neighbourhood distance. (D) A graph showing the curvature at every contour point of the vesicle shown in B, C and E. The graph shows the different in regular curvature estimation (orange) and the adaptive curvature estimation (blue). (E) Curvature values from D mapped to the vesicle shape. Top: Regular curvature estimation. Bottom: Adaptive curvature estimation.

3.4.9 Shape classification*

Vesicles were found in varying sizes and orientations on the micrographs. As the curvature decreases with increasing vesicle size, vesicles must be normalized to have consistent values for a one-dimensional convolutional neural network classifier. As a first step, the vesicles were rotated such that the two most distant points of the contour was aligned horizontally by rotating the vesicle. After rotation, the vesicle was also resized to a fixed size of 200 pixels between two points used for rotation. The ratio of the new vesicle width to the originally rotated vesicle width was then used to normalize previously calculated curvature values. To provide a consistent input to the classifier, the curvature contour was interpolated to 200 values. For the classification, the contour was shifted to the smallest curvature value at the beginning and reversed when the first maximum appeared in opposite direction.

Chapter 4

Membrane analysis in tomograms

*This chapter highlights two implemented methods for studying membranes in three dimensional space - in tomograms. The first method uses the established CryoVIA software tomogram slices and the second method expands the utility of an already existing membrane analysing pipeline (Barad et al., 2023) by adding bilayer thickness estimation. While CryoVIA is published (Schönnenbeck, Junglas, and Sachse, 2025) the usage for tomogram slices was not yet established. The thickness estimation method for tomograms is not yet published in a peer-reviewed article but uploaded to github (*https://github.com/philipp-schoennenbeck/surface_morphometrics_wrapper*).*

4.1 Introduction

The main advantage of using tomograms for analysis, interpretation and general research is the reconstruction of the three dimensional volume. The element or region of interest can be analysed with the surrounding context along the z-direction of the electron beam and a deeper understanding can be established compared to analysing 2D micrographs. However, this analysis is also more complicated because gathering important information from tomograms manually is often done by viewing individual slices. Established software suites can help to address this tedious task by analysing the three dimensional data (Barad et al., 2023, Stalling, Westerhoff, and Hege, 2012) but they are limited to their specific applications. It

is therefore common practice to reduce dimensions and to rely on analysing single slices of tomograms.

In the first part of this chapter, the released CryoVIA software designed to work on 2D micrographs (Schönnenbeck, Junglas, and Sachse, 2025) is tested on whether slices of tomograms can be equally used. While this method is not expected to yield better results than software designed for tomogram analysis, it is a validated approach to gather information about membrane structures in tomograms. Estimating the size of vesicle is straightforward to estimate although the selected slices have the biggest effect on the seen vesicle cross-sections. Curvature estimation can still be used to find uncommon local membrane structures, which may indicate the presence of a protein of interest or a membrane-membrane interaction. Enclosed vesicles and the distance to the enclosing vesicle is equally possible to estimate although the minimum distance could be different depending on which slice is used for the analysis. Therefore, the following section will focus on whether segmentation using the provided tools of CryoVIA for tomogram slices is equally applicable and useful as other software solutions.

Ideally though, tomograms can be analysed directly and the analysis is not relying on single slices. The script pipeline *surface morphometrics* (Barad et al., 2023) captures several aspects of membrane segmentations in tomograms. It is a pipeline of tools to generate robust open mesh surfaces from voxel segmentations of biological membranes using the screened poisson algorithm (Kazhdan and Hoppe, 2013) then estimate morphological features including curvature and membrane-membrane distance using pycurv's vector voting framework (Salfer et al., 2020), and tools to convert these morphological quantities into morphometric features (Barad et al., 2023). The original work was introduced by showing that it could reveal changes in mitochondrial morphology during ER stress by estimating membrane-membrane distances between the inner and outer membrane as well as angles between cristae and the inner membrane.

Bilayer thickness estimation has been established for 2D micrographs with high

resolution (Heberle et al., 2020, Heberle et al., 2023, Schönnenbeck, Junglas, and Sachse, 2025). In these micrographs, the bilayer is clearly visible with the denser hydrophilic part of the lipid separated by the less dense fatty acid chains. The distance between these two headgroups can then be estimated and used as a measure of membrane thickness. Conversely, tomograms usually have lower resolution due to the limited electron dose in biological samples distributed over more images from the tilt series and the following reconstruction. Therefore, the lipid bilayer is often only visible as a single dense element. The two denser layers can sometimes be visible but are usually more noisy and less consistent than the equivalent areas in micrographs. This is one of the reasons why it is more complex and difficult to estimate the bilayer thickness in 3D tomograms compared to 2D micrographs.

Another difficulty for bilayer thickness estimation in tomograms is the automatic location of membrane features in the volumes. However, this issue has largely been solved by several publications of either membrane specific segmentation methods (Lamm et al., 2022, Martinez-Sanchez et al., 2014) or software to facilitate the training of a neural network for tomogram segmentation (Object Research Systems, 2024, Stalling, Westerhoff, and Hege, 2012).

Because the acquisition of high quality tomograms is very tedious and requires a lot of time and expertise in the technique, quantitative analysis using tomograms is very cumbersome and sometimes not feasible. In the recent years various advancements in microscope hardware (Kühlbrandt, 2014), software, image as well as volume processing methods have improved the ability to acquire high quality tomograms in a short time frame (Scheres, 2012, Buchholz et al., 2019, Mastronarde and Held, 2017, Stalling, Westerhoff, and Hege, 2012, Lamm et al., 2022, Zheng et al., 2022, Liu et al., 2022) leading to a greater need of ways to analyse these volumes.

Here I use a pre-trained neural network from *membrain* (Lamm et al., 2022) to create segmentations of vesicles in a tomogram. *Membrain* is a software suite to find protein complexes bound to membranes in cryoEM tomograms using deep neural

networks. Using a network to score samples, subvolumes along the membrane as well as a clustering algorithm allows *membrain* to reliable find membrane-bound protein complexes. Because the detection of the membrane structures is needed for the extraction of subvolumes of the protein complexes, a U-Net (Ronneberger, Fischer, and Brox, 2015) was trained on manually curated segmentations and is also provided as a standalone tool for easy membrane segmentation in tomograms. This U-Net was used to create a 3D segmentation of a tomogram for the membrane thickness estimation in tomograms.

I set out to use the established *surface morphometrics* pipeline as a basis to estimate bilayer thickness in cryoEM tomograms. The vesicles in the example tomogram are extracted, processed by the *surface morphometrics* pipeline and the bilayer is further characterized using a new thickness estimation method. Additionally, the existing pipeline is improved by adding more parallelization support and additional features for easier and more accurate analysis by removing artifacts produces by the the mesh creation. The improved pipeline is here called the *surface morphometrics wrapper*.

4.2 Results

4.2.1 Example tomogram

To show the effectiveness of the introduced methods an example tomogram with a lot of visible vesicles is used as input. The example tomogram shows VeroE6 cells overexpressing blue-fluorescent-protein-tagged DFCP1 resulting in shedding of a large amount of small vesicles (Figure 4.1). The tomogram shows clusters of small vesicles, lipid droplets and another membrane structure, hypothesized to be ER.

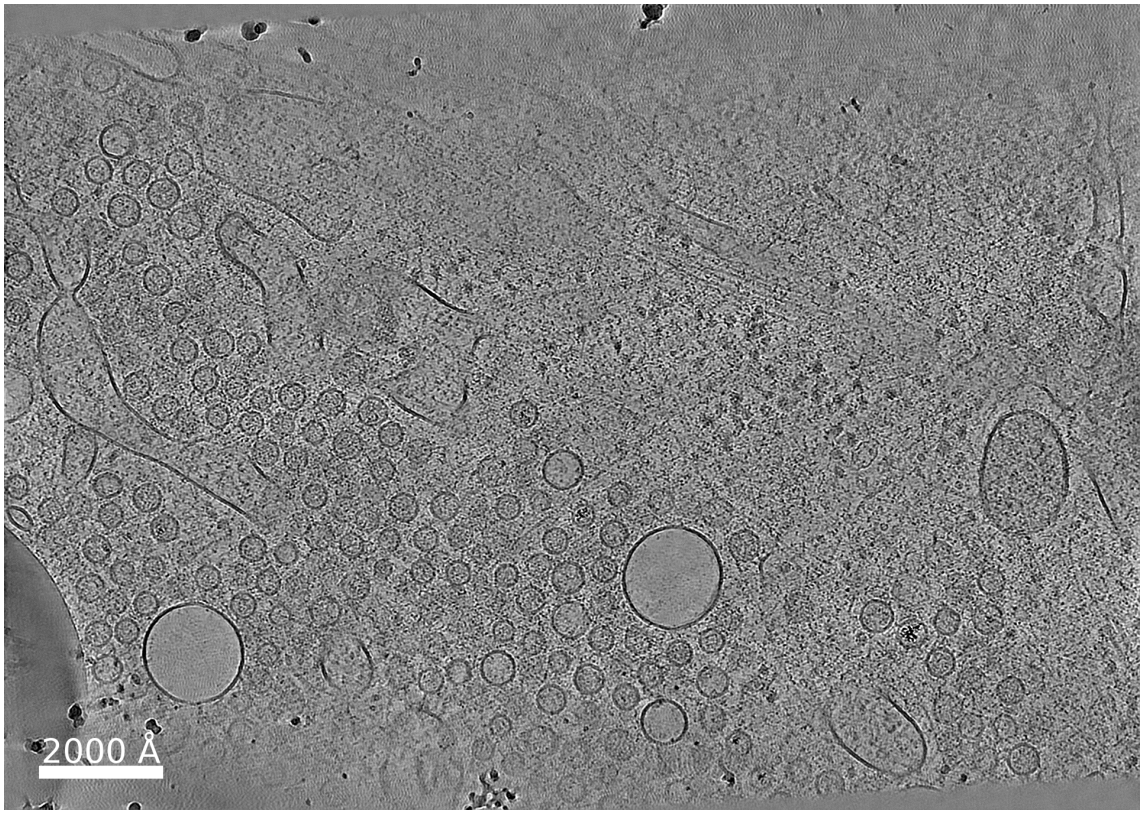

FIGURE 4.1: Tomogram of cytosolic small vesicle shedding in VeroE6 cells. VeroE6 cells overexpressing BFP-DFCP1 were vitrified and areas of interest in the cells were thinned using a focused ion beam scanning electron microscope (FIB-SEM). DFCP1-positive areas were localized using correlative light and electron microscopy (CLEM) and tomograms on these areas were collected with a Titan Krios equipped with a K3 Detector using a dose-symmetric scheme. The tomogram shows large areas of the cytosol covered with small vesicles with approx. about 50 nm in diameter. The vesicles are usually found in large clusters of several hundred units and show close proximity to lipid droplets. Kevin Boga prepared cells and provided the tomogram for further analysis.

4.2.2 Analysing the example tomogram with CryoVIA

To use CryoVIA for analysing tomogram slices, multiple slices through the z-axis are extracted from the example tomogram. Both the original tomogram as well as a denoised tomogram by CryoCare (Buchholz et al., 2019) were used as an input. As single slices of tomograms have much lower resolution than a single 2D micrograph, the segmentation was performed on averaged slices.

The pre-trained neural network provided by CryoVIA was trained on a pixel size of 7 Å/pixel and the example tomogram analysed here has a pixel size of 10.5 Å/pixel. Prior to the segmentation, the images are resized to the pixel size at which the neural network was trained on. The resizing is usually not a problem for 2D micrographs because they are recorded at a much higher resolution but it leads to problems when working with images at a lower resolution than 7 Å/pixel. When resizing images to a larger image size, several artifacts are introduced and information is interpolated, which would be available at a higher resolution. The resulting segmentation will therefore be not as good as a segmentation of a neural network trained at a lower resolution. Therefore, another U-Net was trained on the same training data as the default neural network but at a pixel size of 11 Å/pixel. The difference in segmentation can be seen in Figure 4.2.

The only difference between the two trained neural networks is the pixel size the input images are resized to during training and for prediction. The shown segmentation inputs shown in Figure 4.2 are averaged slices of the example denoised tomogram with 20 slices used for the averaging. It is very clear that the newly trained network at the higher pixel size creates better segmentation over all the examined slices. The resizing from 10.5 Å/pixel to 7 Å/pixel for the default neural network introduced artifacts which were not present in the training data recorded at a much higher resolution. All following results use the newly trained neural network with a pixel size of 11 Å/pixel.

The number of slices to average is also varied from a single slice to 75 slices. An

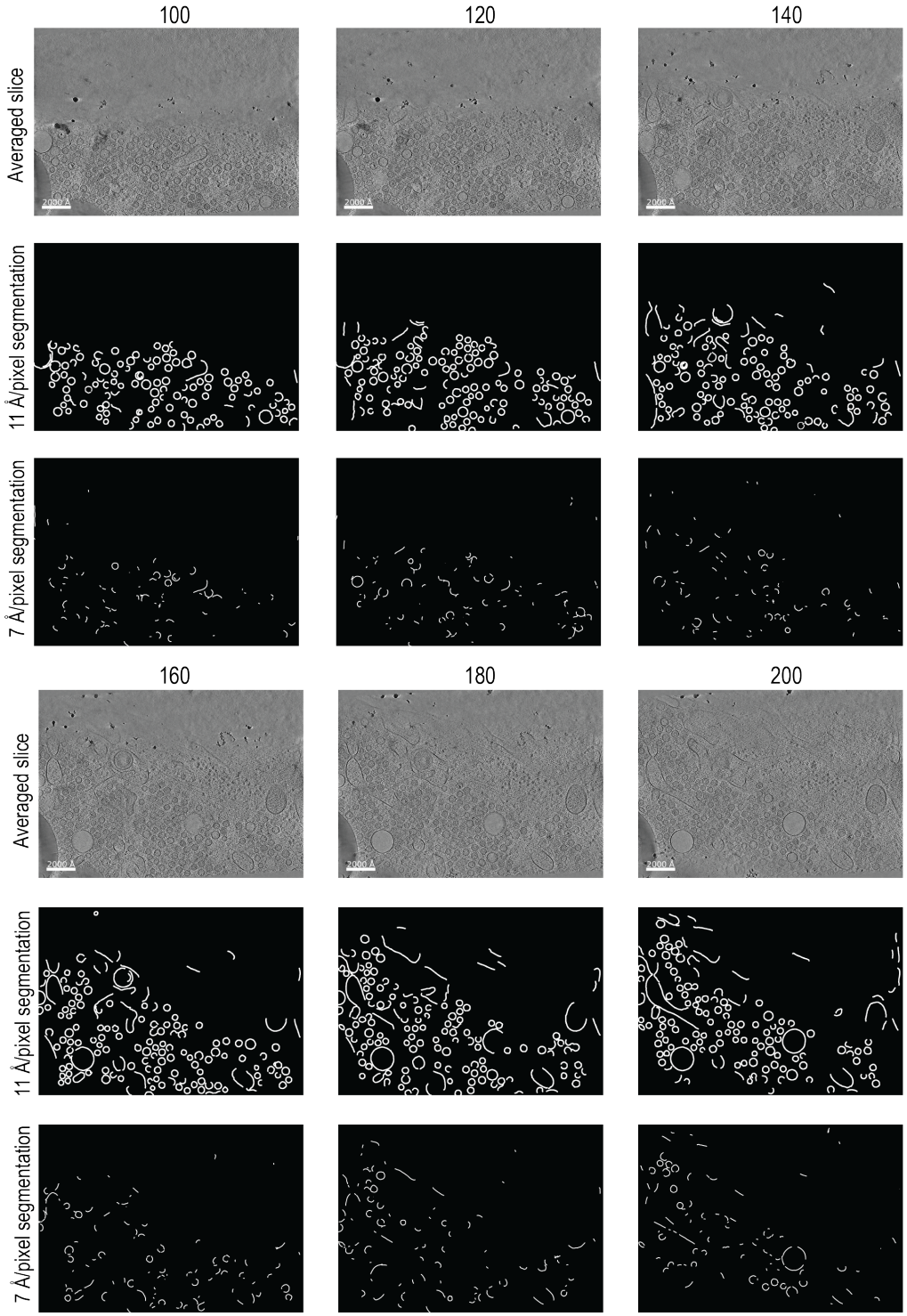

FIGURE 4.2: The segmentation result of 6 tomogram slices (top) using a neural network trained at 11 Å/pixel (middle) and a neural network trained at 7 Å/pixel.

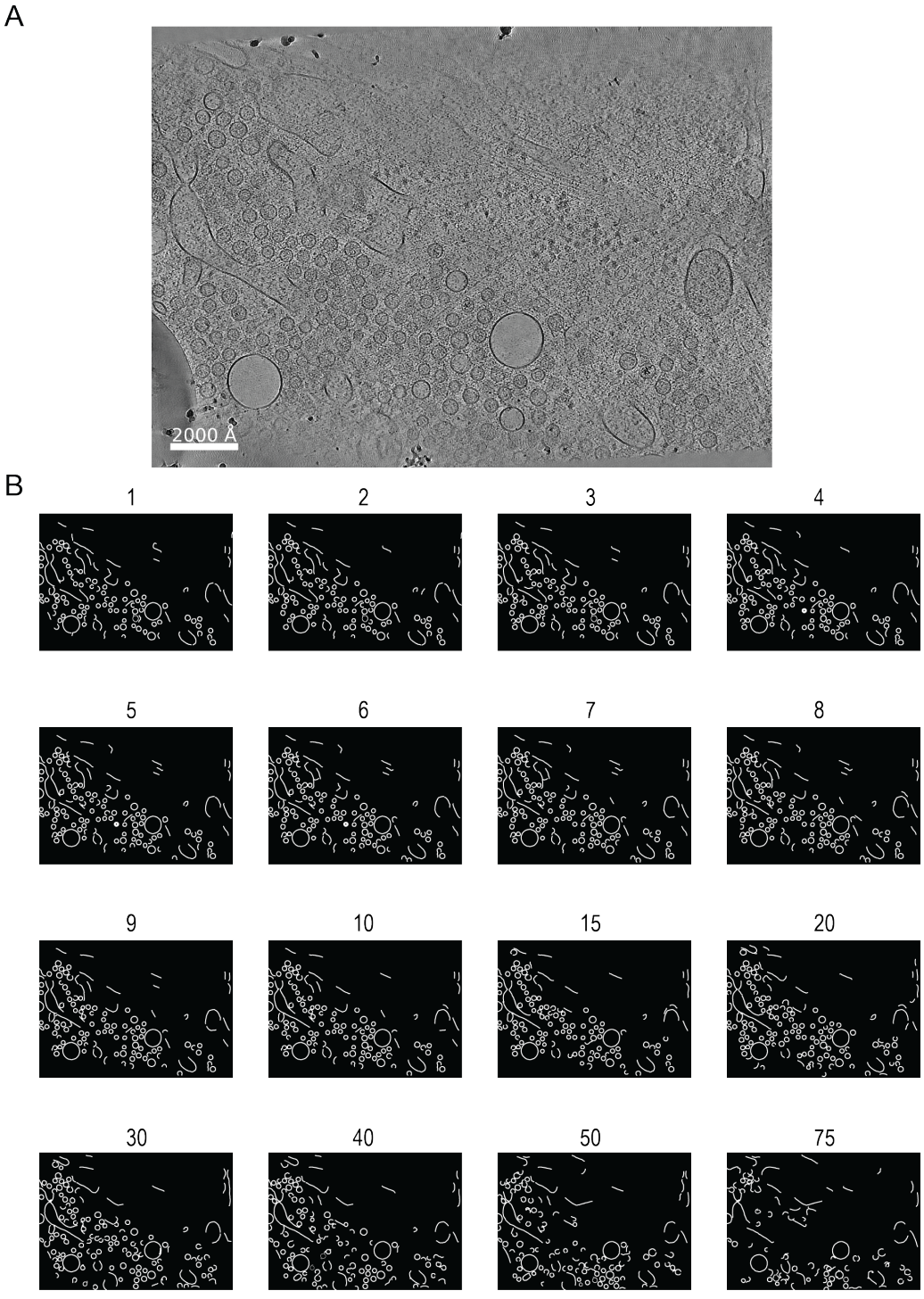

FIGURE 4.3: (A) Example slice number 200 of the denoised tomogram. (B) Segmentation of the slice shown in (A) using varying number of slices for averaging.

example segmentation for slice 200 for the different numbers of averaged slices (n) of the denoised tomogram can be seen in Figure 4.3. The segmentations were visually checked to remove any false positive membrane identifications, but almost no falsely segmented membrane was found. To compare the different segmentations, the total number of closed vesicles for all 10 available slices for each n is summed up. The same procedure was performed for the segmentations of the original noisy tomogram and the comparison between the segmentation results can be seen in Figure 4.4 and 4.5A,B.

While the segmentation with *n=1* already leads to ~500 segmented closed vesicles across the 10 averaged images, averaging more slices leads to better segmentation results with *n=4* to *n=10* resulting in ~550 vesicles (Figure 4.5). The number of segmented vesicles peaks at ~600 vesicles for *n=20* and then rapidly decreases with more slices averaged. This result emphasizes that while it is possible to use the neural network trained on 2D micrographs for segmentation of averaged tomogram slices, figuring out the optimal number of slices to average is required for the best results. While the segmentation were visually checked for any falsely segmented membranes, no check was performed to remove segmentations of the same vesicles in adjacent z-slices. The overall number of segmented membranes still represents the segmentation accuracy of the given parameters but does not accurately reflect the number of vesicles in the complete tomogram. A result of the segmentation using 20 slices for averaging for the different slices of the tomogram can be seen in Figure 4.6.

Another approach is to train a neural network on averaged tomogram slices with the same number of slices for averaging, but this will require a lot more work of manual segmentation. Here, the optimal number of slices for averaging seems to be around 20 slices, but this can differ for every tomogram depending on the quality of the sample, the image acquisition scheme, the used magnification and the reconstruction quality.

The example tomogram was denoised with CryoCare (Buchholz et al., 2019) which

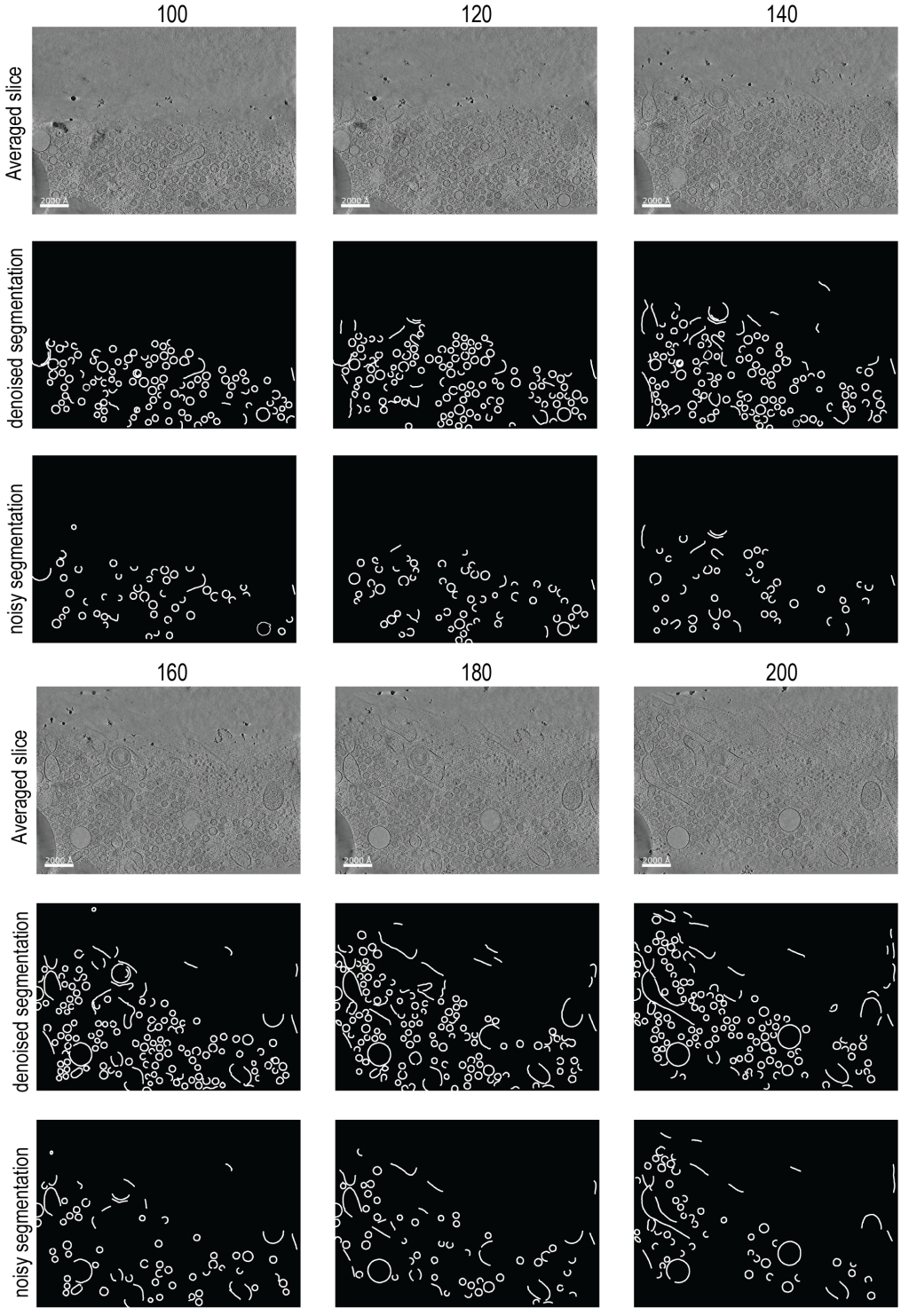

FIGURE 4.4: The segmentation result of 6 tomogram slices using 20 slices for averaging. The number above indicates the selected z-slice and shown underneath is the selected denoised slice and the segmentation of the denoised and noisy tomogram slice.

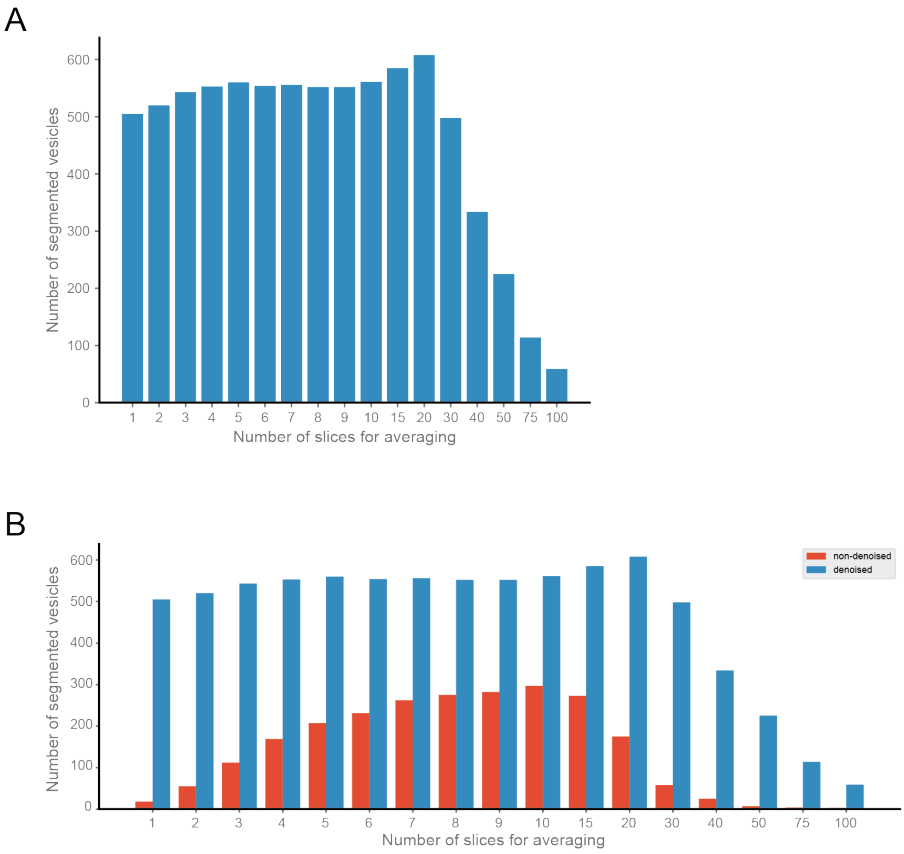

FIGURE 4.5: (A) Histogram of found complete vesicles in all 10 tomogram slices when using various number of slices to average the denoised tomogram. (B) Histogram of found complete vesicles in all 10 tomogram slices when using various number of slices to average the denoised tomogram (blue) and the noisy original tomogram (orange).

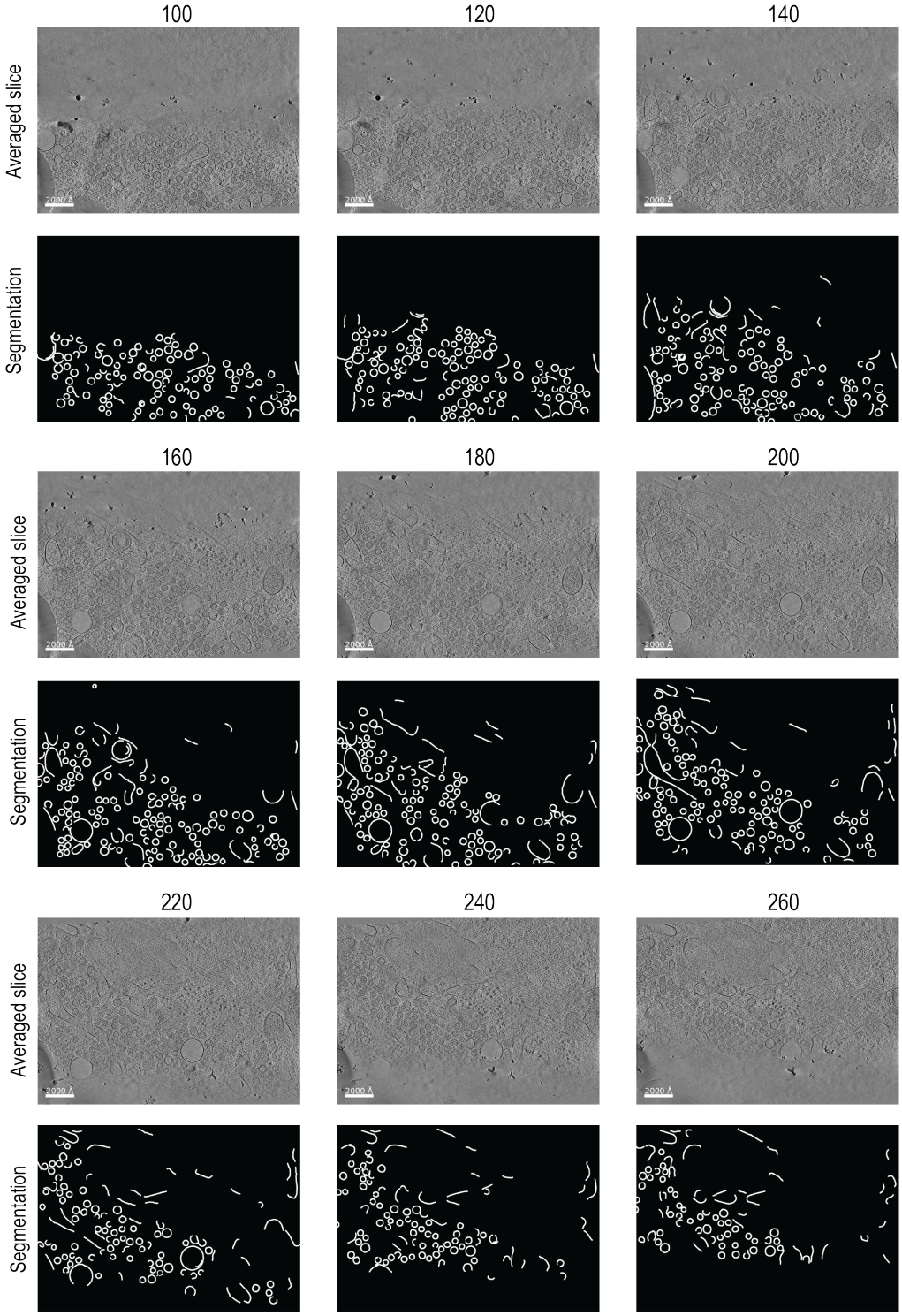

FIGURE 4.6: The segmentation result of 9 tomogram slices using 20 slices for averaging. The number above indicates the selected z-slice and shown underneath is the selected denoised slice and the segmentation of the denoised tomogram slice.

enhances the visual representation of the data and reduces the noise. This denoising also affects the segmentation result because the membranes are more clearly visible. Additional segmentation was performed on the non-denoised tomogram to show the difference in segmentation result (Figure 4.5B). The segmentation of the non-denoised tomogram results in significantly fewer closed vesicles found across all slices. For *n=10* the most vesicles were found with ~300 vesicles compared to the ~550 vesicles from the same *n* for the denoised tomogram. This demonstrates the effectiveness of the denoising as well as it reveals another optimization method when working with tomogram slices. When comparing the amount of found vesicles in averaged slices of the noisy and denoised tomogram with the same *n*, it is clear that the amount of slices to average has a much stronger effect when using noisy tomograms. This can be explained by the denoising method already including information from surrounding slices when denoising tomograms (Buchholz et al., 2019).

In conclusion, there are three main parameters to consider and to adjust when working with tomogram slices:

1. Whether to use the original tomogram or a denoised version.
2. Which neural network to use for the segmentation and which pixel size it was trained on.
3. How many slices to use for averaging to increase the contrast of the used slices.

These parameters can slightly change when analysing different tomograms, but the overall scheme stays the same. If the original tomogram is very noisy and it is difficult to identify membrane structures, it is advisable to use a denoised version of this tomogram. The neural network should be trained on a higher or equal Å per pixel value than the pixel size of the tomogram. The number of slices depends on whether a denoised tomogram is used but a value between 10-20 should work reasonably well. To get the best results for our example tomogram, I used a tomogram

denoised by CryoCare, a neural network trained on a pixel size of 11 Å per pixel, because the pixel size of the tomogram is 10.5 Å per pixel, and number of slices used for averaging was set to 20.

4.2.3 Bilayer thickness estimation in tomograms

Surface Morphometrics Wrapper

While the *surface morphometrics* pipeline is usable as it is, it is sometimes difficult to use for researchers with a biological focus and non-computational background and it is missing some additional features. For this reason a wrapper was written to improve the existing pipeline. With this wrapper various steps have been parallelized and a preprocessing step has been introduced to remove small unwanted segmentation errors by filtering out connected components with a size below a specified threshold. Additionally, calculations for each connected component can be performed individually. This removes some unwanted artifacts in which close membranes were combined and information was lost. Lastly, thickness estimation of the membrane bilayer was added to the analysis pipeline using the extracted coordinates as well as the calculated normal vectors by pycurv for each coordinate. As an example, I use the same example tomogram of VeroE6 cells. The segmentation for this tomogram was obtained by using a pre-trained neural network from *membrain* (Lamm et al., 2022).

A total of 576 membrane structures were identified in the tomogram by separating connected components in the segmentation after removing components that consist of less than 5000 pixels. Most of the found membrane structures are small vesicles but also some larger vesicles as well as other membrane structures from cell organelles can be recognized. After running the *surface morphometrics* pipeline with the addition of the thickness estimation some interesting results can be seen. In the following sections, the result of the local median method (see 4.5.3) is referred to whenever the estimated thickness of a membrane structure is mentioned

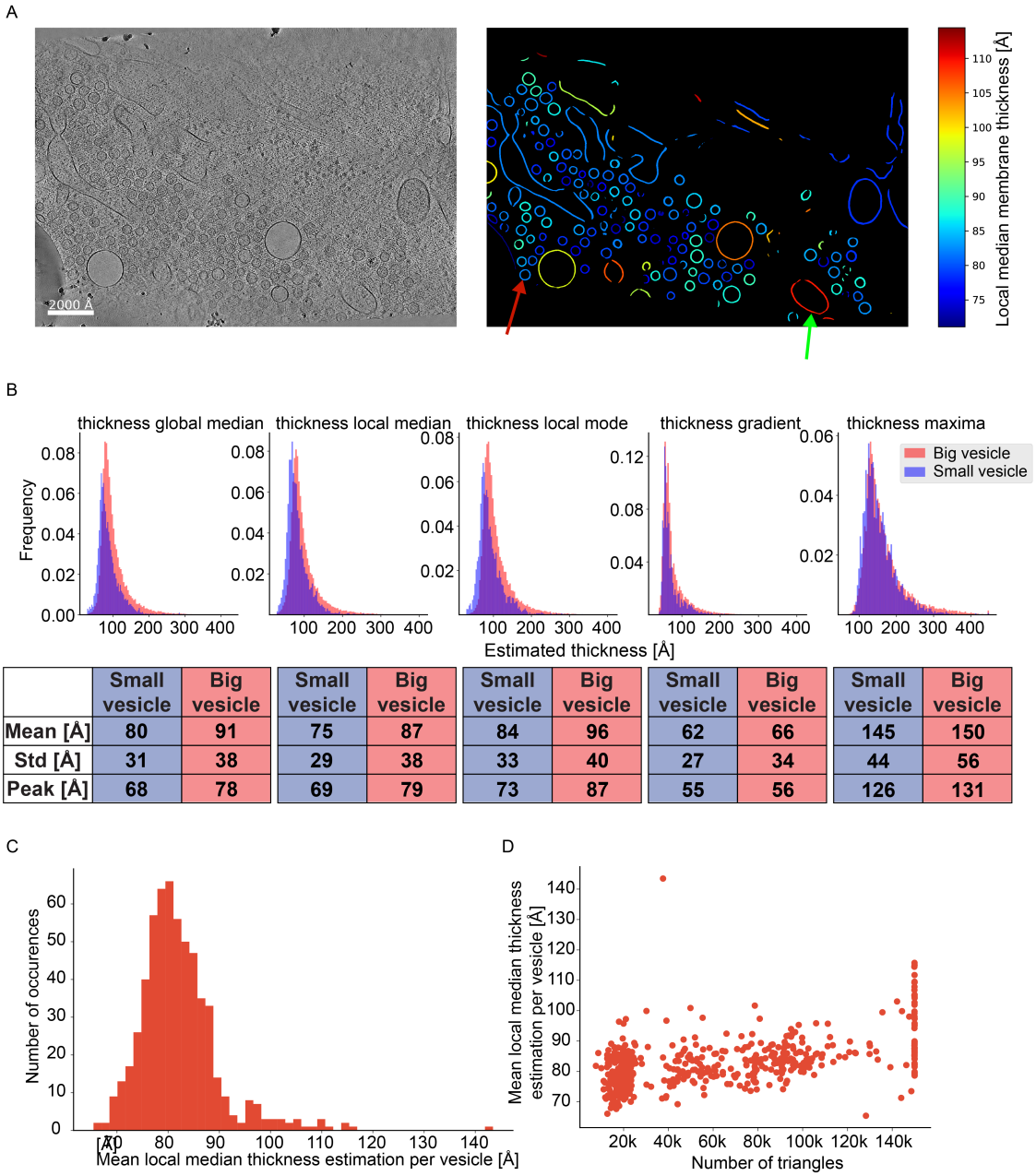

	Small vesicle	Big vesicle	Small vesicle	Big vesicle	Small vesicle	Big vesicle	Small vesicle	Big vesicle	Small vesicle	Big vesicle
Mean [Å]	80	91	75	87	84	96	62	66	145	150
Std [Å]	31	38	29	38	33	40	27	34	44	56
Peak [Å]	68	78	69	79	73	87	55	56	126	131

FIGURE 4.7: (A) Left: Slice number 200 of the example tomogram. Right: Mean estimated thickness values mapped on top of the segmentation mapped for every vesicle. Blue indicating lower thickness and red indicating higher thickness. (B) Histograms of the estimated thickness values using the five different methods of the small (blue) and big (orange) vesicles indicated in (A) with the two arrows. Underneath are the corresponding mean, standard deviation and peak values of the small and big vesicle respectively. (C): Histogram of the means of the local median thickness estimation for all the vesicles found in the example tomogram. (D): Scatter plot of the size of the vesicles (estimated here by number of computed triangles) against the means of the local median thickness estimation per vesicle.

unless a specific different method is specified.

In Figure 4.7A the thickness values are mapped onto the segmentation of the middle slice of the tomogram. As an example, the results of the five different methods for two of the vesicles, indicated in Figure 4.7A, can be seen in Figure 4.7B. The thickness estimation of the three threshold methods *global median*, *local median* and *local modal value* all have very similar results and the thickness estimations for the smaller vesicles are overall shifted towards lower values. Most values are found in the range of 64-100 Å and 80-120 Å for the small and big vesicle respectively. The *gradient* method results in a overall lower estimation of the membrane thickness and most values are around 65 Å for both shown vesicles. As the method with the by default highest estimations for membrane thickness, the *maxima* method results two very similar distributions for both vesicles and most of values are found in the range of 125-175 Å.

Most identified membrane structures have an estimated mean bilayer thickness in the range of 70-90 Å with 519 results in and 67 outside that range (Figure 4.7C). 54 of the membrane structures have an estimated mean bilayer thickness above 90 Å and only 13 have an estimated mean thickness below 70 Å. The mapping reveals a probable correlation between the size of the vesicles and their estimated bilayer thickness. When comparing the estimated thickness against the number of triangles calculated by the surface morphometrics pipeline (Figure 4.7D), it can be seen that almost all of the membrane structures with an estimated bilayer thickness of 100 Å and higher have a large number of triangles and are therefore large vesicles or lipid droplets in the tomogram.

It is difficult to estimate the ideal parameters for the thickness estimations and most of them can be optimised per individual tomogram analysis. The default parameters were used on a few different tomograms and seem to be fine for most of them. The height of the extracted cylinder was set to 45 nm, to assure that the whole local membrane structure is extracted, even if the coordinates are not exactly located on the membrane. The radius of the cylinder was set to 4 nm, to be able to have enough

data points along the height of the cylinder to average out some noise. A high pass filter of 150 nm was applied to the tomogram to reduce the effect of contrast shifts across the tomogram. The tomogram was also additionally smoothed with a kernel size of 5 pixels and the perpendicular, averaged profiles were also smoothed by a gaussian filter with a window size of 10 and a sigma of 1.5. Both smoothing methods increase the amount of viable thickness estimations but they also increase the estimated thickness by smearing the averaged profile. This trade of has to be considered and for this example tomogram I used smoothing to extract more viable thickness estimations. There is no ideal solution for this and it depends on the use case of the application.

4.3 Discussion

4.3.1 CryoVIA

I used averaged tomogram slices as an input for CryoVIA to analyse membrane structures visible in the tomogram and to run the CryoVIA analysis for these images. Out of the box, CryoVIA was not able to consistently identify membranes in tomogram slices because the pre-trained neural network was trained at a higher resolution. Retraining the neural network on the same micrographs as the default trained neural network but at a lower resolution improved the segmentation result. While both neural networks were trained on the same data, the default neural network learned to rely on high resolution information for its segmentation. This information is missing when working with images of lower resolution and the resulting segmentation result has a drastically decreased accuracy. Because the initial internal weights of a neural network are assigned randomly and because it is very difficult to understand the internal logic of a trained neural network, it is almost impossible to adjust the weights to adapt to new data, even when the only difference is the scaling factor. Therefore, another U-Net had to be trained on the new

resolution to be able to get good segmentation results. Additionally, both the original and the denoised tomogram were used to analyse the segmentation results. For both tomograms varying numbers of slices were averaged to increase the visual clarity of single slices. Overall, the denoised tomogram resulted in much better segmentations further improved by using multiple slices for averaging reaching the best segmentation results with 20 averaged slices.

The best segmentation resulted in 600 identified vesicles in 10 averaged slices which shows the effectiveness of CryoVIA when analysing tomogram slices, being even higher than the 576 found membrane structures with *membrain* which uses the complete tomogram for segmentation and also considered non-closed membranes. It is therefore possible to use CryoVIA when analysing tomograms but it also comes with some limitations. For reaching the best segmentation results a specifically trained neural network has to be used that has seen data at lower resolution. Additionally, it is necessary to test a series of averaging steps to find the optimum number of averaged slices for ones specific data. A denoised tomogram is also advisable because of the visual clarity it provides. While it can alter data in some ways, it is only relevant in CryoVIA for the bilayer thickness estimation which often does not work directly for tomogram slices anyway because the bilayer is usually not visible.

Surprisingly, the segmentation using the neural network trained on a different pixel size was able to find most of the membrane structure in the tomogram slices although slices of tomograms look distinctively different from micrograph in high resolution. In high resolution micrographs the lipid bilayer is clearly visible and can be used as additional information for the neural network to correctly identify membrane structures. These lipid bilayers are even visible when resizing the micrograph to much higher pixel sizes as for the second trained neural network at a pixel size of 11 Å/pixel (Figure 4.8) but can usually not be seen when inspecting membrane structures in tomograms (Figure 4.8). Additionally, the tomogram used here shows cellular data instead of clean vesicles in a buffer, which is what the

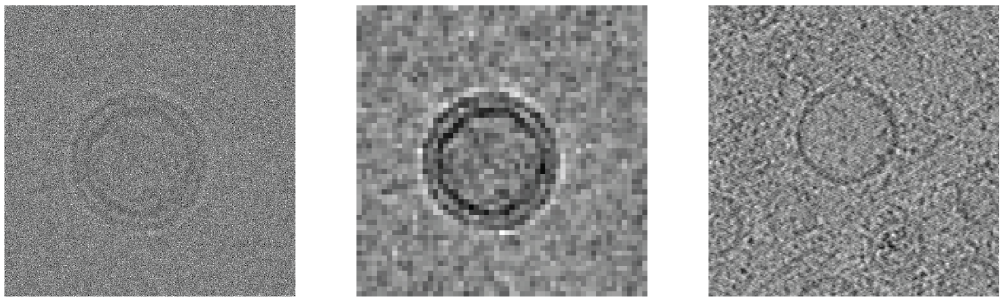

FIGURE 4.8: Cropped out membranes at different pixel sizes and from different sources. From left to right: High resolution micrograph at a pixel size of 1.7 Å/pixel. Resized image from the same micrograph to a pixel size of 11 Å/pixel. Averaged tomogram slice using 20 z-slices with a pixel size of 11 Å/pixel.

neural networks were trained on. Cellular membrane structures greatly differ from artificially created liposomes. The lipid composition is much more diverse, which leads to membranes with a greater variety of bilayer shapes. Furthermore, cellular membrane structure include a large variation of different membrane proteins, which can be connected to the membranes in various ways and alter the visible bilayer structure, making it more difficult for the neural network to correctly identify the membrane structures. The micrographs of the artificial liposomes also contain very few additional particles apart from the liposomes, especially compared to cellular tomograms that are crowded with many types of proteins, filaments and other structures. In conclusion, cellular tomogram slices and high resolution micrographs of liposomes are visually very distinct. The fact, that the neural network is still able to correctly segment most of the membranes in the cellular tomogram slices, shows the generalizability of the membrane segmentation and solidifies the capabilities of the trained neural network.

Because of the previously mentioned caveats with membrane structures in cellular tomogram slices - higher pixel size, lipid distribution and present membrane proteins - the lipid bilayer is often not visible as two distinct lipid layers rather than only one thicker membrane structure (Figure 4.8). This makes the implemented bilayer

thickness estimation of CryoVIA not usable, because it relies on the two distinct minima of the perpendicular profile. While cellular tomograms with visible bilayers exist, the visible membrane structures in tomogram slices are often angled and not perfectly perpendicular, which would skew the estimation. Because of these reasons it is not advisable to use the thickness estimation of CryoVIA for tomogram slices but rather the other introduced method expanding the *surface morphometrics* pipeline.

When analysing the output of CryoVIA one also has to consider that the same vesicle can be visible on multiple slices and can therefore be present multiple times in the statistics. This is a big problem and additional methods have to be developed to reduce these occurrences. The size extracted from the segmented vesicles can also be misleading because the cross section of the vesicles are most often not at the largest diameter. While having the caveats in mind, CryoVIA can be used for analysing tomograms in specific use-cases, but an analysing suite specifically tailored for tomograms would be preferable if available.

4.3.2 Bilayer thickness estimation in tomograms

I introduced a method for estimating bilayer thickness in tomograms by expanding the existing pipeline for analysing tomograms *surface morphometrics* (Barad et al., 2023). The methods uses coordinates and normal vectors from the pipeline's output and creates averaged perpendicular profiles across the membrane segments. Five different thickness estimation methods are shown and extracted for an example tomogram. The resulting thickness estimations are consistent across the vesicles found in the tomogram but also some vesicles with higher thickness estimations were found which hold up when visually examining the tomogram. The local median thickness estimation resulted in most vesicles showing a thickness of ~8 nm ± 1 nm. Typical membrane thicknesses from atomic force microscopy (Attwood,

Choi, and Leonenko, 2013), X-ray scattering (Regan et al., 2019), quantitative differential interference contrast microscopy (Regan et al., 2019) and using 2D cryoEM micrographs (Heberle et al., 2020, Schönnenbeck, Junglas, and Sachse, 2025) usually range from 3-6 nm depending on the method, lipid composition, embedded proteins and the environment. While the estimated values deviate a lot from the previously established values it does not have to mean that they are unusable. The described estimation method relies entirely on visual density of the membrane in a low resolution tomogram often stretching from the very outer edges of the membrane. Additionally, the profiles are smoothened to reduce the noise in the tomograms which can also artificially increase the thickness estimations. While this estimation is not directly comparable with estimations obtained from other methods it is still possible to compare thickness values of varying membranes of different tomograms when both have been estimated using this method. The actual membrane thickness estimated by the various methods and the here estimated values do not show the same range of values but it is very likely that they correlate highly and therefore it makes sense to also call this an estimation for membrane thickness. Additionally, proteins embedded or present close to the membrane can also influence the thickness estimation which can also be used to further develop this method to find membrane-bound proteins for STA.

4.4 Outlook

While I have shown, that CryoVIA can be used to analyse single tomogram slice it is not yet directly implemented in the software suite. To add functionality for tomograms an automatic slice extracting and averaging method can be implemented as well as providing a pre-trained network for lower resolution images. Because the bilayer is often only seen as one dense objects in tomograms the implemented bilayer thickness estimation does not work as well as for high resolution 2D micrographs. The methods used for the *surface morphometrics wrapper* could be implemented in

CryoVIA for averaged tomogram slices but one has to consider that the cross section is not perpendicular to the membrane in three dimensional space which would distort the results of the estimation.

While I have shown that it is possible to estimate the bilayer thickness in tomograms, so far it is only accurate to a certain degree. Further investigation and development is needed to increase the accuracy of this method. Because membrane proteins appear in tomograms as additional densities close to the membrane it is also feasible to use the thickness estimation as protein particle detection. A possible implementation of this method could involve thresholding the estimated thickness values and filtering potential sites with high thickness estimations. Although this method can still be improved it already shows interesting results and can be used to study membrane thickness variance in tomograms.

4.5 Materials and Methods

4.5.1 Example tomogram

The example tomogram shows VeroE6 cells (a continuos adherent mammalian cell line of an African green monkey) containing cytosolic small vesicles. VeroE6 cells overexpressing human DFCP1 were vitrified and areas of interest in the cells were thinned using a focused ion beam scanning electron microscope (FIB-SEM). DFCP1 is a protein associated with various cellular processes including selective autophagy and regulation of lipid droplets. DFCP1-positive areas were localized using correlative light and electron microscopy (CLEM) and tomograms on these areas were collected with a Titan Krios equipped with a K3 Detector using a dose-symmetric scheme up to ± 50° in 2° increments. The total electron exposure was 130.8 $e^{-}/\text{Å}^2$ with 2.32 $e^{-}/\text{Å}^2$ per tilt at a magnification of 24000 using a 20 eV energy filter. Gain and motion correction was done with MotionCor (Zheng et al., 2017) and the reconstruction was created by AreTomo2 (Zheng et al., 2022). The tomogram

shows large areas of the cytosol covered with small vesicles with approx. about 50 nm in diameter. The vesicles are usually found in large clusters of several hundred units and show close proximity to lipid droplets.

4.5.2 Averaged z-slices through the tomographic volume

Due to the inherent lower resolution of tomogram slices compared to 2D micrographs it is reasonable to average multiple slices for analysis which is also a common method when viewing tomograms to improve the visual distinction of the elements of interest. Because it is not obvious how many slices for averaging will lead to the best result multiple different datasets with different amounts of slices are segmented and visually as well as statistically analysed. The example tomogram has 400 slices of which the first and last few slices do not contain any visible vesicles. A total of 10 slices are extracted from slice 100 to 300 with a stepping size of 20 slices. At every step the surrounding *n* slices in both directions are used the calculate the average slice where n is one of 1, 2, 3, 4, 5, 6, 7, 8, 9, 10 ,15, 20, 30, 40, 50 and 75.

4.5.3 Bilayer thickness estimation in tomograms

Coordinate extraction

The first step in the thickness estimation method is to extract the correct coordinates from the output of the previously ran surface morphometrics wrapper pipeline. One of the resulting files from the pipeline is a *csv* file in which each row represents a point on of the membranes found in the provided segmentation. Through various conversion steps, the segmentation is first converted to a coordinate file of all segmentation pixels scaled to the voxel spacing and subsequently converted to a mesh using pymeshlab (Muntoni et al., 2024). The mesh is optimized using a screened poisson algorithm (Kazhdan and Hoppe, 2013) and afterwards further simplified.

Using this generated mesh pycurv can estimate the local curvature as well as normal vectors and the surface morphometrics pipeline can further calculate distances and angles between the different membrane segments.
The coordinates found in the resulting *csv* file are therefore not directly extracted from the segmentation but will be used for the bilayer thickness estimation in the next step. Extracting, scaling the coordinates back to the height, width and depth of the original segmentation result and rounding the coordinate values to the next whole number results in a list of coordinates with a lot of duplicate values due to the fine mesh generating algorithm. Because the thickness estimation method is processing the thickness values at a pixel level the duplicate values are filtered and removed.

Preprocessing

After loading in the tomogram data the range of values are clipped to the range of $mean - standard\_deviation * n$ to $mean + standard\_deviation * n$ where n is a predefined value in the configuration file. This reduces the effect of high pixel value artifacts from image acquisition or reconstruction. Afterwards the values are rescaled to a mean of 0 and a standard deviation of 1 to be more comparable when examining the results. If necessary a high pass filter can be applied afterwards to reduce the effect of gradients across the tomogram which can sometimes be seen. When working with non-denoised tomograms it is also advisable to smoothen the tomogram with a gaussian kernel to enhance the visibility of the membrane structure and reduce the overall noise in the tomogram. Values for the preprocessing steps can be adjusted in the configuration file.

Thickness estimation

To estimate the membrane bilayer thickness at a specific point an averaged profile across the membrane is needed. The average profile is estimated by extracting pixel values in a cylindrical shape across the membrane and averaging the values along

the height of the cylinder. The output of this method is a one dimensional array, optimally with a minimum in a clear valley. The height and radius of this cylinder can be adjusted in the configuration file.

To extract the correct profiles the method iterates over the membrane points. For each point the coordinates of pixels inside the cylinder are calculated along the normal vector previously calculated by the pycurv part of the surface morphometrics pipeline. The values for each pixel are interpolated by the surrounding pixel and the average profile is calculated. For every pixel the local median and local modal value is calculated where the local area is defined as a cube around the current coordinate with an edge length of twice the height of the extracted cylinder.

For every averaged profile the local membrane thickness is subsequently convolved by a gaussian kernel to further smooth the profile. The parameters of this smoothing can also be adjusted in the config file if necessary. At this stage the membrane thickness can be estimated by 5 different methods (Figure 4.9) using the profile as the main input:

- Global median

  Local peak maxima and valley minima are extracted from the given profile. The lowest found minimum which still has a peak in both direction is identified and estimated as the middle of the membrane. The values between the minimum and the two maxima are examined whether they cross the global median value of the given tomogram. If both sides cross the median value the distance between these two indices is calculated and scaled according to the pixel size. This scaled distance is the estimated membrane bilayer thickness for this specific coordinate.

- Local median and local mode

  These two methods work the same way as the *Global median* method but instead of using the global median value of the tomogram to threshold the profile, they use the local median or the local modal value respectively. This

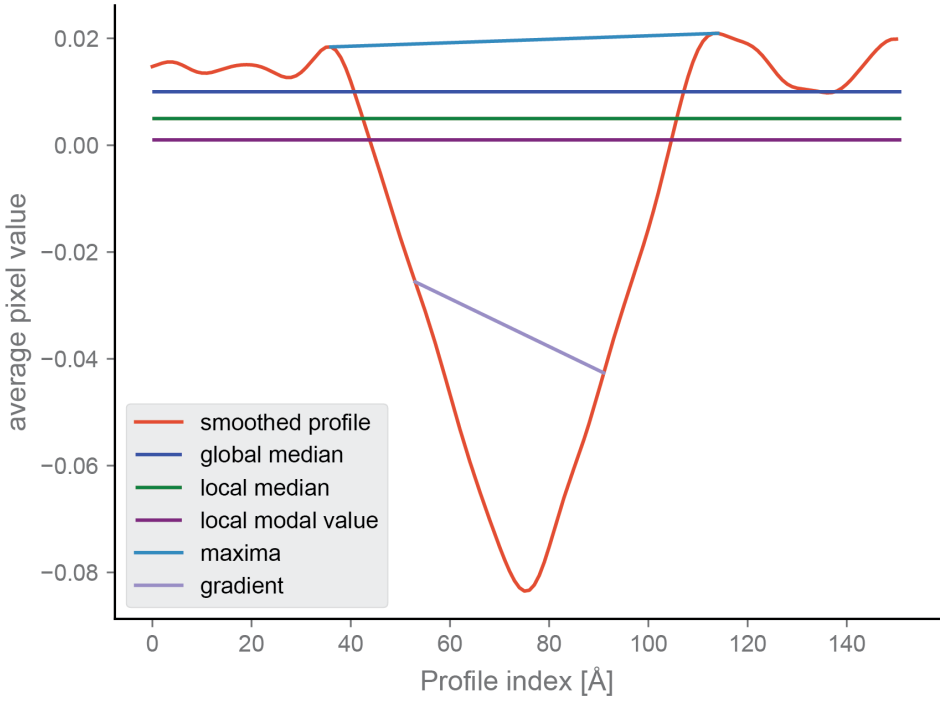

FIGURE 4.9: Ideal example plot of an average profile (not real data). Shows the indices found by the different methods.

method can further mitigate existing gradients in the tomogram or reduce the effect of grey values variance in different cell organelles. Because the local area is focused around the coordinate of the current membrane segment, the median and modal value can be influenced by artifacts or other strongly different grey values in the local area.

- Gradient

  This method starts the same way as the threshold methods but instead of finding the index where the threshold is crossed it will estimate the indices with the highest gradient on each side of the minimum. The distance between these two indices is then scaled and used as the thickness estimation.

- Maxima

  The *maxima* method starts the same way as the other methods. After finding the estimated middle of the membrane the distance between the two surrounding maxima is calculated and scaled to the pixel size. This thickness estimation will therefore always be higher than the threshold and gradient methods.

For all methods it is possible to exclude profiles with irregularities like a low gradient between the minimum and the maxima which could indicate other densities close to the membrane or too close maxima around the minimum which could indicate artifacts from the reconstruction or damage to the membrane during image acquisition.
The thickness estimation of all chosen methods is saved for all membrane segment coordinates and can be further analysed. The results of each method are not comparable but the thickness estimations of multiple different membrane structures can be compared when using the same method.

Chapter 5

Local membrane morphology changes

The two methods described in this chapter aim to automate the creation of logical steps for shape changes in membrane segments. The first method uses variational autoencoders to create a latent space where membrane segments are encoded, clusters the encoded segments and thus creates a possible path between the clusters. Because of some shortcomings of this method a second method was developed that is a semi-automated method to identify shape transitions using dynamic time warping algorithms.

5.1 Introduction

Biological membranes are one of the most important structures in organisms compartmentalizing parts of cells to create different chemical environments. In order to create the perfect organelles, divide into new cells or enclose cargo to digest membranes need to be able to bend, stretch and overall change their shape. Various factors can change the curvature and therefore the shape of membranes including temperature (Seifert and Lipowsky, 1995), osmotic changes (Dimova and Marques, 2022), pH changes or ingested particles (Holló et al., 2021). But also some proteins have membrane remodeling capabilities often resulting in drastic changes to the vesicle shape like tubulation. Those proteins include ATP synthase dimers (Tarasenko and Meinecke, 2021), BAR domain proteins (Tarasenko and

Meinecke, 2021), amphipathic helix-containing proteins (Giménez-Andrés, Čopič, and Antonny, 2018) and phage shock proteins (Junglas et al., 2021). Understanding the effects these membrane-shaping proteins is crucial to understand the complex interactions in cells and organelles. When studying these effects, often a series of steps for the membrane change process is proposed using membrane depictions and actual microscopy images.

When images of vesicles are acquired by cryoEM methods, the membranes are frozen in vitreous ice. This means that they are frozen at a specific time and will stay in their morphological state. To identify time resolved changes in membrane shape, two methods can be used depending on the specific biological setup and question. When the influence of an agent like a protein, heat stress or some other interaction with the membrane is of interest and the interactions are not reversible and ongoing, multiple different time steps have to be frozen. This requires multiple batches of samples where the agent is induced and after various time intervals the sample has to be frozen to be able to see the influence of the agent towards the membranes. The time interval heavily depends on the type of interaction the membrane and the agent and identifying appropriate intervals requires a lot of tries. Ideally various stages of structural changes in the vesicle shape can be identified after acquiring the cryoEM micrographs afterwards.

Another setup could include ongoing changes that may or may not be reversible. In this setup, all of the various steps of the interaction can be seen simultaneously in the cryoEM micrograph and no splitting of the dataset is necessary.

Either of the two setups can than be used to understand the interaction of the membranes with the agent. In some cases the datasets of these processes can reach a few hundreds up to thousands images, which is tedious to scan manually while it is easy to miss important parts of images. The following methods aim to automate the identification of the time steps for local membrane changes and connect them in a sequence.

5.2 Result

5.2.1 Automatic construction of timelines using VAEs

(Variational) autoencoders have been used for various methods in cryoEM. Heterogeneous single particle reconstruction (Zhong et al., 2021), micrograph denoising (Shen et al., 2024) or particle picking (Xu, Zhan, and Xu, 2024) are a few of the examples, in which VAEs have been used in a cryoEM context. The variations in these techniques emphasize the ability of reducing high dimensionality to a low dimensionality latent space. Here, I tried various methods using VAEs to cluster similar membrane segments in the latent space and find a meaningful and logical timeline for the membrane morphology changes. While this method ultimately was not developed further due to input restrictions as well as a rather unorganized latent space the method is still an interesting approach and could be investigated further in the future.

The main idea behind this method is to split the vesicle contour into smaller segments and train a variational autoencoder with 1D-convolution layers to reduce the segments to only a few variables in the latent space. In this latent space similar membrane segments would ideally be clustered close together while dissimilar segments would be further apart. The information of the latent space can subsequently be used to cluster segments, create average segments or find a sequential morphology steps for the membrane segments.

Membrane segment extraction

VAEs require a consistent input shape. In order to provide this input, segments from the established membrane instances from CryoVIA are used. For every vesicle instance the contour coordinates and the curvature contour are extracted and the length along the coordinate contour is calculated. The algorithm extracts then curvature segments and coordinate segments along the vesicle contour for every

predefined step size (Figure 5.1A). The predefined length along the vesicle contour stays constant and the extracted segments are extrapolated to the input shape of the VAE if necessary. The two parameters define the amount and size of these segments, set the sensitivity of the method and also influence the amount of different segment shapes.

Construction of a latent space for membrane segments

The VAE architecture uses 1D convolution layers with increasing filter sizes, a kernel of size 3 and ReLU activation layers. The latent space dimensionality was tested for various sizes of 1D-arrays. The input shape was tested for both curvature segments (shape: (X,1)) (Figure 5.1B) and normalized membrane coordinates (shape: (X, 2)). In all cases the loss at the end of the training was very small and the input could be decoded from the latent space almost perfectly. Sampling the latent space with previously unknown input also created reasonable output which resembled the surrounding encoded membrane segments closely. Using clustering methods like k-means (MacQueen, 1967), dbscan (Ester et al., 1996) or hdbscan (Campello, Moulavi, and Sander, 2013) reveals that closely packed latent space samples are very similar, which validates the latent space construction (Figure 5.1C).

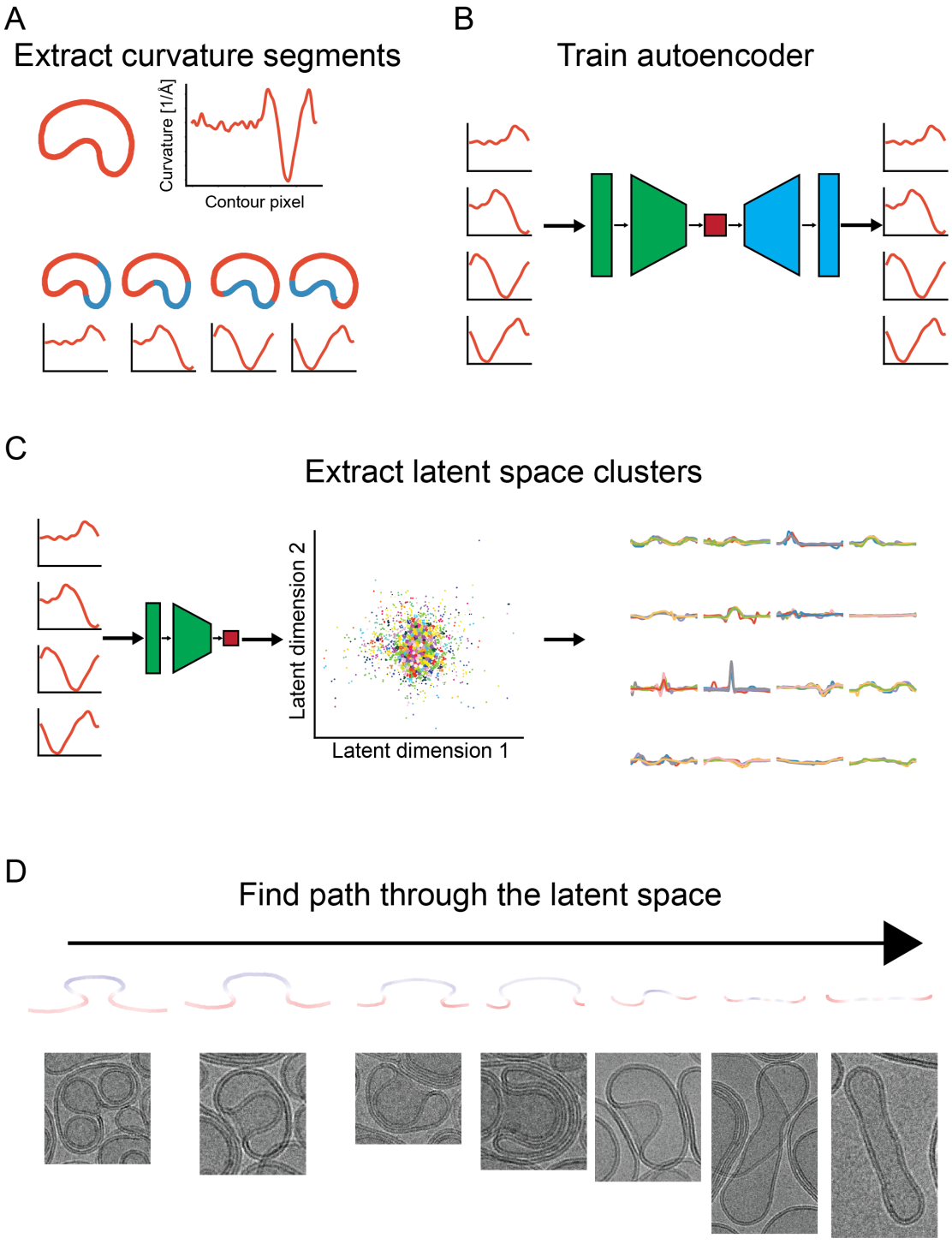
A
Extract curvature segments
Curvature [1/Å]
Contour pixel
B
Train autoencoder
C
Extract latent space clusters
Latent dimension 2
Latent dimension 1
D
Find path through the latent space

FIGURE 5.1: Workflow of the membrane remodeling step detection with VAEs. (A) Extraction of curvature segments from vesicles. Top: Contour and the corresponding curvature. Bottom: Extracted curvature segments from the overlapping contour segments in blue. (B) Training the VAE using the curvature segments as input. Green - encoder, red - latent space, blue - decoder. (C) Left: Encoding curvature values into the latent space using the VAE. Middle: Clustering the latent space using any clustering algorithm. Right: Example plots of curvature segment clusters. (D) From left to right a possible path through the latent space to identify remodeling steps. These plots show the contour segments with the curvature mapped on top of it. Red - positive curvature, blue - negative curvature. At the bottom are the corresponding cropped out vesicles from the micrographs. The steps shown here were extracted by manually selecting cluster cores that were close to each other.

When trying to traverse the latent space from a given starting and end segment multiple methods were tested:

- A linear connection between the two encoded latent space segment was sampled at multiple steps and decoded.
- The mean latent space sample of each cluster was calculated and the distances between the clusters was extracted. Using the starting segment as the first point traversing the latent space from cluster mean to cluster mean always using the next closest cluster until the defined ending cluster is reached.
- The mean latent space sample of each cluster was calculated and the distances between the clusters was extracted. Using the starting segment as the first point traversing the latent space to the next cluster mean that is closer to the end cluster than all previously considered cluster means until the final cluster is reached.

All of these methods were tested with various additional parameters, as well as additional manual decisions (Figure 5.1D) and often leading to understandable chains of results but not necessarily resulting in convincing sequences that would make sense for vesicle formation. The main problem is the restriction of the input segments being the same length. When searching for changes in membrane shapes

the membrane regions of interest increase or decrease in size over time. An example for this would be a budding vesicle for which the starting region of interest is a small bump in the membrane which increases over time until the bump separates from the original vesicle. While the method using VAE finds very similar membrane segments it can only find membrane segments of the same length due the restriction of the input shape. While there might be solutions for this problem as discussed in 5.3, the method was not pursued further as another method was found to be more promising.

5.2.2 Semi-automated construction of timelines using DTW

As a semi-automated method that is not based on autoencoders we aim to leverage the ability to search for subsequences in larger sequences using dynamic time warping. Using the segmentation and output of CryoVia it is possible to find a fitting membrane morphology time line by presenting the user with some well fitting membrane segments to the previously selected segments.

As a first step, a starting membrane object has to be selected. From this object a specific segment is extracted that the user is interested in. After the selection of the segment, dynamic time warp subsequence search (Meert et al., 2020) is calculated for all available vesicles, using the selected segment as the subsequence to search for. Although the user selects a specific segment of the membrane shape, the dynamic time warping algorithm works with the corresponding curvature segment instead of the actual coordinates. By using the curvature the shapes do not have to be rotated and normalized to be able to be compared which would produce various problems depending on the methods used and shapes in the dataset. It also reduces the computational resources by reducing the dynamic time warping algorithm to a 1D problem instead of 2D. After performing the parallelized subsequence search across all available membranes, the membranes are sorted by the resulting distance measurements and are displayed with the corresponding segment highlighted for

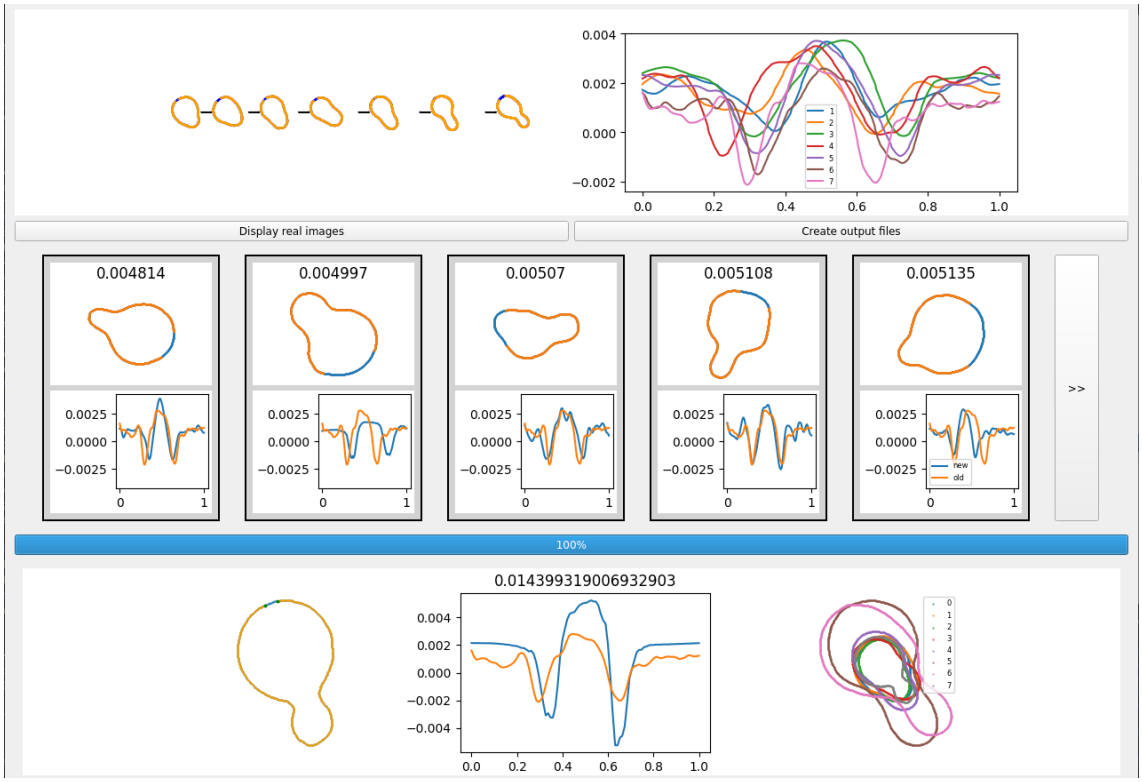

FIGURE 5.2: Example section of the graphical user interface used to create the membrane segment timelines. In the top left the previously selected membrane contours can be seen with orange indicating the part of the segment to actually use as a query segment. In the top right are the overlayed curvature values of all previously selected membrane segments. The middle section shows a selection of the best fitting next membrane segments considering the last selected segment. The bottom shows the currently selected membrane segment on the left. In the middle it has an overlay of the curvature value of the currently selected segment and the last selected segment and on the right is an overlay of all previously selected membranes. The selected segment (orange) of a membrane on the left can be manually adjusted.

the user to see. The segments with the lowest distance scores are presented to the user and the next segment in the time line can now be selected. At this step small adjustments to the found subsequence can be made for the next iteration of subsequence searches.

Using this method a membrane morphology time line can be established by selecting a membrane segment as a starting point and finding similar segments at each step.

Various parameters can be adjusted to fit the needs of specific use cases:

- Penalty: This parameter adjusts the dynamic time warping penalty for warping the sequence. It can be used to adjust the similarity of the membrane segments. If some parts of the segments are allowed to be warped to be stretched or compressed a small penalty is sensible but if the overall shape should stay the same a higher penalty should be used.

- Curvature scaling: This parameter rescales the curvature values of all membranes to better fit the subsequence curvature values. It can only be used when comparing subsequences in closed vesicles because a closed shape is necessary for the scaling. Three different types of curvature scaling are available.

  - Circumference: The ratio between the circumference of the vesicle from the selected segment and all other circumferences is calculated and the curvature values are scaled accordingly.

  - Area: The ratio between the area of the vesicle from the selected segment and all other areas is calculated and the curvature values are scaled accordingly.

  - Convex hull area: The ratio between the area of the convex hull of the vesicle from the selected segment and all other convex hull areas is calculated and the curvature values are scaled accordingly. This type of scaling can be used when working with vesicles with concave elements.

- Scaling contour: This parameter resamples membranes to have the same amount of curvature values. It can be used when working with a high variety in vesicle sizes while only the overall shape is of interest.

- Find similar percentage: This parameter forces the subsequence found in the searched membrane to be of a similar percentage as the selected segment. If the selected segment composes 50% of its membrane the found subsequence will also comprise a similar percentage of their corresponding membranes.

- Consider previous segments: This parameter helps to create the correct order in membrane morphology changes automatically. When this parameter is used found subsequences will be not only compared with the currently selected segment but also all previously selected segments. If any of the previously selected segments has a lower distance value with this newly found subsequence than the last selected segment, the method will not consider this as a viable next step.

To further automate this method it is also possible to set the algorithm to take the best fitting segment at every iteration and continue without manual intervention for a specified number of iterations. Unwanted steps can subsequently be removed. To efficiently use this method it is necessary to use the "Consider previous segments" parameter to find any kind of direction for the morphology changes because without activating the parameter the method will find only similar segments without any direction in between iterations.

Another method to reduce the manual interaction can be used by setting a starting and an end segment. Steps in between will be filled by searching for subsequences similar to both segments and sorting the resulting subsequences. The found subsequences are sorted by the weighted distance to both selected segments while starting with a weight of 1 for the distance to the starting segment and a weight of 0.1 for the distance to the end segment. At every step the weight is shifted more towards the distance to the end segment until the values are completely reversed. If enough time steps are present in the dataset between the start and end segment this method will find a adequate step by step progression in the membrane morphology. As a prove of concept a combination of various datasets of vesicles is used as an example input. The micrographs are segmented and classified into shape classes by CryoVIA. The vesicles are filtered so that only *stomatocytes*, *pears* and *elongated pears* remain (Figure 3.6). The reduction is an optional step but increases the speed of the calculations and helps quickly finding good starting and end shapes. To

show the effectiveness of this method a timeline for inward (Figure 5.3) as well as outward budding or tubulation (Figure 5.4) is created.

5.3 Discussion

I introduced two method to automatically find reasonable time steps of membrane remodeling in cryoEM micrographs. The first method is based on training an VAE on the curvature values of membrane segment, clustering the latent space and using the latent space clusters find good connections between paths. The second method is based on the subsequence search of DTW and provides a semi-automated way to guide a user through membrane segments.

The VAE is able to create a latent space in which similar encoded curvature segments are close to each and the original segments are able to be decoded as well. Because a variational autoencoder encoder was used it is also possible to new create curvature segments by sampling the latent space. Because the latent space is well structured, clustering algorithms result in good clusters with very similar curvature segments. Creating useful connections between these clusters was more difficult because there is not guarantee that close clusters in the latent space create reasonable time steps. While the clusters close to each other are often similar, a path from on a starting cluster to an end cluster is not necessarily logical. The segment extraction is also a reason why this method falls short in creating good timelines because it always extract segments of the same length for consistent input for the VAE. It also extracts overlapping segments of the same vesicles to include as many different segment shapes as possible, but this can also lead to a latent space in which the overlapping segments are very close to each other because they are partially the same segment which is not wanted.

While this method is not working as intended, a few improvements could lead to better, more usable results. The segment extraction method could also extract segments of various lengths and interpolating these segments to the same input

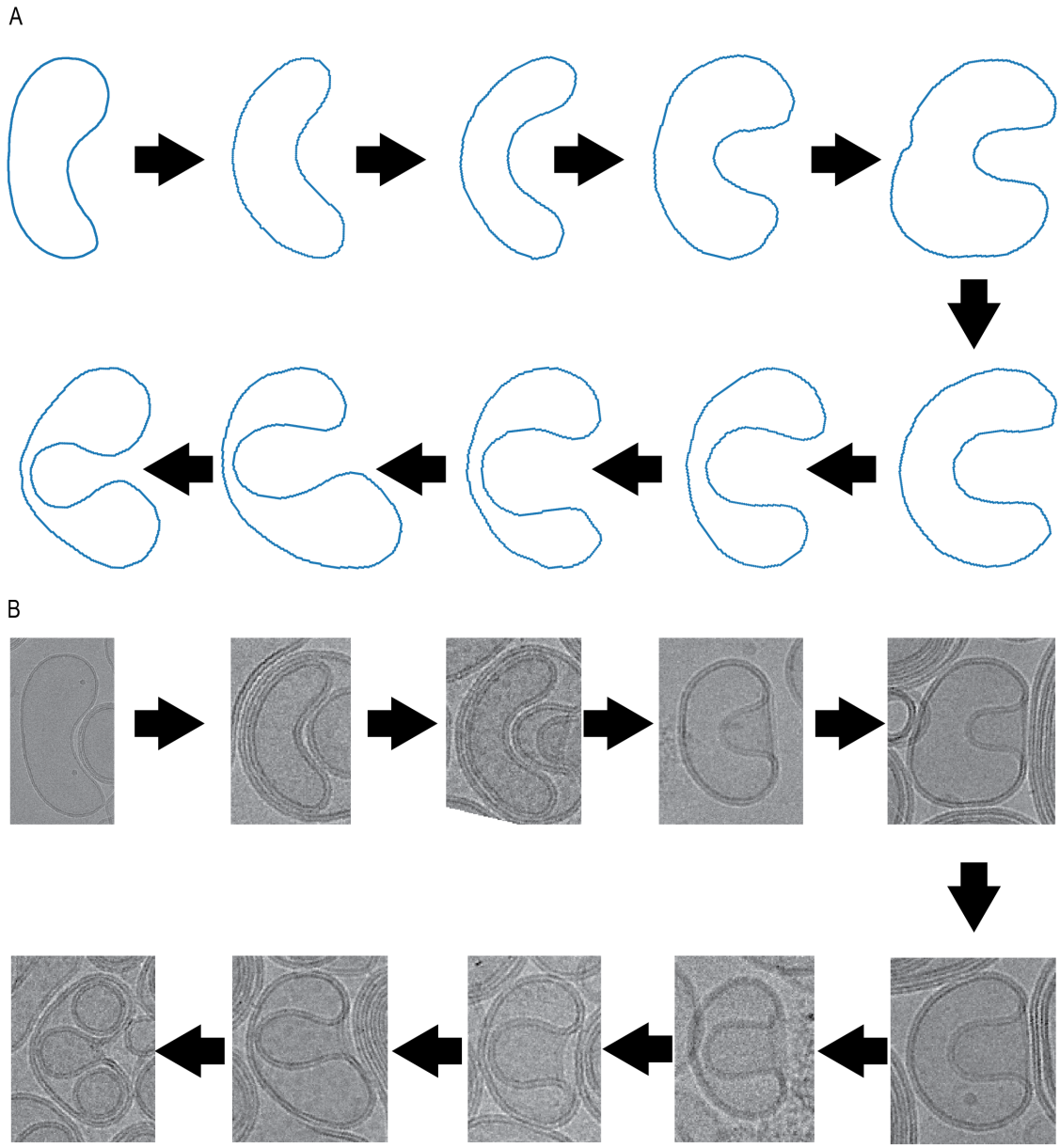

FIGURE 5.3: Example timeline for inward budding. (A) Vesicle contour of the vesicles in the timeline. (B) Cropped micrographs of the vesicles in the timeline.

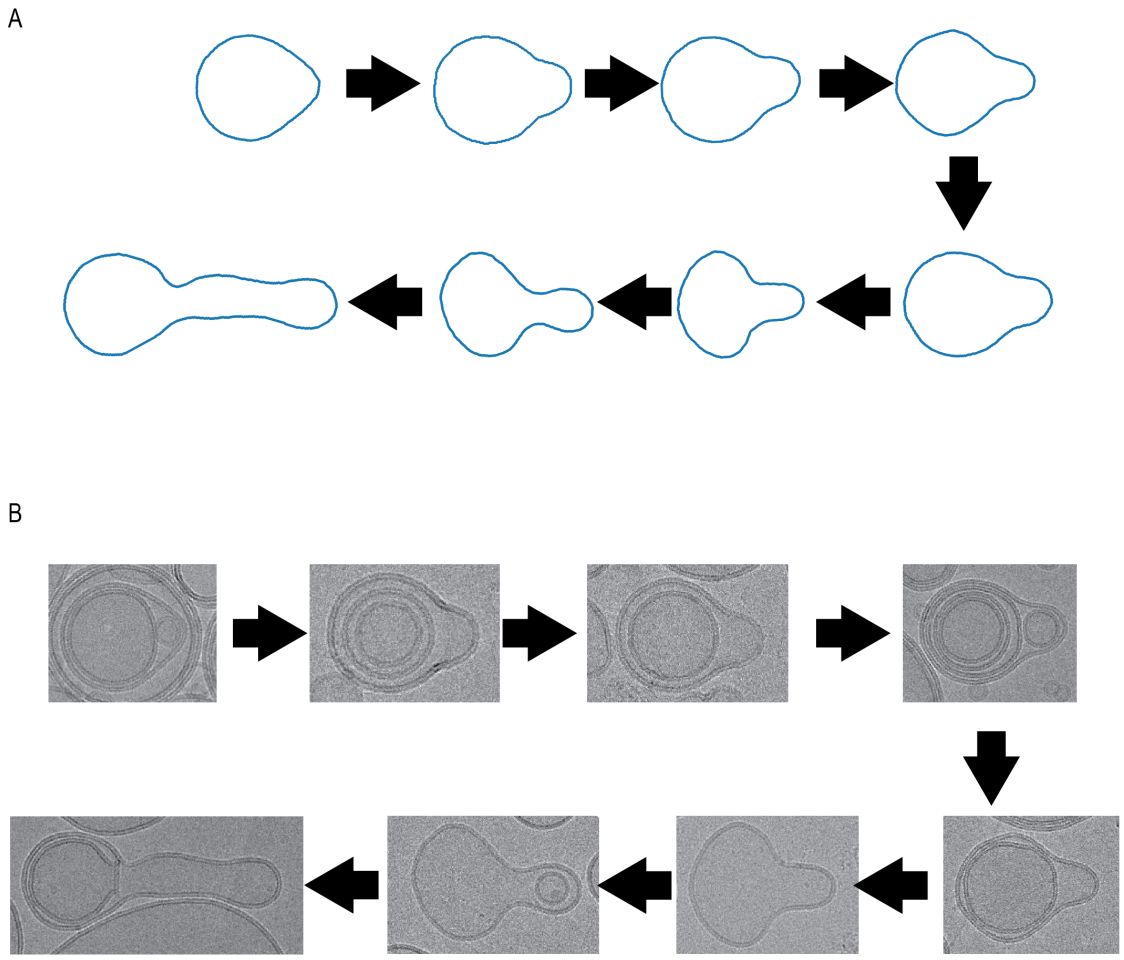

FIGURE 5.4: Example timeline for outward budding or tubulation. (A) Vesicle contour of the vesicles in the timeline. (B) Cropped micrographs of the vesicles in the timeline.

shape for the VAE. While this was tried for a short time, it was not extensively studied and potential improved of the method is possible. Another improvement could be an additional regulation function for the latent space creation (Gabdullin, 2024). It is feasible to use for example some sort of distance measurement like DTW to regulate the latent space creation further to ensure that close clusters make more logical sense. DTW could also be used to analyse the result of the clustering combining these two methods but removing a lot of very similar segments by only using a cluster mean. Another idea is to analyse complete vesicles instead of just segments, but this introduces the problem of not having a clear starting index. This problem could potentially be solved by using circular CNNs (Schubert et al., 2019) which introduce a wrapping padding to convolution steps which can be used for periodic data. While there are a lot of areas for improvement, it is not clear if this would result in a usable method for the problem.

The second method shows to be more promising by already creating good timeline for membrane remodeling. A timeline for inward as well as outward budding could be easily created with minimal user input. The method is also adaptable by manual intervention and focusing on the membrane segment of interest. An important improvement over the method using VAE is the ability to use membrane segments of various lengths in the timeline creation as well as correct and improving the results during method usage. However there are still areas to improve the suggested method. Some of the scaling methods create unrealistic distance measurements when both small and giant vesicles can be found in the same dataset. Low curvature regions of the giant vesicles can be scaled and compared to areas of small vesicles to very high similarity measurements which do not hold up when analysed visually. The automated creations of timelines using the best next fitting segment can also be improved by testing various methods to determine the next selected segment for the timeline. While this method can be further improved it is already capable of creating reasonable timelines although only vesicles without environmental or protein interaction were used. To estimate the real usefulness of this method it has

to be used with a dataset where membrane remodeling is studied.

Chapter 6

Outlook

While CryoEM already enables the determination of high-resolution protein structures and provides deep insights into cellular processes, it remains a method under continuous development and innovation. Especially CryoET is still actively being developed and the improvements for imaging by better hardware and more sophisticated software enable faster data acquisition at higher resolutions. The growing number of high-resolution tomograms intensifies the need for more diverse and powerful analysis tools to reliably extract the wealth of information they contain. While software solutions such as *membrain* (Lamm et al., 2022), *surface morphometrics* (Barad et al., 2023), *Amira* (Stalling, Westerhoff, and Hege, 2012) and the thickness estimation method introduced in this thesis already exist for membrane analysis in tomograms, future increases in resolution will drive the development of even more advanced tools. As lipid bilayers become more clearly resolved in tomograms, techniques currently used in 2D micrographs for bilayer thickness estimation will become applicable in 3D as well. A specialised software platform that consolidates various membrane analysis methods into a unified framework could prove highly beneficial and is already partially done by *membrain* (Lamm et al., 2022). Such a tool might incorporate segmentation, bilayer structure analysis, membrane protein identification and extraction (based on features such as curvature, thickness or local interactions), 3D shape comparison across datasets, and mapping of membrane structure distributions. Given the pace of recent advancements in the field, these analysis opportunities appear to be achievable in the near future.

Even with the increase of resolution in tomograms, a high-quality single micrograph will generally offer higher resolution due to the constraints imposed by the limited electron dose in tomography (Grant and Grigorieff, 2015, Lucas et al., 2022). It will therefore always be viable and necessary to include 2D images when analysing membranes due to some information only being present at very high resolutions. At the same time, enhancements in microscope hardware and software are enabling the acquisition of large datasets more rapidly, increasing the value of software tools capable of analysing large volumes of micrographs efficiently. While CryoVIA already facilitates the analysis of membrane-containing datasets, further development is both possible and necessary. It is feasible to integrate membrane analysis with SPA or STA to pick particles in close proximity to membranes or only at spots where the membrane shows specific characteristics (Nygaard, Kim, and Mancia, 2020, Yan et al., 2025, Pyle, Hutchings, and Zanetti, 2022). Another option for an interesting interaction with SPA would be to only include particles found inside specific organelles which could for example be defined by their shapes and size. This could lead to reconstructions of organelle-specific protein structures. While various publications have already extracted membrane thickness from micrographs (Heberle et al., 2020, Heberle et al., 2023. Sharma, Heberle, and Waxham, 2023, Tahara and Fujiyoshi, 1994), a possible advancements in the field could be to estimate the lipid distribution across the membrane structure. This could be achieved by either fitting observed densities to established models or train a neural network on synthetic data generated by molecular dynamics simulations. This could enhance our knowledge and understanding of membrane structures and their effect in the cellular environment.

New methods of sample preparation also open the door to innovative approaches for time-resolved CryoEM. One such concept might involve automating the addition of interaction agents to biological samples, depositing them on grids and vitrifying them at defined time intervals (Lu et al., 2009) or after activating interactions through outside stimuli (Ménétret et al., 1991). A specifically designed laboratory

robot could potentially automate this process (Gemin et al., 2024). This would enable the capture of structural snapshots at different stages of dynamic biological processes, provided that appropriate analysis tools, like the proposed method using DTW, are developed to interpret the resulting data.

In conclusion, CryoEM remains a rapidly advancing field. Continuous improvements in microscope technology, data acquisition strategies and analytical software are not only increasing the quantity of available structural data but also enhancing its quality. The improvements in tomogram resolutions and acquisition speed specifically, will provide many more biological insights in the near future.

Bibliography

Aden, Saša, Tina Snoj, and Gregor Anderluh (2021). “The use of giant unilamellar vesicles to study functional properties of pore-forming toxins”. In: *Methods in Enzymology*. Vol. 649. Elsevier, pp. 219–251. ISBN: 978-0-12-823858-5. DOI: 10.1016/bs.mie.2021.01.016. URL: https://linkinghub.elsevier.com/retrieve/pii/S0076687921000380 (visited on 01/29/2025).

Adrian, Marc, Jacques Dubochet, Jean Lepault, and Alasdair W. McDowall (Mar. 1984). “Cryo-electron microscopy of viruses”. In: *Nature* 308.5954, pp. 32–36. ISSN: 0028-0836, 1476-4687. DOI: 10.1038/308032a0. URL: https://www.nature.com/articles/308032a0 (visited on 01/30/2025).

Ahlers, Jannis, Daniel Althviz Moré, Oren Amsalem, Ashley Anderson, Grzegorz Bokota, Peter Boone, Jordão Bragantini, Genevieve Buckley, Alister Burt, Matthias Bussonnier, Ahmet Can Solak, Clément Caporal, Draga Doncila Pop, Kira Evans, Jeremy Freeman, Lorenzo Gaifas, Christoph Gohlke, Kabilar Gunalan, Hagai Har-Gil, Mark Harfouche, Kyle I. S. Harrington, Volker Hilsenstein, Katherine Hutchings, Talley Lambert, Jessy Lauer, Gregor Lichtner, Ziyang Liu, Lucy Liu, Alan Lowe, Luca Marconato, Sean Martin, Abigail McGovern, Lukasz Migas, Nadalyn Miller, Hector Muñoz, Jan-Hendrik Müller, Christopher Nauroth-Kreß, Juan Nunez-Iglesias, Constantin Pape, Kim Pevey, Gonzalo Peña-Castellanos, Andrea Pierré, Jaime Rodríguez-Guerra, David Ross, Loic Royer, Craig T. Russell, Gabriel Selzer, Paul Smith, Peter Sobolewski, Konstantin Sofiiuk, Nicholas Sofroniew, David Stansby, Andrew Sweet, Wouter-Michiel Vierdag, Pam Wadhwa, Melissa Weber Mendonça, Jonas Windhager, Philip Winston, and Kevin

Yamauchi (2023). *Napari: A Multi-Dimensional Image Viewer for Python*. DOI: 10.5281/ZENODO.3555620.

Attwood, Simon, Youngjik Choi, and Zoya Leonenko (Feb. 6, 2013). "Preparation of DOPC and DPPC Supported Planar Lipid Bilayers for Atomic Force Microscopy and Atomic Force Spectroscopy". In: *International Journal of Molecular Sciences* 14.2, pp. 3514–3539. ISSN: 1422-0067. DOI: 10.3390/ijms14023514. URL: https://www.mdpi.com/1422-0067/14/2/3514 (visited on 02/07/2025).

Baker, Lindsay A. and John L. Rubinstein (2010). "Radiation Damage in Electron Cryomicroscopy". In: *Methods in Enzymology*. Vol. 481. Elsevier, pp. 371–388. ISBN: 978-0-12-374906-2. DOI: 10.1016/S0076-6879(10)81015-8. URL: https://linkinghub.elsevier.com/retrieve/pii/S0076687910810158 (visited on 02/05/2025).

Ballard, Dana H. (1987). "Modular Learning in Neural Networks". In: *AAAI Conference on Artificial Intelligence*. URL: https://api.semanticscholar.org/CorpusID:38968420.

Barad, Benjamin A., Michaela Medina, Daniel Fuentes, R. Luke Wiseman, and Danielle A. Grotjahn (Feb. 2023). "Quantifying Organellar Ultrastructure in Cryo-Electron Tomography Using a Surface Morphometrics Pipeline". In: *Journal of Cell Biology* 222.4. Publisher: Rockefeller University Press. ISSN: 1540-8140. DOI: 10.1083/jcb.202204093.

Berndsen, Zachary, Charles Bowman, Haerin Jang, and Andrew B. Ward (Dec. 1, 2017). "EMHP: an accurate automated hole masking algorithm for single-particle cryo-EM image processing". In: *Bioinformatics (Oxford, England)* 33.23, pp. 3824–3826. ISSN: 1367-4811. DOI: 10.1093/bioinformatics/btx500.

Bhatia, Tripta, Peter Husen, Jonathan Brewer, Luis A. Bagatolli, Per L. Hansen, John H. Ipsen, and Ole G. Mouritsen (Dec. 2015). "Preparing giant unilamellar vesicles (GUVs) of complex lipid mixtures on demand: Mixing small unilamellar vesicles of compositionally heterogeneous mixtures". In: *Biochimica et Biophysica Acta (BBA) - Biomembranes* 1848.12, pp. 3175–3180. ISSN: 00052736.

DOI: 10.1016/j.bbamem.2015.09.020. URL: https://linkinghub.elsevier.com/retrieve/pii/S0005273615003053 (visited on 01/29/2025).

Binder, Hans and Klaus Gawrisch (Dec. 1, 2001). "Effect of Unsaturated Lipid Chains on Dimensions, Molecular Order and Hydration of Membranes". In: *The Journal of Physical Chemistry B* 105.49, pp. 12378–12390. ISSN: 1520-6106, 1520-5207. DOI: 10.1021/jp010118h. URL: https://pubs.acs.org/doi/10.1021/jp010118h (visited on 02/06/2025).

Botella, César, Emeline Sautron, Laurence Boudiere, Morgane Michaud, Emmanuelle Dubots, Yoshiki Yamaryo-Botté, Catherine Albrieux, Eric Marechal, Maryse A. Block, and Juliette Jouhet (Mar. 2016). "ALA10, a Phospholipid Flippase, Controls FAD2/FAD3 Desaturation of Phosphatidylcholine in the ER and Affects Chloroplast Lipid Composition in *Arabidopsis thaliana*". In: *Plant Physiology* 170.3, pp. 1300–1314. ISSN: 0032-0889, 1532-2548. DOI: 10.1104/pp.15.01557. URL: https://academic.oup.com/plphys/article/170/3/1300-1314/6114071 (visited on 01/29/2025).

Brémaud, Erwan, Cyril Favard, and Delphine Muriaux (Apr. 19, 2022). "Deciphering the Assembly of Enveloped Viruses Using Model Lipid Membranes". In: *Membranes* 12.5, p. 441. ISSN: 2077-0375. DOI: 10.3390/membranes12050441. URL: https://www.mdpi.com/2077-0375/12/5/441 (visited on 01/29/2025).

Buchholz, Tim-Oliver, Mareike Jordan, Gaia Pigino, and Florian Jug (Apr. 2019). "Cryo-CARE: Content-Aware Image Restoration for Cryo-Transmission Electron Microscopy Data". In: *2019 IEEE 16th International Symposium on Biomedical Imaging (ISBI 2019)*. 2019 IEEE 16th International Symposium on Biomedical Imaging (ISBI). Venice, Italy: IEEE, pp. 502–506. ISBN: 978-1-5386-3641-1. DOI: 10.1109/ISBI.2019.8759519. URL: https://ieeexplore.ieee.org/document/8759519/ (visited on 02/04/2025).

Campello, Ricardo J. G. B., Davoud Moulavi, and Joerg Sander (2013). "Density-Based Clustering Based on Hierarchical Density Estimates". In: *Advances in Knowledge Discovery and Data Mining*. Ed. by Jian Pei, Vincent S. Tseng, Longbing Cao,

Hiroshi Motoda, and Guandong Xu. Berlin, Heidelberg: Springer Berlin Heidelberg, pp. 160–172. ISBN: 978-3-642-37456-2.

Carter, C. Barry and David B. Williams, eds. (2016). *Transmission Electron Microscopy: Diffraction, Imaging, and Spectrometry*. SpringerLink Bücher. Cham: Springer. 518 pp. ISBN: 978-3-319-26649-7 978-3-319-26651-0. DOI: 10.1007/978-3-319-26651-0.

Casares, Doralicia, Pablo V. Escribá, and Catalina Ana Rosselló (May 1, 2019). "Membrane Lipid Composition: Effect on Membrane and Organelle Structure, Function and Compartmentalization and Therapeutic Avenues". In: *International Journal of Molecular Sciences* 20.9, p. 2167. ISSN: 1422-0067. DOI: 10.3390/ijms20092167. URL: https://www.mdpi.com/1422-0067/20/9/2167 (visited on 01/29/2025).

Chapman, D. (Feb. 1, 1987). "Handbook of Lipid Research, Volume 4: The Physical Chemistry of Lipids". In: *Biochemical Society Transactions* 15.1, pp. 184–185. ISSN: 0300-5127, 1470-8752. DOI: 10.1042/bst0150184a. URL: https://portlandpress.com/biochemsoctrans/article/15/1/184/59294/Handbook-of-Lipid-Research-Volume-4-The-Physical (visited on 01/29/2025).

Chemaxon (Feb. 7, 2025). *Marvin for JavaScript*. Version 24.3.0.

Cheng, Anchi, Paul T. Kim, Huihui Kuang, Joshua H. Mendez, Eugene Y. D. Chua, Kashyap Maruthi, Hui Wei, Anjelique Sawh, Mahira F. Aragon, Viacheslav Serbynovskyi, Kasahun Neselu, Edward T. Eng, Clinton S. Potter, Bridget Carragher, Tristan Bepler, and Alex J. Noble (Jan. 1, 2023). "Fully automated multi-grid cryoEM screening using Smart Leginon". In: *IUCrJ* 10 (Pt 1), pp. 77–89. ISSN: 2052-2525. DOI: 10.1107/S2052252522010624.

Cooper, Geoffrey M. (2000). *The cell: a molecular approach*. 2nd ed. Washington, D.C. Sunderland, Mass: ASM Press. 1 p. ISBN: 978-0-87893-106-4.

Coupland, Claire E., Ryan Karimi, Stephanie A. Bueler, Yingke Liang, Gautier M. Courbon, Justin M. Di Trani, Cassandra J. Wong, Rayan Saghian, Ji-Young Youn,

Lu-Yang Wang, and John L. Rubinstein (2024). "High resolution cryo-EM of V-ATPase in native synaptic vesicles". In: *bioRxiv*. DOI: 10.1101/2024.04.01.587493. URL: https://www.biorxiv.org/content/early/2024/04/01/2024.04.01.587493.

Crowther, Richard, DeRosier, and Aaron Klug (June 23, 1970). "The reconstruction of a three-dimensional structure from projections and its application to electron microscopy". In: *Proceedings of the Royal Society of London. A. Mathematical and Physical Sciences* 317.1530, pp. 319–340. ISSN: 0080-4630. DOI: 10.1098/rspa.1970.0119. URL: https://royalsocietypublishing.org/doi/10.1098/rspa.1970.0119 (visited on 01/31/2025).

Dalton, Amanda K., Danso Ako-Adjei, Paul S. Murray, Diana Murray, and Volker M. Vogt (June 15, 2007). "Electrostatic Interactions Drive Membrane Association of the Human Immunodeficiency Virus Type 1 Gag MA Domain". In: *Journal of Virology* 81.12, pp. 6434–6445. ISSN: 0022-538X, 1098-5514. DOI: 10.1128/JVI.02757-06. URL: https://journals.asm.org/doi/10.1128/JVI.02757-06 (visited on 01/29/2025).

Darwin, Andrew J. (Aug. 2005). "The phage-shock-protein response". In: *Molecular Microbiology* 57.3, pp. 621–628. ISSN: 0950-382X, 1365-2958. DOI: 10.1111/j.1365-2958.2005.04694.x. URL: https://onlinelibrary.wiley.com/doi/10.1111/j.1365-2958.2005.04694.x (visited on 01/29/2025).

Daumke, Oliver, Aurélien Roux, and Volker Haucke (Feb. 2014). "BAR Domain Scaffolds in Dynamin-Mediated Membrane Fission". In: *Cell* 156.5. Publisher: Elsevier BV, pp. 882–892. ISSN: 0092-8674. DOI: 10.1016/j.cell.2014.02.017.

Desfosses, Ambroise, Rodolfo Ciuffa, Irina Gutsche, and Carsten Sachse (Jan. 2014). "SPRING – an Image Processing Package for Single-Particle Based Helical Reconstruction from Electron Cryomicrographs". In: *Journal of Structural Biology* 185.1. Publisher: Elsevier BV, pp. 15–26. ISSN: 1047-8477. DOI: 10.1016/j.jsb.2013.11.003.

Diaz, Ruben, J. Rice William, and David L. Stokes (2010). “Fourier–Bessel Reconstruction of Helical Assemblies”. In: *Cryo-EM, part b: 3-d reconstruction*. ISSN: 0076-6879. Elsevier, pp. 131–165. DOI: 10.1016/s0076-6879(10)82005-1.

Dimova, Rumiana and Carlos M. Marques, eds. (2022). *The giant vesicle book*. First issued in paperback. Boca Raton London New York: CRC Press, Taylor & Francis Group. 652 pp. ISBN: 978-1-03-233789-0 978-1-4987-5217-6.

Döbereiner, Hans-Günther (July 2000). “Properties of Giant Vesicles”. In: *Current Opinion in Colloid & Interface Science* 5.3. Publisher: Elsevier BV, pp. 256–263. ISSN: 1359-0294. DOI: 10.1016/s1359-0294(00)00064-9.

“Let’s talk about lipid nanoparticles” (Feb. 9, 2021). In: *Nature Reviews Materials* 6.2. Ed. by Editorial, pp. 99–99. ISSN: 2058-8437. DOI: 10.1038/s41578-021-00281-4. URL: https://www.nature.com/articles/s41578-021-00281-4 (visited on 01/31/2025).

Egelman, Edward H. (Jan. 2007). “The Iterative Helical Real Space Reconstruction Method: Surmounting the Problems Posed by Real Polymers”. In: *Journal of Structural Biology* 157.1. Publisher: Elsevier BV, pp. 83–94. ISSN: 1047-8477. DOI: 10.1016/j.jsb.2006.05.015.

Ester, Martin, Hans-Peter Kriegel, Jörg Sander, and Xiaowei Xu (1996). “A density-based algorithm for discovering clusters in large spatial databases with noise”. In: *Proceedings of the Second International Conference on Knowledge Discovery and Data Mining*. KDD’96. Place: Portland, Oregon. AAAI Press, pp. 226–231.

Flores-Kim, Josué and Andrew J. Darwin (Sept. 8, 2016). “The Phage Shock Protein Response”. In: *Annual Review of Microbiology* 70.1, pp. 83–101. ISSN: 0066-4227, 1545-3251. DOI: 10.1146/annurev-micro-102215-095359. URL: https://www.annualreviews.org/doi/10.1146/annurev-micro-102215-095359 (visited on 01/29/2025).

Frangi, Alejandro F., Wiro J. Niessen, Koen L. Vincken, and Max A. Viergever (1998). “Multiscale vessel enhancement filtering”. In: *Medical Image Computing and Computer-Assisted Intervention — MICCAI’98*. Ed. by William M. Wells, Alan

Colchester, and Scott Delp. Vol. 1496. Series Title: Lecture Notes in Computer Science. Berlin, Heidelberg: Springer Berlin Heidelberg, pp. 130–137. ISBN: 978-3-540-65136-9 978-3-540-49563-5. DOI: 10.1007/BFb0056195. URL: http://link.springer.com/10.1007/BFb0056195 (visited on 05/23/2024).

Freytag, J. William (Jan. 1985). "Large unilamellar lipid vesicles for use in therapeutic and diagnostic medicine". In: *Journal of Microencapsulation* 2.1, pp. 31–38. ISSN: 0265-2048, 1464-5246. DOI: 10.3109/02652048509049575. URL: http://www.tandfonline.com/doi/full/10.3109/02652048509049575 (visited on 01/29/2025).

Frost, Adam, Rushika Perera, Aurélien Roux, Krasimir Spasov, Olivier Destaing, Edward H. Egelman, Pietro De Camilli, and Vinzenz M. Unger (Mar. 2008). "Structural Basis of Membrane Invagination by f-BAR Domains". In: *Cell* 132.5. Publisher: Elsevier BV, pp. 807–817. ISSN: 0092-8674. DOI: 10.1016/j.cell.2007.12.041.

Gabdullin, Nikita (2024). *Latent space configuration for improved generalization in supervised autoencoder neural networks*. Version Number: 2. DOI: 10.48550/ARXIV.2402.08441. URL: https://arxiv.org/abs/2402.08441 (visited on 02/12/2025).

Gemin, Olivier, Victor Armijo, Michael Hons, Caroline Bissardon, Romain Linares, Matthew W. Bowler, Georg Wolff, Kirill Kovalev, Anastasiia Babenko, Veijo T. Salo, Sarah Schneider, Christopher Rossi, Léa Lecomte, Thibault Deckers, Kévin Lauzier, Robert Janocha, Franck Felisaz, Jérémy Sinoir, Wojciech Galej, Julia Mahamid, Christoph W. Müller, Sebastian Eustermann, Simone Mattei, Florent Cipriani, and Gergely Papp (Jan. 20, 2024). *EasyGrid: a versatile platform for automated cryo-EM sample preparation and quality control*. DOI: 10.1101/2024.01.18.576170. URL: http://biorxiv.org/lookup/doi/10.1101/2024.01.18.576170 (visited on 05/12/2025).

Gennis, Robert B. (1989). *Biomembranes: Molecular Structure and Function*. Red. by Charles R. Cantor. Springer Advanced Texts in Chemistry. New York, NY:

Springer New York. ISBN: 978-1-4757-2067-9 978-1-4757-2065-5. DOI: 10.1007/978-1-4757-2065-5. URL: http://link.springer.com/10.1007/978-1-4757-2065-5 (visited on 01/29/2025).

Giménez-Andrés, Manuel, Alenka Čopič, and Bruno Antonny (July 5, 2018). "The Many Faces of Amphipathic Helices". In: *Biomolecules* 8.3, p. 45. ISSN: 2218-273X. DOI: 10.3390/biom8030045. URL: https://www.mdpi.com/2218-273X/8/3/45 (visited on 02/07/2025).

Gonzalez, Rafael C. and Richard E. Woods (2008). *Digital image processing*. 3. ed., internat. ed. Pearson education. Upper Saddle River, NJ: Pearson Education Internat. 954 pp. ISBN: 978-0-13-505267-9.

Goodfellow, Ian, Aaron Courville, and Yoshua Bengio (2016). *Deep learning*. Adaptive computation and machine learning. Cambridge, Massachusetts: The MIT Press. 1 p. ISBN: 978-0-262-03561-3 978-0-262-33737-3.

Grant, Timothy and Nikolaus Grigorieff (May 29, 2015). "Measuring the optimal exposure for single particle cryo-EM using a 2.6 Å reconstruction of rotavirus VP6". In: *eLife* 4, e06980. ISSN: 2050-084X. DOI: 10.7554/eLife.06980. URL: https://elifesciences.org/articles/06980 (visited on 05/12/2025).

Grzejszczak, Tomasz, Eryka Probierz, Adam Galuszka, Krzysztof Simek, Karol Jedrasiak, and Tomasz Wisniewski (Jan. 1, 2022). "Dynamic Time Warping in Financial Data – Modification of Algorithm in Context of Stock Market Similarity Analysis". In: *EUROPEAN RESEARCH STUDIES JOURNAL* XXV (Issue 1), pp. 967–979. ISSN: 1108-2976. DOI: 10.35808/ersj/2897. URL: https://ersj.eu/journal/2897 (visited on 02/13/2025).

Harayama, Takeshi and Howard Riezman (May 2018). "Understanding the diversity of membrane lipid composition". In: *Nature Reviews Molecular Cell Biology* 19.5, pp. 281–296. ISSN: 1471-0072, 1471-0080. DOI: 10.1038/nrm.2017.138. URL: https://www.nature.com/articles/nrm.2017.138 (visited on 01/29/2025).

He, Kaiming, Georgia Gkioxari, Piotr Dollár, and Ross Girshick (2017). *Mask R-CNN*. Version Number: 3. DOI: 10.48550/ARXIV.1703.06870. URL: https://arxiv.org/abs/1703.06870 (visited on 02/10/2025).

He, Shaoda and Sjors H. W. Scheres (June 2017). "Helical Reconstruction in RELION". In: *Journal of Structural Biology* 198.3. Publisher: Elsevier BV, pp. 163–176. ISSN: 1047-8477. DOI: 10.1016/j.jsb.2017.02.003.

Heberle, Frederick A., Milka Doktorova, Haden L. Scott, Allison D. Skinkle, M. Neal Waxham, and Ilya Levental (Aug. 2020). "Direct Label-Free Imaging of Nanodomains in Biomimetic and Biological Membranes by Cryogenic Electron Microscopy". In: *Proceedings of the National Academy of Sciences* 117.33. Publisher: Proceedings of the National Academy of Sciences, pp. 19943–19952. DOI: 10.1073/pnas.2002200117.

Heberle, Frederick A., Doug Welsch, Haden L. Scott, and M. Neal Waxham (Mar. 2023). "Optimization of Cryo-Electron Microscopy for Quantitative Analysis of Lipid Bilayers". In: *Biophysical Reports* 3.1. Publisher: Elsevier BV, p. 100090. DOI: 10.1016/j.bpr.2022.100090.

Herrmann, Matthieu and Geoffrey I. Webb (May 2023). "Amercing: An intuitive and effective constraint for dynamic time warping". In: *Pattern Recognition* 137, p. 109333. ISSN: 00313203. DOI: 10.1016/j.patcog.2023.109333. URL: https://linkinghub.elsevier.com/retrieve/pii/S0031320323000341 (visited on 01/29/2025).

Hokanson, David E. and E. Michael Ostap (Feb. 28, 2006). "Myo1c binds tightly and specifically to phosphatidylinositol 4,5-bisphosphate and inositol 1,4,5-trisphosphate". In: *Proceedings of the National Academy of Sciences* 103.9, pp. 3118–3123. ISSN: 0027-8424, 1091-6490. DOI: 10.1073/pnas.0505685103. URL: https://pnas.org/doi/full/10.1073/pnas.0505685103 (visited on 01/29/2025).

Holló, Gábor, Ylenia Miele, Federico Rossi, and István Lagzi (2021). "Shape changes and budding of giant vesicles induced by an internal chemical trigger: an interplay between osmosis and pH change". In: *Physical Chemistry Chemical Physics*

23.7, pp. 4262–4270. ISSN: 1463-9076, 1463-9084. DOI: 10.1039/D0CP05952H. URL: https://xlink.rsc.org/?DOI=D0CP05952H (visited on 02/07/2025).

Jensen, Grant J. (2010). *Cryo-EM*. 1st ed. Methods in enzymology v. 481. Amsterdam Boston: Academic. ISBN: 978-0-12-374906-2.

Jiang, Yihang, Yuankai Qi, Will Ke Wang, Brinnae Bent, Robert Avram, Jeffrey Olgin, and Jessilyn Dunn (May 9, 2020). "EventDTW: An Improved Dynamic Time Warping Algorithm for Aligning Biomedical Signals of Nonuniform Sampling Frequencies". In: *Sensors* 20.9, p. 2700. ISSN: 1424-8220. DOI: 10.3390/s20092700. URL: https://www.mdpi.com/1424-8220/20/9/2700 (visited on 02/13/2025).

Jimah, John R. and Jenny E. Hinshaw (Mar. 2019). "Structural Insights into the Mechanism of Dynamin Superfamily Proteins". In: *Trends in Cell Biology* 29.3. Publisher: Elsevier BV, pp. 257–273. ISSN: 0962-8924. DOI: 10.1016/j.tcb.2018.11.003.

Joly, Nicolas, Christoph Engl, Goran Jovanovic, Maxime Huvet, Tina Toni, Xia Sheng, Michael P.H. Stumpf, and Martin Buck (Sept. 2010). "Managing membrane stress: the phage shock protein (Psp) response, from molecular mechanisms to physiology". In: *FEMS Microbiology Reviews* 34.5, pp. 797–827. ISSN: 1574-6976. DOI: 10.1111/j.1574-6976.2010.00240.x. URL: https://academic.oup.com/femsre/article-lookup/doi/10.1111/j.1574-6976.2010.00240.x (visited on 01/29/2025).

Jovanovic, Goran, Parul Mehta, Christopher McDonald, Anthony C. Davidson, Povilas Uzdavinys, Liming Ying, and Martin Buck (Apr. 2014). "The N-Terminal Amphipathic Helices Determine Regulatory and Effector Functions of Phage Shock Protein A (PspA) in Escherichia coli". In: *Journal of Molecular Biology* 426.7, pp. 1498–1511. ISSN: 00222836. DOI: 10.1016/j.jmb.2013.12.016. URL: https://linkinghub.elsevier.com/retrieve/pii/S0022283613007821 (visited on 01/29/2025).

Junglas, Benedikt, Stefan T. Huber, Thomas Heidler, Lukas Schlösser, Daniel Mann, Raoul Hennig, Mairi Clarke, Nadja Hellmann, Dirk Schneider, and Carsten Sachse (July 2021). "PspA Adopts an ESCRT-III-like Fold and Remodels Bacterial Membranes". In: *Cell* 184.14. Publisher: Elsevier BV, 3674–3688.e18. ISSN: 0092-8674. DOI: 10.1016/j.cell.2021.05.042.

Junglas, Benedikt, Esther Hudina, Philipp Schönnenbeck, Ilona Ritter, Anja Heddier, Beatrix Santiago-Schübel, Pitter F. Huesgen, Dirk Schneider, and Carsten Sachse (Jan. 2025). "Structural plasticity of bacterial ESCRT-III protein PspA in higher-order assemblies". In: *Nature Structural & Molecular Biology* 32.1, pp. 23–34. ISSN: 1545-9993, 1545-9985. DOI: 10.1038/s41594-024-01359-7. URL: https://www.nature.com/articles/s41594-024-01359-7 (visited on 02/05/2025).

Karimi, Ryan, Claire E. Coupland, and John L. Rubinstein (Dec. 2024). "Vesicle Picker: A tool for efficient identification of membrane protein complexes in vesicles". In: *Journal of Structural Biology* 216.4, p. 108148. ISSN: 10478477. DOI: 10.1016/j.jsb.2024.108148. URL: https://linkinghub.elsevier.com/retrieve/pii/S1047847724000881 (visited on 01/30/2025).

Kausche, G. A., E. Pfankuch, and H. Ruska (May 1939). "Die Sichtbarmachung von pflanzlichem Virus im Übermikroskop". In: *Die Naturwissenschaften* 27.18, pp. 292–299. ISSN: 0028-1042, 1432-1904. DOI: 10.1007/BF01493353. URL: http://link.springer.com/10.1007/BF01493353 (visited on 02/05/2025).

Kazhdan, Michael and Hugues Hoppe (June 2013). "Screened poisson surface reconstruction". In: *ACM Transactions on Graphics* 32.3, pp. 1–13. ISSN: 0730-0301, 1557-7368. DOI: 10.1145/2487228.2487237. URL: https://dl.acm.org/doi/10.1145/2487228.2487237 (visited on 02/10/2025).

Kingma, Diederik and Jimmy Ba (Dec. 2014). "Adam: A Method for Stochastic Optimization". In: *International Conference on Learning Representations*.

Kingma, Diederik P and Max Welling (2013). *Auto-Encoding Variational Bayes*. Version Number: 11. DOI: 10.48550/ARXIV.1312.6114. URL: https://arxiv.org/abs/1312.6114 (visited on 01/29/2025).

Knoll, M. and E. Ruska (May 1932). "Das Elektronenmikroskop". In: *Zeitschrift für Physik* 78.5, pp. 318–339. ISSN: 1434-6001, 1434-601X. DOI: 10.1007/BF01342199. URL: http://link.springer.com/10.1007/BF01342199 (visited on 01/30/2025).

Koning, Roman I., Abraham J. Koster, and Thomas H. Sharp (May 2018). "Advances in cryo-electron tomography for biology and medicine". In: *Annals of Anatomy - Anatomischer Anzeiger* 217, pp. 82–96. ISSN: 09409602. DOI: 10.1016/j.aanat.2018.02.004. URL: https://linkinghub.elsevier.com/retrieve/pii/S0940960218300219 (visited on 01/31/2025).

Kühlbrandt, Werner (Mar. 28, 2014). "The Resolution Revolution". In: *Science* 343.6178, pp. 1443–1444. ISSN: 0036-8075, 1095-9203. DOI: 10.1126/science.1251652. URL: https://www.science.org/doi/10.1126/science.1251652 (visited on 02/06/2025).

Kühlbrandt, Werner (Feb. 2022). "Forty Years in cryoEM of Membrane Proteins". In: *Microscopy* 71 (Supplement_1). Publisher: Oxford University Press (OUP), pp. i30–i50. ISSN: 2050-5701. DOI: 10.1093/jmicro/dfab041.

Lagergren, John, Erica Rutter, and Kevin Flores (2020). *Region Growing with Convolutional Neural Networks for Biomedical Image Segmentation*. DOI: 10.48550/ARXIV.2009.11717.

Lamm, Lorenz, Ricardo D. Righetto, Wojciech Wietrzynski, Matthias Pöge, Antonio Martinez-Sanchez, Tingying Peng, and Benjamin D. Engel (Sept. 2022). "MemBrain: A Deep Learning-Aided Pipeline for Detection of Membrane Proteins in Cryo-Electron Tomograms". In: *Computer Methods and Programs in Biomedicine* 224. Publisher: Elsevier BV, p. 106990. ISSN: 0169-2607. DOI: 10.1016/j.cmpb.2022.106990.

Lee, T.C., R.L. Kashyap, and C.N. Chu (Nov. 1994). "Building Skeleton Models via 3-D Medial Surface Axis Thinning Algorithms". In: *CVGIP: Graphical Models and Image Processing* 56.6, pp. 462–478. ISSN: 10499652. DOI: 10.1006/cgip.1994.1042. URL: https://linkinghub.elsevier.com/retrieve/pii/S104996528471042X (visited on 01/31/2025).

Li, Yi, Xuan Feng, Yuanping Xu, Xude Dong, Zhijie Xu, Jian Huang, and Li Lu (Sept. 2019). "A Dynamic Hand Gesture Recognition Model Based on the Improved Dynamic Time Warping Algorithm". In: *2019 25th International Conference on Automation and Computing (ICAC)*. 2019 25th International Conference on Automation and Computing (ICAC). Lancaster, United Kingdom: IEEE, pp. 1–6. ISBN: 978-1-86137-665-7. DOI: 10.23919/IConAC.2019.8895002. URL: https://ieeexplore.ieee.org/document/8895002/ (visited on 02/13/2025).

Lijffijt, Jefrey, Panagiotis Papapetrou, Jaakko Hollmén, and Vassilis Athitsos (June 23, 2010). "Benchmarking dynamic time warping for music retrieval". In: *Proceedings of the 3rd International Conference on PErvasive Technologies Related to Assistive Environments*. PETRA '10: The 3rd International Conference on PErvasive Technologies Related to Assistive Environments. Samos Greece: ACM, pp. 1–7. ISBN: 978-1-4503-0071-1. DOI: 10.1145/1839294.1839365. URL: https://dl.acm.org/doi/10.1145/1839294.1839365 (visited on 02/13/2025).

Liu, Yun-Tao, Heng Zhang, Hui Wang, Chang-Lu Tao, Guo-Qiang Bi, and Z. Hong Zhou (Oct. 29, 2022). "Isotropic reconstruction for electron tomography with deep learning". In: *Nature Communications* 13.1, p. 6482. ISSN: 2041-1723. DOI: 10.1038/s41467-022-33957-8. URL: https://www.nature.com/articles/s41467-022-33957-8 (visited on 02/07/2025).

Lombardo, Domenico and Mikhail A. Kiselev (Feb. 28, 2022). "Methods of Liposomes Preparation: Formation and Control Factors of Versatile Nanocarriers for Biomedical and Nanomedicine Application". In: *Pharmaceutics* 14.3, p. 543.

ISSN: 1999-4923. DOI: 10.3390/pharmaceutics14030543. URL: https://www.mdpi.com/1999-4923/14/3/543 (visited on 01/29/2025).

Low, Harry H., Carsten Sachse, Linda A. Amos, and Jan Löwe (Dec. 2009). "Structure of a Bacterial Dynamin-Like Protein Lipid Tube Provides a Mechanism for Assembly and Membrane Curving". In: *Cell* 139.7. Publisher: Elsevier BV, pp. 1342–1352. ISSN: 0092-8674. DOI: 10.1016/j.cell.2009.11.003.

Lu, Zonghuan, Tanvir R. Shaikh, David Barnard, Xing Meng, Hisham Mohamed, Aymen Yassin, Carmen A. Mannella, Rajendra K. Agrawal, Toh-Ming Lu, and Terence Wagenknecht (Dec. 2009). "Monolithic microfluidic mixing–spraying devices for time-resolved cryo-electron microscopy". In: *Journal of Structural Biology* 168.3, pp. 388–395. ISSN: 10478477. DOI: 10.1016/j.jsb.2009.08.004. URL: https://linkinghub.elsevier.com/retrieve/pii/S1047847709002123 (visited on 05/12/2025).

Lucas, Bronwyn A, Kexin Zhang, Sarah Loerch, and Nikolaus Grigorieff (Aug. 2022). "In Situ Single Particle Classification Reveals Distinct 60S Maturation Intermediates in Cells". In: *eLife* 11. Publisher: eLife Sciences Publications, Ltd. ISSN: 2050-084X. DOI: 10.7554/elife.79272.

MacQueen, J. (1967). "Some methods for classification and analysis of multivariate observations". In: URL: https://api.semanticscholar.org/CorpusID:6278891.

Mandala, Venkata Shiva and Roderick MacKinnon (Nov. 15, 2022). "Voltage-sensor movements in the Eag Kv channel under an applied electric field". In: *Proceedings of the National Academy of Sciences* 119.46, e2214151119. ISSN: 0027-8424, 1091-6490. DOI: 10.1073/pnas.2214151119. URL: https://pnas.org/doi/10.1073/pnas.2214151119 (visited on 01/30/2025).

Martinez-Sanchez, Antonio, Inmaculada Garcia, Shoh Asano, Vladan Lucic, and Jose-Jesus Fernandez (Apr. 2014). "Robust Membrane Detection Based on Tensor Voting for Electron Tomography". In: *Journal of Structural Biology* 186.1. Publisher: Elsevier BV, pp. 49–61. DOI: 10.1016/j.jsb.2014.02.015.

Mastronarde, David N. and Susannah R. Held (Feb. 2017). "Automated tilt series alignment and tomographic reconstruction in IMOD". In: *Journal of Structural Biology* 197.2, pp. 102–113. ISSN: 10478477. DOI: 10.1016/j.jsb.2016.07.011. URL: https://linkinghub.elsevier.com/retrieve/pii/S1047847716301526 (visited on 02/07/2025).

McMahon, Harvey T. and Jennifer L. Gallop (Nov. 2005). "Membrane Curvature and Mechanisms of Dynamic Cell Membrane Remodelling". In: *Nature* 438.7068. Publisher: Springer Science; Business Media LLC, pp. 590–596. ISSN: 1476-4687. DOI: 10.1038/nature04396.

Meert, Wannes, Kilian Hendrickx, Toon Van Craenendonck, Pieter Robberechts, Hendrik Blockeel, and Jesse Davis (Aug. 11, 2020). *DTAIDistance*. Version v2.3.10. DOI: 10.5281/ZENODO.7158824. URL: https://zenodo.org/record/7158824 (visited on 02/05/2025).

Mitra, Kakoli, Iban Ubarretxena-Belandia, Tomohiko Taguchi, Graham Warren, and Donald M. Engelman (Mar. 23, 2004). "Modulation of the bilayer thickness of exocytic pathway membranes by membrane proteins rather than cholesterol". In: *Proceedings of the National Academy of Sciences* 101.12, pp. 4083–4088. ISSN: 0027-8424, 1091-6490. DOI: 10.1073/pnas.0307332101. URL: https://pnas.org/doi/full/10.1073/pnas.0307332101 (visited on 02/06/2025).

Moody, Michael F. (2011). *Structural biology using electrons and X-rays: an introduction for biologists*. 1st ed. Amsterdam Boston: Academic Press. ISBN: 978-0-12-370581-5.

Moss, Frank R., James Lincoff, Maxwell Tucker, Arshad Mohammed, Michael Grabe, and Adam Frost (Jan. 2023). "Brominated Lipid Probes Expose Structural Asymmetries in Constricted Membranes". In: *Nature Structural & Molecular Biology* 30.2. Publisher: Springer Science; Business Media LLC, pp. 167–175. ISSN: 1545-9985. DOI: 10.1038/s41594-022-00898-1.

Muntoni, Alessandro, jmespadero, Paolo Cignoni, Alberto Luaces, RichardScottOZ, luzpaz, and Fubin Zhang (Sept. 16, 2024). *cnr-isti-vclab/PyMeshLab: PyMeshLab*

v2023.12.post2. Version v2023.12.post2. DOI: 10.5281/ZENODO.13768931. URL: https://zenodo.org/doi/10.5281/zenodo.13768931 (visited on 02/10/2025).

Ménétret, J.-F., W. Hofmann, R.R. Schröder, G. Rapp, and R.S. Goody (May 1991). "Time-resolved cryo-electron microscopic study of the dissociation of actomyosin induced by photolysis of photolabile nucleotides". In: *Journal of Molecular Biology* 219.2, pp. 139–144. ISSN: 00222836. DOI: 10.1016/0022-2836(91)90554-J. URL: https://linkinghub.elsevier.com/retrieve/pii/002228369190554J (visited on 05/12/2025).

Needleman, Saul B. and Christian D. Wunsch (Mar. 1970). "A general method applicable to the search for similarities in the amino acid sequence of two proteins". In: *Journal of Molecular Biology* 48.3, pp. 443–453. ISSN: 00222836. DOI: 10.1016/0022-2836(70)90057-4. URL: https://linkinghub.elsevier.com/retrieve/pii/0022283670900574 (visited on 01/29/2025).

Nizamudeen, Zubair Ahmed, Rachael Xerri, Christopher Parmenter, Kiran Suain, Robert Markus, Lisa Chakrabarti, and Virginie Sottile (Sept. 2021). "Low-Power Sonication Can Alter Extracellular Vesicle Size and Properties". In: *Cells* 10.9. Publisher: MDPI AG, p. 2413. ISSN: 2073-4409. DOI: 10.3390/cells10092413.

Nogales, Eva and Sjors H.W. Scheres (May 2015). "Cryo-EM: A Unique Tool for the Visualization of Macromolecular Complexity". In: *Molecular Cell* 58.4, pp. 677–689. ISSN: 10972765. DOI: 10.1016/j.molcel.2015.02.019. URL: https://linkinghub.elsevier.com/retrieve/pii/S1097276515001331 (visited on 01/31/2025).

Nsairat, Hamdi, Dima Khater, Usama Sayed, Fadwa Odeh, Abeer Al Bawab, and Walhan Alshaer (May 2022). "Liposomes: structure, composition, types, and clinical applications". In: *Heliyon* 8.5, e09394. ISSN: 2405-8440. DOI: 10.1016/j.heliyon.2022.e09394.

Nygaard, Rie, Jonathan Kim, and Filippo Mancia (Oct. 2020). "Cryo-electron microscopy analysis of small membrane proteins". In: *Current Opinion in Structural Biology* 64, pp. 26–33. ISSN: 0959440X. DOI: 10.1016/j.sbi.2020.05.009. URL: https://linkinghub.elsevier.com/retrieve/pii/S0959440X20300774 (visited on 05/12/2025).

Object Research Systems (2024). *Dragonfly*. Version 2024. Montreal, Canada. URL: https://www.theobjects.com/dragonfly/.

Orloff, Jon, ed. (2009). *Handbook of charged particle optics*. Second edition. Boca Raton London New York: CRC Press. 1 p. ISBN: 978-1-4200-4554-3 978-1-4200-4555-0. DOI: 10.1201/9781420045550.

Osadnik, Hendrik, Michael Schöpfel, Eyleen Heidrich, Denise Mehner, Hauke Lilie, Christoph Parthier, H. Jelger Risselada, Helmut Grubmüller, Milton T. Stubbs, and Thomas Brüser (Nov. 2015). "PspF-binding domain PspA1-144 and the PspA·F complex: New insights into the coiled-coil-dependent regulation of AAA+ proteins". In: *Molecular Microbiology* 98.4, pp. 743–759. ISSN: 1365-2958. DOI: 10.1111/mmi.13154.

Osawa, Tsukiho, Kohki Fujikawa, and Keiko Shimamoto (Feb. 8, 2024). "Structures, functions, and syntheses of glycero-glycophospholipids". In: *Frontiers in Chemistry* 12, p. 1353688. ISSN: 2296-2646. DOI: 10.3389/fchem.2024.1353688. URL: https://www.frontiersin.org/articles/10.3389/fchem.2024.1353688/full (visited on 01/29/2025).

Pan, Jianjun, Frederick A. Heberle, Stephanie Tristram-Nagle, Michelle Szymanski, Mary Koepfinger, John Katsaras, and Norbert Kučerka (Sept. 2012). "Molecular structures of fluid phase phosphatidylglycerol bilayers as determined by small angle neutron and X-ray scattering". In: *Biochimica et Biophysica Acta (BBA) - Biomembranes* 1818.9, pp. 2135–2148. ISSN: 00052736. DOI: 10.1016/j.bbamem.2012.05.007. URL: https://linkinghub.elsevier.com/retrieve/pii/S0005273612001551 (visited on 09/18/2024).

Permanasari, Yurika, Erwin H. Harahap, and Erwin Prayoga Ali (Nov. 1, 2019). "Speech recognition using Dynamic Time Warping (DTW)". In: *Journal of Physics: Conference Series* 1366.1, p. 012091. ISSN: 1742-6588, 1742-6596. DOI: 10.1088/1742-6596/1366/1/012091. URL: https://iopscience.iop.org/article/10.1088/1742-6596/1366/1/012091 (visited on 02/13/2025).

Punjani, Ali, John L. Rubinstein, David J. Fleet, and Marcus A. Brubaker (Mar. 2017). "cryoSPARC: Algorithms for Rapid Unsupervised cryo-EM Structure Determination". In: *Nature Methods* 14.3. Publisher: Nature Publishing Group, pp. 290–296. DOI: 10.1038/nmeth.4169. URL: https://www.nature.com/articles/nmeth.4169 (visited on 02/17/2021).

Pyle, Euan, Joshua Hutchings, and Giulia Zanetti (2022). "Strategies for picking membrane-associated particles within subtomogram averaging workflows". In: *Faraday Discussions* 240, pp. 101–113. ISSN: 1359-6640, 1364-5498. DOI: 10.1039/D2FD00022A. URL: https://xlink.rsc.org/?DOI=D2FD00022A (visited on 05/12/2025).

Regan, David, Joseph Williams, Paola Borri, and Wolfgang Langbein (Oct. 29, 2019). "Lipid Bilayer Thickness Measured by Quantitative DIC Reveals Phase Transitions and Effects of Substrate Hydrophilicity". In: *Langmuir: the ACS journal of surfaces and colloids* 35.43, pp. 13805–13814. ISSN: 1520-5827. DOI: 10.1021/acs.langmuir.9b02538.

Reimer, Ludwig and Helmut Kohl (2008). *Transmission electron microscopy: physics of image formation*. 5th ed. Springer series in optical sciences 36. New York, NY: Springer. ISBN: 978-0-387-34758-5.

Ronneberger, Olaf, Philipp Fischer, and Thomas Brox (2015). *U-Net: Convolutional Networks for Biomedical Image Segmentation*. DOI: 10.48550/ARXIV.1505.04597.

Rose, H H (Apr. 1, 2008). "Optics of high-performance electron microscopes". In: *Science and Technology of Advanced Materials* 9.1, p. 014107. ISSN: 1878-5514.

DOI: 10.1088/0031-8949/9/1/014107. URL: https://iopscience.iop.org/article/10.1088/0031-8949/9/1/014107 (visited on 02/03/2025).

Rowlett, Veronica W., Venkata K. P. S. Mallampalli, Anja Karlstaedt, William Dowhan, Heinrich Taegtmeyer, William Margolin, and Heidi Vitrac (July 2017). "Impact of Membrane Phospholipid Alterations in Escherichia coli on Cellular Function and Bacterial Stress Adaptation". In: *Journal of Bacteriology* 199.13. Ed. by Victor J. DiRita. ISSN: 0021-9193, 1098-5530. DOI: 10.1128/JB.00849-16. URL: https://journals.asm.org/doi/10.1128/JB.00849-16 (visited on 01/29/2025).

Ruska, Helmut, Bodo V. Borries, and Ernst Ruska (Feb. 1939). "Die Bedeutung der Übermikroskopie für die Virusforschung". In: *Archiv für die gesamte Virusforschung* 1.1, pp. 155–169. ISSN: 0304-8608, 1432-8798. DOI: 10.1007/BF01243399. URL: http://link.springer.com/10.1007/BF01243399 (visited on 01/30/2025).

Sakoe, H. and S. Chiba (1978). "Dynamic programming algorithm optimization for spoken word recognition". In: *IEEE Transactions on Acoustics, Speech, and Signal Processing* 26.1, pp. 43–49. DOI: 10.1109/TASSP.1978.1163055.

Salfer, Maria, Javier F. Collado, Wolfgang Baumeister, Rubén Fernández-Busnadiego, and Antonio Martínez-Sánchez (Aug. 2020). "Reliable Estimation of Membrane Curvature for Cryo-Electron Tomography". In: *PLOS Computational Biology* 16.8. Ed. by Jeffrey J. Saucerman. Publisher: Public Library of Science (PLoS), e1007962. ISSN: 1553-7358. DOI: 10.1371/journal.pcbi.1007962.

Satapathy, Mantosh Kumar, Ting-Lin Yen, Jing-Shiun Jan, Ruei-Dun Tang, Jia-Yi Wang, Rajeev Taliyan, and Chih-Hao Yang (July 31, 2021). "Solid Lipid Nanoparticles (SLNs): An Advanced Drug Delivery System Targeting Brain through BBB". In: *Pharmaceutics* 13.8, p. 1183. ISSN: 1999-4923. DOI: 10.3390/pharmaceutics13081183. URL: https://www.mdpi.com/1999-4923/13/8/1183 (visited on 02/05/2025).

Scheres, Sjors H.W. (Dec. 2012). "RELION: Implementation of a Bayesian approach to cryo-EM structure determination". In: *Journal of Structural Biology* 180.3,

pp. 519–530. ISSN: 10478477. DOI: 10.1016/j.jsb.2012.09.006. URL: https://linkinghub.elsevier.com/retrieve/pii/S1047847712002481 (visited on 01/30/2025).

Schubert, Stefan, Peer Neubert, Johannes Poschmann, and Peter Protzel (June 2019). "Circular Convolutional Neural Networks for Panoramic Images and Laser Data". In: *2019 IEEE Intelligent Vehicles Symposium (IV)*. 2019 IEEE Intelligent Vehicles Symposium (IV). Paris, France: IEEE, pp. 653–660. ISBN: 978-1-72810-560-4. DOI: 10.1109/IVS.2019.8813862. URL: https://ieeexplore.ieee.org/document/8813862/ (visited on 02/12/2025).

Schönnenbeck, Philipp, Benedikt Junglas, and Carsten Sachse (Jan. 13, 2025). *CryoVIA - An image analysis toolkit for the quantification of membrane structures from cryo-EM micrographs*. DOI: 10.1101/2025.01.09.632183. URL: http://biorxiv.org/lookup/doi/10.1101/2025.01.09.632183 (visited on 02/03/2025).

Seifert, U. and Reinhard Lipowsky (Jan. 1, 1995). "Morphology of vesicles". In: *Structure and Dynamics of Membranes* 1, pp. 403–463.

Sejwal, Kushal, Mohamed Chami, Paul Baumgartner, Julia Kowal, Shirley A. Müller, and Henning Stahlberg (Feb. 1, 2017). "Proteoliposomes – a system to study membrane proteins under buffer gradients by cryo-EM". In: *Nanotechnology Reviews* 6.1, pp. 57–74. ISSN: 2191-9097, 2191-9089. DOI: 10.1515/ntrev-2016-0081. URL: https://www.degruyter.com/document/doi/10.1515/ntrev-2016-0081/html (visited on 01/30/2025).

Sharma, Karan D., Frederick A. Heberle, and M. Neal Waxham (Mar. 31, 2023). "Visualizing lipid membrane structure with cryo-EM: past, present, and future". In: *Emerging Topics in Life Sciences* 7.1, pp. 55–65. ISSN: 2397-8554, 2397-8562. DOI: 10.1042/ETLS20220090. URL: https://portlandpress.com/emergtoplifesci/article/7/1/55/232412/Visualizing-lipid-membrane-structure-with-cryo-EM (visited on 05/12/2025).

Shen, Yingjun, Haizhao Dai, Qihe Chen, Yan Zeng, Jiakai Zhang, Yuan Pei, and Jingyi Yu (2024). *DRACO: A Denoising-Reconstruction Autoencoder for Cryo-EM*. Version Number: 2. DOI: 10.48550/ARXIV.2410.11373. URL: https://arxiv.org/abs/2410.11373 (visited on 02/10/2025).

Sigworth, Fred J. (Feb. 2016). "Principles of cryo-EM single-particle image processing". In: *Microscopy* 65.1, pp. 57–67. ISSN: 2050-5698, 2050-5701. DOI: 10.1093/jmicro/dfv370. URL: https://academic.oup.com/jmicro/article-lookup/doi/10.1093/jmicro/dfv370 (visited on 01/31/2025).

Simons, Kai and Robert Ehehalt (Sept. 1, 2002). "Cholesterol, lipid rafts, and disease". In: *Journal of Clinical Investigation* 110.5, pp. 597–603. ISSN: 0021-9738. DOI: 10.1172/JCI0216390. URL: http://www.jci.org/articles/view/16390 (visited on 02/06/2025).

Skruzny, Michal, Ambroise Desfosses, Simone Prinz, Svetlana O. Dodonova, Anna Gieras, Charlotte Uetrecht, Arjen J. Jakobi, Marc Abella, Wim J.H. Hagen, Joachim Schulz, Rob Meijers, Vladimir Rybin, John A.G. Briggs, Carsten Sachse, and Marko Kaksonen (Apr. 2015). "An Organized Co-Assembly of Clathrin Adaptors Is Essential for Endocytosis". In: *Developmental Cell* 33.2. Publisher: Elsevier BV, pp. 150–162. ISSN: 1534-5807. DOI: 10.1016/j.devcel.2015.02.023.

Smith, Steven W. (1997). *The scientist and engineer's guide to digital signal processing*. 1st ed. San Diego, Calif: California Technical Pub. 626 pp. ISBN: 978-0-9660176-3-2.

Stalling, Detlev, Malte Westerhoff, and Hans-Christian Hege (Aug. 4, 2012). "Amira - a Highly Interactive System for Visual Data Analysis". In: *The visualization handbook*.

Subramaniam, Sriram, Werner Kühlbrandt, and Richard Henderson (Jan. 2016). "CryoEM at IUCrJ: A New Era". In: *IUCrJ* 3.1. Publisher: International Union of Crystallography (IUCr), pp. 3–7. ISSN: 2052-2525. DOI: 10.1107/s2052252515023738.

Suda, Yasuyuki and Akihiko Nakano (Apr. 2012). "The Yeast Golgi Apparatus". In: *Traffic* 13.4, pp. 505–510. ISSN: 1398-9219, 1600-0854. DOI: 10.1111/j.

1600-0854.2011.01316.x. URL: https://onlinelibrary.wiley.com/doi/10.1111/j.1600-0854.2011.01316.x (visited on 02/05/2025).

Tahara, Yoshikazu and Yoshinori Fujiyoshi (Apr. 1994). "A new method to measure bilayer thickness: Cryo-electron microscopy of frozen hydrated liposomes and image simulation". In: *Micron* 25.2, pp. 141–149. ISSN: 09684328. DOI: 10.1016/0968-4328(94)90039-6. URL: https://linkinghub.elsevier.com/retrieve/pii/0968432894900396 (visited on 05/12/2025).

Tao, Xiao, Chen Zhao, and Roderick MacKinnon (May 2, 2023). "Membrane protein isolation and structure determination in cell-derived membrane vesicles". In: *Proceedings of the National Academy of Sciences* 120.18, e2302325120. ISSN: 0027-8424, 1091-6490. DOI: 10.1073/pnas.2302325120. URL: https://pnas.org/doi/10.1073/pnas.2302325120 (visited on 01/30/2025).

Tarasenko, Daryna and Michael Meinecke (Mar. 2021). "Protein-dependent membrane remodeling in mitochondrial morphology and clathrin-mediated endocytosis". In: *European Biophysics Journal* 50.2, pp. 295–306. ISSN: 0175-7571, 1432-1017. DOI: 10.1007/s00249-021-01501-z. URL: https://link.springer.com/10.1007/s00249-021-01501-z (visited on 02/07/2025).

Tietz, Hr (Aug. 2008). "Design and Characterization of 64 MegaPixel Fiber Optic Coupled CMOS Detector for Transmission Electron Microscopy". In: *Microscopy and Microanalysis* 14 (S2), pp. 804–805. ISSN: 1431-9276, 1435-8115. DOI: 10.1017/S1431927608084675. URL: https://academic.oup.com/mam/article/14/S2/804/6919067 (visited on 01/30/2025).

Wan, W. and J.A.G. Briggs (2016). "Cryo-Electron Tomography and Subtomogram Averaging". In: *Methods in Enzymology*. Vol. 579. Elsevier, pp. 329–367. ISBN: 978-0-12-805382-9. DOI: 10.1016/bs.mie.2016.04.014. URL: https://linkinghub.elsevier.com/retrieve/pii/S0076687916300325 (visited on 01/31/2025).

Wang, Liguo and Fred Sigworth (Feb. 2009). "Cryo-EM Structure of Functional BK Channels in Lipid Bilayers". In: *Biophysical Journal* 96.3, 413a. ISSN: 00063495.

DOI: 10.1016/j.bpj.2008.12.2107. URL: https://linkinghub.elsevier.com/retrieve/pii/S0006349508023278 (visited on 01/30/2025).

Xu, Chentianye, Xueying Zhan, and Min Xu (2024). *CryoMAE: Few-Shot Cryo-EM Particle Picking with Masked Autoencoders*. Version Number: 1. DOI: 10.48550/ARXIV.2404.10178. URL: https://arxiv.org/abs/2404.10178 (visited on 02/10/2025).

Yan, Xiaofeng, Shudong Li, Weilin Huang, Hao Wang, Tianfang Zhao, Mingtao Huang, Niyun Zhou, Yuan Shen, and Xueming Li (Jan. 8, 2025). "MPicker: visualizing and picking membrane proteins for cryo-electron tomography". In: *Nature Communications* 16.1, p. 472. ISSN: 2041-1723. DOI: 10.1038/s41467-024-55767-w. URL: https://doi.org/10.1038/s41467-024-55767-w.

Yan, Xiaolong (2021). *Skeleton Network*. Publication Title: GitHub repository. URL: https://github.com/Image-Py/sknw.

Yao, Xia, Xiao Fan, and Nieng Yan (Aug. 4, 2020). "Cryo-EM analysis of a membrane protein embedded in the liposome". In: *Proceedings of the National Academy of Sciences* 117.31, pp. 18497–18503. ISSN: 0027-8424, 1091-6490. DOI: 10.1073/pnas.2009385117. URL: https://pnas.org/doi/full/10.1073/pnas.2009385117 (visited on 01/30/2025).

Zhang, Peijun and Jenny E. Hinshaw (Sept. 2001). "Three-Dimensional Reconstruction of Dynamin in the Constricted State". In: *Nature Cell Biology* 3.10. Publisher: Springer Science; Business Media LLC, pp. 922–926. ISSN: 1476-4679. DOI: 10.1038/ncb1001-922.

Zhang, T. Y. and C. Y. Suen (Mar. 1984). "A Fast Parallel Algorithm for Thinning Digital Patterns". In: *Communications of the ACM* 27.3. Publisher: Association for Computing Machinery (ACM), pp. 236–239. DOI: 10.1145/357994.358023.

Zhao, Jiaping and Laurent Itti (2016). *shapeDTW: shape Dynamic Time Warping*. Version Number: 1. DOI: 10.48550/ARXIV.1606.01601. URL: https://arxiv.org/abs/1606.01601 (visited on 02/13/2025).

Zheng, Shawn, Georg Wolff, Garrett Greenan, Zhen Chen, Frank G.A. Faas, Montserrat Bárcena, Abraham J. Koster, Yifan Cheng, and David A. Agard (2022). "AreTomo: An integrated software package for automated marker-free, motion-corrected cryo-electron tomographic alignment and reconstruction". In: *Journal of Structural Biology: X* 6, p. 100068. ISSN: 25901524. DOI: 10.1016/j.yjsbx.2022.100068. URL: https://linkinghub.elsevier.com/retrieve/pii/S2590152422000095 (visited on 02/07/2025).

Zheng, Shawn Q, Eugene Palovcak, Jean-Paul Armache, Kliment A Verba, Yifan Cheng, and David A Agard (Apr. 2017). "MotionCor2: anisotropic correction of beam-induced motion for improved cryo-electron microscopy". In: *Nature Methods* 14.4, pp. 331–332. ISSN: 1548-7091, 1548-7105. DOI: 10.1038/nmeth.4193. URL: https://www.nature.com/articles/nmeth.4193 (visited on 02/25/2025).

Zhong, Ellen D., Tristan Bepler, Bonnie Berger, and Joseph H. Davis (Feb. 2021). "CryoDRGN: reconstruction of heterogeneous cryo-EM structures using neural networks". In: *Nature Methods* 18.2, pp. 176–185. ISSN: 1548-7091, 1548-7105. DOI: 10.1038/s41592-020-01049-4. URL: https://www.nature.com/articles/s41592-020-01049-4 (visited on 02/10/2025).

Zhou, W and M D Resh (Dec. 1996). "Differential membrane binding of the human immunodeficiency virus type 1 matrix protein". In: *Journal of Virology* 70.12, pp. 8540–8548. ISSN: 0022-538X, 1098-5514. DOI: 10.1128/jvi.70.12.8540-8548.1996. URL: https://journals.asm.org/doi/10.1128/jvi.70.12.8540-8548.1996 (visited on 01/29/2025).